UC Merced

UC Merced Electronic Theses and Dissertations

Title

Hierarchical Carbon Electrodes from 3D Printed Polymers via Transition Metal—Catalyzed Pyrolysis and Tannic Acid Integration

Permalink

https://escholarship.org/uc/item/01566581

ISBN

9798173794239

Author

Kuo, Han-Lin

Publication Date

2026-08-18

Copyright Information

This work is made available under the terms of a Creative Commons Attribution License, available at https://creativecommons.org/licenses/by/4.0/

Peer reviewed|Thesis/dissertation

eScholarship.org Powered by the California Digital Library
University of California

UNIVERSITY OF CALIFORNIA, MERCED

Hierarchical Carbon Electrodes from 3D Printed Polymers via Transition Metal–Catalyzed Pyrolysis and Tannic Acid Integration

Submitted to the School of Engineering

in partial fulfillment of the requirements for

the degree of Doctor of Philosophy

by

Han Lin Kuo

2026

Committee Members:

Professor Jennifer Lu (University of California, Merced)

Professor Christopher Viney (University of California, Merced)

Professor Yat Li (University of California, Santa Cruz)

Chapter 2 © 2025 Carbon

Signature page

The Dissertation of Han Lin Kuo is approved and is acceptable in quality and form for publication on microfilm and in digital formats.

Professor Jennifer Lu, Advisor

Professor Christopher Viney, Committee chair

Professor Yat Li

University of California, Merced

2026

This Dissertation is dedicated to:

Mom and Dad, for giving me the tools to succeed, whatever my path, and always supporting me, whatever I am doing

And to Yi-Rong, for always standing by my side and cheering me up through all the ups and downs of my Ph.D. journey.

Table of Contents

Signature page ……...iii

Preface……...iv

Acknowledgement……...viii

Curriculum Vita……ix

List of Figures……...x

List of Tables……..xiv

Abstract……1

Chapter 1 – Introduction of 3D carbon supercapacitor: operating principles, significance, and future potentials……..2

1.1. Introduction to 3D carbon supercapacitor……2

1.2. Charge storage mechanism of supercapacitors……3

1.2.1. Electric double-layer capacitors (EDLCs) ……4

1.2.2. Pseudocapacitor……7

1.2.3. Hybrid capacitor……9

1.3. Carbon-based supercapacitors……9

1.3.1. Activated carbon (ACs) based supercapacitors……9

1.3.2. Carbon nanotubes (CNTs) based supercapacitors……10

1.4. 3D supercapacitor……11

1.4.1. 3D printing supercapacitor……11

1.4.2. 3D pyrolytic carbon for energy storage……19

1.4.3. Selection of 3D printing resin for 3D pyrolytic carbon……21

Chapter 2 – Design of 3D Carbon Electrodes via Metal-Catalyzed Conversion of 3D-Printed Polymer PR48 Templates……29

2.1. Selection of metal catalyst for graphitization……29

2.1.1. Catalytic graphitization……29

2.1.2. Thermal decomposition……31

2.1.3. Capture hydrocarbon byproducts from degradation gases……32

2.2. Selection of metal chloride salts……32

2.3. Experimental section……33

2.3.1. Metal catalyst impregnation process……34

2.3.2. Pyrolysis procedure……35

2.3.3. Materials characterization……35

2.3.4. Strut size calculation……35

2.4. Results and discussion……36

2.4.1. Conformal deposition of catalysts on 3D polymer template……36

2.4.2. Metal catalyst formation of coordination complexes and metal hydroxides/oxides on polymer surface……39

2.4.3. Catalytic degradation demonstrated with lowered decomposition temperature……41

2.4.4. Enhanced graphitization with different transition metal catalysts……45

2.5. Conclusion……47

Chapter 3 – Design of High-resolution 3D Carbon Electrodes via Tannic Acid and Metal Catalyst Integration from 3D-Printed Elegoo Template……53

3.1. Selection of tannic acid as carbon precursors……53

3.2. Experimental section……56

3.2.1. Preparation of high-resolution 3D printed Elegoo sample……56

3.2.2. Preparation of tannic acid (TA)/$FeCl_3$ soaking solution……57

3.2.3. Pyrolysis procedure……57

3.2.4. Carbon nanotubes growing procedure……57

3.2.5. Materials characterization……58

3.2.6. Data analysis of electrochemical data and SEM images……58

3.3. Results and discussion……62

3.3.1. Selection of tannic acid……62

3.3.2. Effects of $FeCl_3$ and tannic acid (TA) infiltration……63

3.3.3. Different feature size effect……64

3.3.4. Effects of $FeCl_3$/TA infiltration on char yield, dimensional retention and surface morphology……65

3.3.5.Different Fe and tannic acid ratios to determine the best performance……68

3.3.6.CNT growth on 3D hierarchical samples to enhance electrochemical performance and electromagnetic interference (EMI) shielding effect……69

3.4. Conclusion……74

Chapter 4 – Enhancing Energy Storage Performance of Pyrolytic Elegoo Carbon through Secondary Structure Growth - PDAN and CNT Integration……79

4.1. PDAN deposition on 3D carbon template……79

4.1.1. PDAN selection……79

4.1.2. Experimental section…… .....….80
4.2. Mechanistic Insights into PDAN: Electropolymerization and Energy Storage Behavior… .....……80
4.2.1. Electropolymerization mechanism…… .....….80
4.2.2. Charge storage mechanism…….....….81
4.3. Results and discussion…….....……..83
4.3.1. Conformal PDAN deposition on 3D carbon electrode…….....…...83
4.3.2. Enhanced capacitance by additional pseudocapacitance from PDAN…….....……84
4.3.3. Electrochemical performance of different PDAN thicknesses …….....…..86
4.3.4. Redox kinetics (capacitive and diffusive contribution) on PDAN-coated 3D carbon electrodes…….....……..88
4.3.5. Cycle stability of PDAN-coated 3D carbon sample…….....……...98
4.4. Conclusion and future plan…… ..... ……..…100

Acknowledgement

I would like to acknowledge the following individuals and organizations that supported me throughout my Ph.D. journey and helped make this dissertation possible.

I would like to express my sincerest gratitude to my advisor, Jennifer Lu, for her guidance and mentorship throughout this work and my Ph.D. journey. Her patience, passion, dedication to research and scientific integrity, and constant support made this dissertation possible.

I would like to extend deepest appreciation to my committee members Christopher Viney and Yat Li for their guidance and feedback

I would like to acknowledge UC Merced Imaging and Microscopy Facility for maintaining the various spectrometers and microscopes which contributed to this work, and particularly Kennedy Nguyen for his support and guidance in their use.

I would like to acknowledge the support and contributions of Joe DeSimone's lab at Stanford University, and particularly his students Philip Onffroy for their valuable discussions and material support.

I would like to thank Professor Shaowei Chen and his students, Qiming Liu and Dingjie Pan, for their invaluable help in the fields of ORR and OER, as well as for giving me the opportunity to collaborate with them.

I would like to acknowledge Prof. Yat Li and his student, Dun Lin, at UC Santa Cruz for their mentorship in electrochemistry.

This work was financially supported by the Merced Nanomaterials Center for Energy and Sensing (MACES).

I would like to express my deepest appreciation to those who helped and supported me in achieving my goals throughout my academic journey. The text and content of this dissertation were directed, supervised, and/or supported by:

Prof. Jennifer Lu

Prof. Joe DeSimone

Prof. Viney

Prof. Yat Li

Samuel Chiovoloni

Philip Onffroy

Austin Ashworth

Levi Williams

Yaneth Hernandez

Adan Rodriguez

Zelma Alvillo Guerrero

Curriculum Vita

Education

2016 B.S. in Materials Science and Engineering, National Taiwan University

2026 Ph.D. in Materials and Biomaterials Science and Engineering, University of California, Merced

Professional experience

2017~2018, Lithography process engineer, WINs Semiconductor Corp.

2018~2019, Research assistant, Institute of Atomic and Molecular Science, Academia Sinica

2020~present, Ph.D. student, University of California, Merced

Publications

- Engineered 3D micro-architected carbon structures via conformal deposition of multifunctional transition metal catalysts (Carbon, 2025)
  Author: HL Kuo, PR Onffroy, SP Chiovoloni, L Williams, JM DeSimone, J Lu
- Opportunities at the Intersection of 3D Printed Polymers and Pyrolysis for the Microfabrication of Carbon-Based Energy Materials (JACS Au, 2024)
  Author: PR Onffroy, S Chiovoloni, HL Kuo, MA Saccone, JQ Lu, JM DeSimone
- Ultrafast synthesis of amorphous molybdenum sulfide by magnetic induction heating for hydrogen evolution reaction (Applied Catalysis, 2024))
  Author: Qiming Liu, Forrest Nichols, Amrinder Bhuller, Kevin Singewald, Han-Lin Kuo, Jennifer Q Lu, Glenn L Millhauser, Frank Bridges, Qingfeng Ge, Shaowei Chen
- Stable Cuprous Hydroxide Nanostructures by Organic Ligand Functionalization (Advanced Materials, 2023)
  Author: Qiming Liu, Yi Peng, Zaheer Masood, Davida DuBois, John Tressel, Forrest Nichols, Paul Ashby, Rene Mercado, Tufa Assafa, Dingjie Pan, Han-Lin Kuo, Jennifer Q Lu, Frank Bridges, Glenn Millhauser, Qingfeng Ge, Shaowei Chen
- Platinum-anchored iron oxide nanostructures for efficient hydrogen evolution reaction in acidic media (J. Phys. Chem. C, 2023)
  Author: Bingzhe Yu, Qiming Liu, Forrest Nichols, Kiley Mayford, Dingjie Pan, Han-Lin Kuo, Jennifer Q Lu, Frank Bridges, Shaowei Chen
- Oxygen reduction reaction catalyzed by carbon composites with ruthenium-doped iron oxide nanoparticles (Materials Advanced, 2022)
  Author: Qiming Liu, Hong Bo Zhou, Forrest Nichols, Han-Lin Kuo, Rene Mercado, Bingzhang Lu, Weiya Zhu, Yashu Liu, Jennifer Q Lu, Frank Bridges, Shaowei Chen

Patents

- Methods for Fabrication of Dual Network Polymers Formed from Polymeric Precursors and In Situ Polymerization and Systems for Same (WO/2025/151617)
  Author: Jennifer Lu, Joseph M. DeSimone, Max A. Saccone, Philip R. Onffroy, Samuel Chiovoloni, Han-Lin Kuo, Austin Ashworth
- Solid-state polymer electrolyte systems and batteries using the same (US20240297354A1)
  Author: Jennifer Lu, Michael Leveille, Han-Lin Kuo, Lexi Hefner

Manuscript

- Hierarchical 3D Carbon Electrodes Grafted with Poly(diaminonaphthalene) for High-Performance Cation-Based Energy Storage

•

List of Figures

Figure 1.1: Ragone plot of different electrochemical energy storage devices.

Figure 1.2: Basic configuration of supercapacitors. The supercapacitor consists of two symmetric porous carbon electrodes sandwiched between two current collectors and separated by an isolated separator.

Figure 1.3: Different types of supercapacitors: (A) EDLC type, (B) pseudocapacitor type, (C) hybrid capacitor type.

Figure 1.4: (a) Helmholtz, (b) Gouy-Chapman, and (c) Stern Model of the electrical double layer formed at a positively charged electrode in aqueous electrolyte. The electric potential (ϕ) decreases when transitioning from the electrode (ϕe), the bulk electrolyte away from the electrode surface (ϕs). The Stern plane defines the closest approach between ions and the charged surface. The Stern layer is free of mobile ions, while the diffuse layer begins farther from the electrode surface, typically within 10 to 100 nm.

Figure 1.5: The charge state of symmetric porous carbon electrode EDLC and its corresponding equivalent circuit. R represents resistors and C represents capacitors.

Figure 1.6: Different types of reversible redox mechanisms that give rise to pseudocapacitance: (a) underpotential deposition, (b) redox pseudocapacitance, and (c) intercalation pseudocapacitance.

Figure 1.7: The cell configuration of thin and thick electrodes with the weight ratios of the electrodes to other inactive materials (current collectors and separators).

Figure 1.8: Approximate global 3D printing market during the 10 years from 2023 to 2033. Figure 1.9: Schematic of the direct ink writing process.

Figure 1.10: Schematic of the fused deposition modeling process.

Figure 1.11: Schematic of the powder bed fusion process.

Figure 1.12: Schematic of the stereolithography process.

Figure 1.13: Schematic of the digital light processing method

Figure 1.14: Schematic illustration of projection micro stereolithography.

Figure 1.15: Schematic of CLIP continuous printing. The part is printed by elevating the build support plate while dynamically projecting 2D cross-sectional UV images. An oxygen-permeable window maintains a "dead zone" (a persistent liquid interface) beneath the rising part, preventing adhesion to the window.

Figure 2.1: Phase diagram of Fe and carbon.

Figure 2.2: Phase diagram of Ni and carbon.

Figure 2.3: Phase diagram of Cu and carbon.

Figure 2.4: Schematic depiction of pyrolysis and catalytic decomposition for hydrogen gas and CNTs growth with Fe/Ni catalysts

Figure 2.5: Mechanism of combined catalysis of metal halide catalysts for the formation of multiwalled carbon nanotubes from polypropylene during pyrolysis.

Figure 2.6: Carbon distribution in products after pyrolysis with different Fe salts.

Figure 2.7: (a) Schematic illustration of the process flow for selective metal salt impregnation onto 3D

polymer templates via two approaches; (b) Optical images of the polymer template (leftmost) and the resulting 3D carbon after pyrolysis at 900 °C using approach 1, showing areal retention and density.

Figure 2.8: Illustration of metal cations interacting with O–C=O groups on the polymer surfaces and infiltrating into the polymer lattice to form coordination bonds.

Figure 2.9: Using ImageJ software to measure strut size by the two thickest and two thinnest regions of each carbon strut.

Figure 2.10: Photo images of samples after soaking in 50 mM metal chloride solution in ethanol for 72 hours (Approach 1) and after solvent evaporation for Fe^{3+} catalyst deposition (Approach 2; Bottom: Optical images of catalyst infused samples using approach 1, (a) 50 mM $CuCl_2$, (b) 50 mM $NiCl_2$, (c) 50 mM $FeCl_2$, (d) 50 mM $FeCl_3$ in ethanol solution.

Figure 2.11: Carbon yield and range (based on three runs) of metal-treated PR48 versus neat polymer.

Figure 2.12: SEM images for carbon strut with different treatments: (a) control, (b) Cu^{2+}, (c) Ni^{2+}, (d) Fe^{2+} and (e) Fe^{3+}, prepared from polymer pyrolyzed at 900°C for 2 h.

Figure 2.13: XPS O(1s) spectra, displaying the shift of the ester group's binding energy from its undisturbed polymer center upon interaction with transition metal cations. (Peak values of Cu^{2+} is at 532.1 eV, Ni^{2+} is 532.0 eV, Fe^{2+} is 531.7 eV, and Fe^{3+} is 530.8 eV vs 532.5 eV untreated) The peaks are related to metal oxides and hydroxides marked with*.

Figure 2.14: Pourbaix diagram of (a) Ni, (b) Fe, (c) Cu, showing the energy for metal oxide reduced to metal $Cu^{2+} < Ni^{2+} < Fe^{3+}$ (orange line $\Delta G = -nF\Delta E$ (potential)) and onset pH for the formation of Ni and Fe hydroxides and oxides (blue vertical line).

Figure 2.15: (a) Thermogravimetric analysis (TGA) results for metal salt-soaked PR48 samples (via approach 1) with inset to highlight variance of the onset; (b) Normalized derivative thermogravimetric (DTG) curves of mass loss rate vs. temperature showing the degradation profile variation of different metal species.

Figure 2.16: Schematic reactions promoted by $FeCl_3$ during pyrolysis.

Figure 2.17: Example spectrum of standard modulus carbon fiber with possible peak components shown: D1, D2, D3, D4, G band.

Figure 2.18: Raman spectra of carbon samples after 900°C pyrolysis and ratios of D1 and G bands used to distinguish between amorphous and graphitic carbon content. For XPS measurements, two samples were analyzed for each condition at six different locations.

Figure 2.19: Raman data fitted by a four-peak model using Gaussian functions of the Figure 4 spectra demonstrating a more precise distinction of D1, D3, D4, and G band peaks. (a) Neat polymer, (b) $CuCl_2$, (c) $NiCl_2$, (d) $FeCl_2$ and (e) $FeCl_3$.

Figure 3.1: Chemical structure of tannic acid

Figure 3.2: (a) ImageJ measurement of eight different unit cell sizes from an SEM image, (b) ImageJ measurement of 8 different unit cell areas, (c) ImageJ measurement of strut size by measuring two thickest and two thinnest regions of each carbon strut.

Figure 3.3: Integrated area calculation from OriginPro 2023b to calculate the area capacitance from the GCD discharge curve

Figure 3.4: Octet-truss unit cell, a is the unit cell size, and L is the strut length.

Figure 3.5: (a) Thermogravimetric analysis (TGA) of Elegoo and PR48 octet lattices with as-printed 50 μm

struts and 500 μm unit cell size under typical inert pyrolysis conditions; (b) (i) photographs of the original polymer template (left), the resulting pyrolyzed product (Elegoo, middle), and the resulting pyrolyzed product (PR48, right) using 50 μm strut size, 500 μm unit cell size polymer templates, and (ii) scanning electron microscopy (SEM) images of the corresponding 3D pyrolytic carbon structures.

Figure 3.6: Thermogravimetric analysis (TGA) of pure PR48, pure Elegoo and TA-infiltrated Elegoo octet lattices with as-printed 50 μm struts and 500 μm unit cell size under typical inert pyrolysis conditions.

Figure 3.7: SEM images of 3D carbon lattice derived from 3D printed Elegoo after pyrolysis at 900°C without $FeCl_3$ and tannic acid soaking (a, b, c) and with 0.08 M $FeCl_3$ + 0.08 M tannic acid soaking (d, e, f).

Figure 3.8: SEM images of 3D carbon lattice derived from 3D printed Elegoo after pyrolysis at 900°C without FeCl3 and tannic acid soaking (a) and with $FeCl_3$ and tannic acid soaking (b) at 100000 X magnification.

Figure 3.9: (a) Cyclic voltammetry of control and Fe-TA infiltration samples at 5 mV/s in 0.5 M H_2SO_4, (b) GCD discharge curve of control and Fe-TA samples at 5 mA/cm^2 in 0.5 M H_2SO_4, (c) summarized areal capacitance of control and Fe-TA treated samples (For each condition, we prepared three samples, all of which exhibited the same trend.)

Figure 3.10: Cyclic voltammetry of control and Fe-TA infiltrated samples with different Fe/TA ratios at (a) 20 mV/s and (b) 5 mV/s. (c) Nyquist plot of control and Fe-TA infiltrated samples with different Fe/TA ratios. (Each condition was reproduced 3 times, and all of them followed the same trend.)

Figure 3.11: SEM images of 3D pyrolytic carbon derived from a high-resolution 3D-printed Elegoo sample after pyrolysis (a, b) control sample without any treatment, (c, d) Fe: TA=2:1 soaking, and (e, f) Fe: TA=1:1 at 2000X and 10000X magnification.

Figure 3.12: SEM images of 50 μm control sample after CNT (a) at 100 X, (b) loose CNT growth region at 200 X, (c) dense CNT growth region at 200 X.

Figure 3.13: SEM images of pyrolytic 50 μm Elegoo before CNT growth at (a) 200 X, (b) 1000 X, SEM images of pyrolytic 50 μm Elegoo after CNT growth at (c) 200 X, (d) 1000 X, (e) 5000 X, and (f) 100000 X.

Figure 3.14: (a) Cyclic voltammetry of 50 μm Fe-TA infiltrated Elegoo sample before and after CNT growth at 20 mV/s in 0.5 M H_2SO_4, (b) Nyquist plot of 50 μm Elegoo before and after CNT growth in 0.5 M H_2SO_4

Figure 3.15: Schematic representation showing the mechanism of electromagnetic shielding.

Figure 3.16: SEM images of Carbon nanofiber clusters on silicon carbide template (a) 2k, (b) 10k x, (c) thick CNT clusters at 100k X, (d) thin CNT clusters at 100k X.

Figure 4.1: Suggested mechanism of 1,5-diaminonaphthalene electropolymerization.

Figure 4.2: Charge storage mechanism of bipolar branched PDAN in the charge/discharge process.

Figure 4.3: Charge storage mechanism of laddered PDAN in the charge/discharge process.

Figure 4.4: SEM images before PDAN deposition (a, b), and after PDAN deposition (c, d), showing the conformal PDAN coating and resulting smooth surface morphology; (e) Cyclic voltammetry in 0.5 M H_2SO_4 at 5 mV/s, (f) Cyclic voltammetry in 3 M $NaClO_4$ at 5 mV/s.

Figure 4.5: (a) Cyclic voltammetry of 3D carbon prepared from pure polymer (3D carbon_P), 3D carbon prepared with Fe-TA infiltration, and PDAN-coated Fe-TA-treated 3D carbon in 0.5 M H_2SO_4 at 5 mV/s, (b) Areal capacitance of the 3D carbon_P, 3D carbon (Fe: TA), and PDAN@3D carbon in 0.5 M H_2SO_4

calculated from GCD, (c) Nyquist plot of the 3D carbon_P, 3D carbon (Fe: TA), and PDAN@3D carbon in 0.5 M H_2SO_4.

Figure 4.6: GCD curves of 3D carbon prepared from pure polymer (3D carbon_P), 3D carbon prepared with Fe-TA infiltration, and PDAN-coated Fe-TA-treated 3D carbon in 0.5 M H_2SO_4 at (a) 20 mA/cm^2, (b)10 mA/cm^2, (c) 5 mA/cm^2.

Figure 4.7: Cyclic voltammetry of 3D carbon before and after PDAN deposition in 0.5 M H_2SO_4 (a-c) at 20, 10, 5 mV/s in 0.5 M H_2SO_4, and (d-f) at 20, 10, 5 mV/s in 3 M $NaClO_4$.

Figure 4.8: Areal capacitance improvement after PDAN deposition on 3D carbon electrodes in 0.5 M H_2SO_4 and 3 M $NaClO_4$ at scan rates of 20, 10, and 5 mV/s. (Four different 3D carbon samples were evaluated before and after PDAN deposition in both electrolytes.)

Figure 4.9: (a) Cyclic voltammetry curves at 1, 2, 5, 8, and 10 mV/s of 1.2 V-PDAN deposition 3D carbon in 3 M $NaClO_4$, (b) Cyclic voltammetry curves at 1, 2, 5, 8, and 10 mV/s of 1.7V-PDAN deposition 3D carbon in 3 M $NaClO_4$, (c) Cyclic voltammetry curves at 2 mV/s of 3D carbon, 1.2 V-PDAN deposition 3D carbon in 3 M $NaClO_4$.

Figure 4.10: (a) Cyclic voltammetry curves in 3 M $NaClO_4$ at 5 mV/s before and after PDAN deposition, (b)GCD curves in 3 M $NaClO_4$ at 5 mA/cm2 before and after PDAN deposition, and (c) areal capacitance calculated from GCD data in 3 M NaClO4 before and after PDAN deposition.

Figure 4.11: Energy storage devices are distinguished by their appropriate b-value.

Figure 4.12: (a) b-value of PDAN-1.2 V in 3 M $NaClO_4$ at scan rates 1, 2, 5, 8, 10 mV/s, (b) b-value of PDAN-1.7 V in 3 M $NaClO_4$ at scan rates 1, 2, 5, 8, 10 mV/s.

Figure 4.13: (a-e) Cyclic voltammetry curves at 10, 8, 5, 2, and 1 mV/s of 1.2 V-PDAN deposition 3D carbon in 0.5 M H_2SO_4, (f) Capacitive and diffusive contribution ratios based on Dunn's analysis at different scan rates.

Figure 4.14: (a-e) Cyclic voltammetry and Dunn analysis curves at 10, 8, 5, 2, and 1 mV/s of 1.2 V-PDAN deposition 3D carbon in 3 M $NaClO_4$, (f) Capacitive and diffusive contribution ratios based on Dunn's analysis at different scan rates.

Figure 4.15: (a-e) Cyclic voltammetry and Dunn analysis curves at 10, 8, 5, 2, and 1 mV/s of 1.7 V-PDAN deposition 3D carbon in 3 M $NaClO_4$, (f) Capacitive and diffusive contribution ratios based on Dunn's analysis at different scan rates.

Figure 4.16: EIS data of 3D carbon and 3D carbon with different PDAN deposition potential samples in 3 M $NaClO_4$.

Figure 4.17: (a, b) The Randles equivalent circuit and its behavior at (c, d) low and (e, f) high frequencies.

Figure 4.18: Warburg coefficient data of 3D carbon and 3D carbon with different PDAN deposition potential samples in 3 M $NaClO_4$ (two samples are tested under different PDAN deposition, both show the same trend.)

Figure 4.19: (a) 5 mV/s CV curves in 3 M NaCl after 5000,7500,10000 and 100000 cycles, (b) Areal capacitance and capacitance retention of S1-PDAN after 100,000 cycles at 100 mV/s, (c) Coulombic efficiency of S1-PDAN after 1000000 cycles at 100 mV/s.

Figure 4.20: (a) 10 mV/s CV curves in 3 M $NaClO_4$ after 100, 300,3000 and 7500 cycles, (b) GCD curves of PDAN sample at 30 mA/cm^2 after 100, 300, 3000 and 7500 cycles (c) Areal capacitance and capacitance retention of PDAN coated sample after 7500 cycles at 30 mA/cm^2, (d) Coulombic efficiency of PDAN coated sample after 7500 cycles at 30 mA/cm^2.

List of Tables

Table 1.1: Electrochemical properties of supercapacitors and batteries.

Table 1.2: Summary of sample feature sizes of current additive manufacturing used in combination with pyrolysis for generation of pyrolytic carbon template in energy storage applications.

Table 1.3: Composition and characteristics of the commercial 3D printing resins that have been used to generate pyrolytic carbon by pyrolysis.

Table 2.1: shows the effect of catalysts on carbon density and geometric retention. Table 2.2: Carbon yield of PR48 samples soaked in different metal catalysts.

Table 2.3: Variation in strut diameter of pyrolyzed PR48 samples soaked in different transition-metal catalysts using approach 1.

Table 2.4: Average metal content, as determined by XPS survey scans of 4-5 samples for each treatment. Table 2.5. Comparison of carbon yield and strut diameter of different catalyst shell thickness.

Table 3.1: Common carbon precursors for preparation of pyrolytic carbon materials.

Table 3.2: Calculation of GCD data of 3D carbon sample tested in 0.5 M H_2SO_4.

Table 3.3: Char yield of 3D polymer pyrolyzed at 850 ºC

Table 3.4: Char yield and dimensional retention of control sample and Fe-TA-soaked sample after pyrolysis at 900 ºC.

Table 3.5: Areal capacitance calculated from GCD measurement of high-resolution carbonized Elegoo samples in 0.5 M H_2SO_4 with SCE as reference electrode, and graphite rod as counter electrode.

Table 3.6: The electrochemical performance of the 3D-printed carbon electrode in this work compared with previous literature with similar thickness.

Table 4.1: Comparison of different analysis methods to investigate charge-storage mechanism.

Abstract

Today, the transition to renewable energy systems has highlighted the need for efficient energy storage technologies to address the intermittent nature of sources such as solar and wind. While electrochemical devices such as supercapacitors and batteries offer viable solutions, their performance is often constrained by conventional electrode fabrication methods that limit active material loading, ion transport, and structural control. Designing three-dimensional (3D) electrodes provides a pathway to overcome these limitations by enabling thick, architected structures with high surface area and improved mass transport. Additive manufacturing of 3D electrodes enables precise control of electrode geometry, thereby increasing energy storage capacity through well-defined hierarchical structures. However, the resolution of conductive materials is limited in 3D printing, and polymers with high printability and high resolution don't have ideal conductivity for electrode applications. Therefore, converting these printed polymers into electrically conductive carbon frameworks is a promising route for fabricating high-resolution, easily prepared 3D electrodes. However, carbonization typically requires high-temperature pyrolysis, which introduces challenges such as structural shrinkage, deformation, and low carbon yield, ultimately limiting the effectiveness of the resulting 3D electrodes. This dissertation presents a systematic approach to the fabrication and performance enhancement of three-dimensional (3D) printed carbon electrodes for advanced supercapacitor applications.

Chapter one outlines the growing importance of architected 3D electrodes enabled by additive manufacturing, highlighting current limitations in conductivity, surface area, and scalability of polymer-derived carbon structures. This chapter summarizes the current additive manufacturing process for preparing 3D electrodes and the limitations of converting polymer-based 3D templates into carbonaceous 3D electrodes.

Chapter two investigates the role of transition-metal-based catalysts in the pyrolytic conversion of PR48-based 3D-printed polymers into conductive carbon frameworks, with an emphasis on char yield, structural retention, and graphitization.

In Chapter three, tannic acid is introduced as an additional carbon precursor alongside the best graphitization catalyst we found in the previous chapter, $FeCl_3$, to significantly improve carbon yield and structural retention and generate hierarchical, high-surface-area 3D carbon architectures with enhanced ion accessibility and electrochemical performance.

Chapter four further improves electrode performance by growing a secondary pseudocapacitive polydiaminonaphthalene (PDAN) layer on our 3D carbon electrodes, which synergistically enhances charge storage through combined electric double-layer and redox mechanisms. This integrated strategy demonstrates a scalable route to high-performance 3D electrodes with improved capacitance, structural integrity, and tunable electrochemical properties, offering a promising pathway for next-generation energy storage systems.

In summary, we demonstrate a facile post-processing catalyst infiltration strategy that enhances the carbon conversion ratio while preserving the intricate structures of 3D-printed polymer electrodes. Moreover, the as-prepared 3D carbon electrode can serve as an ideal scaffold for integrating active materials, such as conducting polymers, to further improve electrochemical performance. This approach provides a promising material for developing scalable, sustainable, and high-performance electrodes in energy storage applications.

Chapter 1 - Introduction of 3D carbon supercapacitor: operating principles, significance and future potential

1.1. Introduction to 3D carbon supercapacitor

With the depletion of fossil fuels and growing concerns about global warming, the development of efficient energy storage and conversion technologies is essential to meet the growing global demand for sustainable energy solutions. Electrochemical energy storage systems, such as batteries, fuel cells, and supercapacitors, have attracted increasing attention, and each has its own advantages and limitations, determining their unique applications. Fuel cells offer high efficiency and low emissions by directly converting chemical energy into electrical energy, but their application remains limited by high cost, system complexity, and fuel supply issues. Batteries are widely used for their high energy density, compact size, and stable performance, making them indispensable in portable electronics, electric vehicles, and large-scale energy storage. However, the application and performance of batteries are strongly limited by their short cycle life, slow charge and discharge kinetics, safety concerns, and environmental issues.

Supercapacitors, on the other hand, are distinguished by their high-power density up to 10000 W/kg, rapid charge–discharge behavior in seconds to a few tens of seconds, and long operational lifetime up to 100000 cycles, which render them highly effective in applications requiring rapid energy delivery and frequent cycling **(Table 1.1)**. [1–3] These characteristics make them highly attractive for applications requiring fast energy delivery and frequent cycling, from renewable energy integration to portable electronic devices and electric vehicles. In addition, supercapacitors can complement batteries by bridging the gap between high energy density and high-power output, thereby improving the overall efficiency and reliability of energy storage systems. As demand for sustainable, high-performance power technologies continues to grow, the development of advanced supercapacitors has become increasingly important for next-generation energy storage applications. The biggest differences in energy storage mechanisms separate supercapacitors (SCs) from batteries. Therefore, any technological advancement aimed at improving SC performance should preserve the unique operational characteristics that differentiate SCs from battery systems.

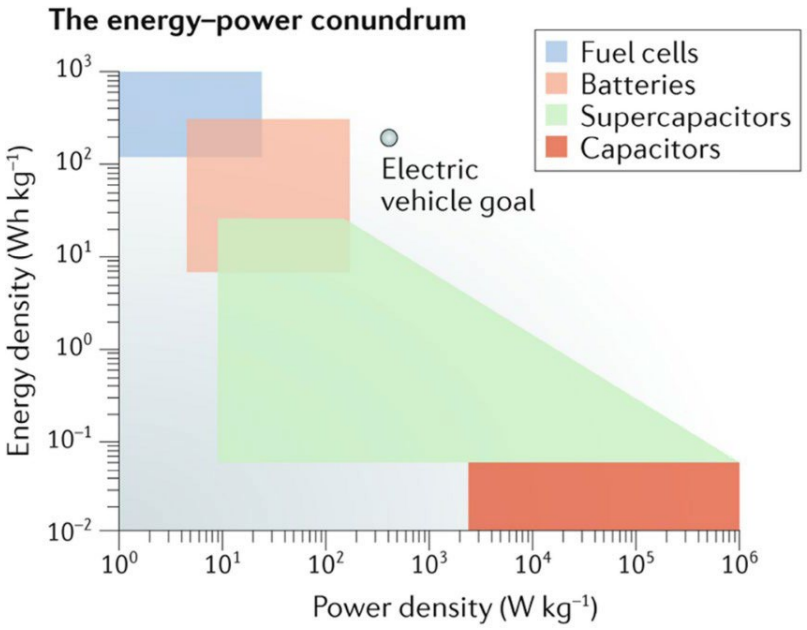


Figure 1.1. Ragone plot of different electrochemical energy storage devices. [3]

Table 1.1. Electrochemical properties of supercapacitors and batteries. [2]

Characteristics	Supercapacitors	Batteries
Specific energy (Wh/kg)	1~10	10~100
Specific power (W/kg)	500~10000	< 1000
Energy storage	Surface area (limited)	Bulk materials (High)
Charge/discharge rate	Fast (seconds to a few ten of seconds)	Slow (kinetic limited)
Cycle life	> 500000 cycles	~ 1000 cycles
Cycle life limitation	Side reactions	Chemical reversibility and mechanical stability
Coulombic efficiency	> 85 %	70 ~ 85%

1.2. Charge storage mechanisms of supercapacitors

Conventional capacitors consist of two electrodes divided by a dielectric layer. Supercapacitors (SCs) are energy storage devices that combine the high energy storage capability of batteries with the high-power delivery capability of capacitors. The basic structure of a supercapacitor is similar to that of conventional capacitors, and SCs can be classified into three main types: electric double-layer capacitors (EDLCs), pseudocapacitors, and hybrid supercapacitors. (**Figure 1.2)**

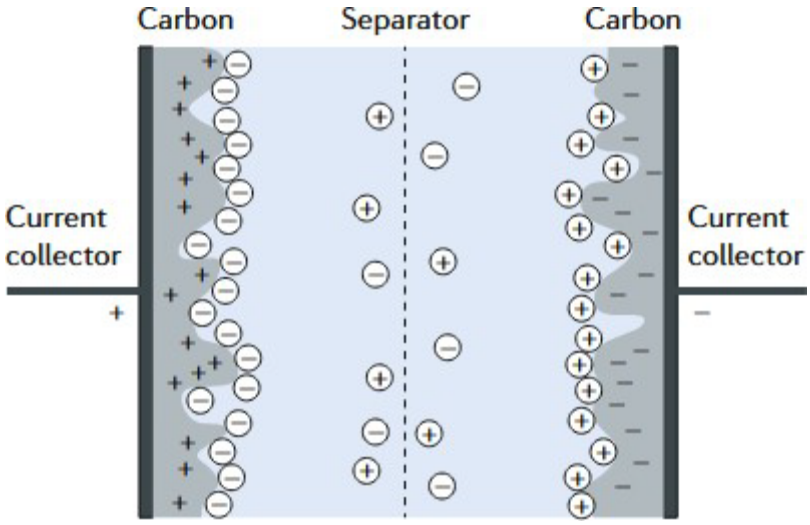


Figure 1.2. Basic configuration of supercapacitors. The supercapacitor consists of two symmetric porous carbon electrodes sandwiched between two current collectors and separated by an isolated separator. [4]

1.2.1. Electric double-layer capacitors (EDLC)

Electric double-layer capacitors (EDLCs), the oldest form of supercapacitors, often employ porous materials such as activated carbon, carbon aerogels, and carbon nanotubes, which provide abundant surface sites for charge accumulation and exhibit higher energy density than conventional capacitors because of their much larger specific surface area, which is defined as the total surface area of a solid per unit mass. In contrast, pseudocapacitors store charge through rapid, reversible redox reactions and ion intercalation at the electrode/electrolyte interface. Common pseudocapacitor materials include conductive polymers and transition metal oxides, both of which can change oxidation state during charge storage. The third type, hybrid supercapacitors, combines the advantages of both EDLC and pseudocapacitor mechanisms, as illustrated in **Figure 1.3**.

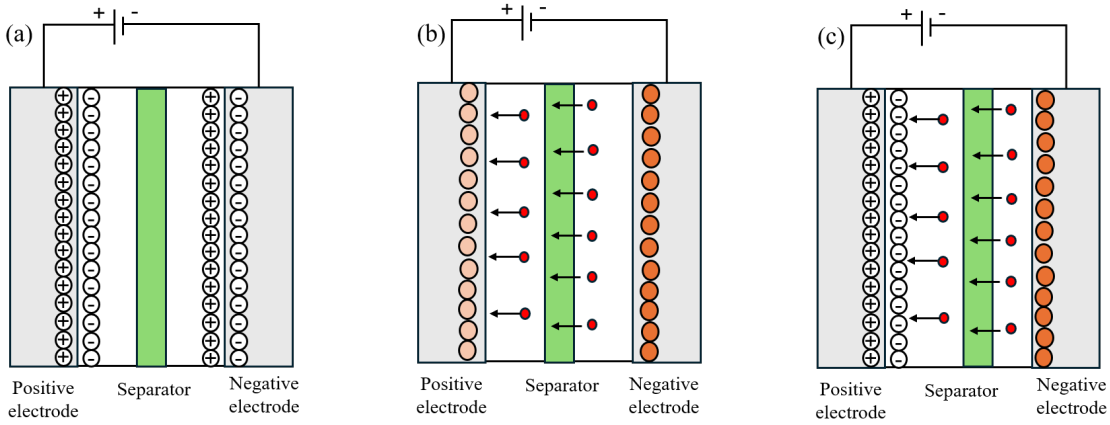


Figure 1.3. Different types of supercapacitors: (A) EDLC type, (B) pseudocapacitor type, (C) hybrid capacitor type. [2]

The primary energy storage mechanism in EDLC supercapacitors is the reversible electrostatic accumulation of ions on the electrode surfaces, which can be attributed to three basic models: the Helmholtz model, the Gouy−Chapman model, and the Stern model. The Helmholtz model, proposed in 1853, describes

charge separation at the electrode/electrolyte interface upon electrode polarization. Under this condition, oppositely charged ions migrate through the electrolyte and accumulate near the other electrode surface, forming a layer a few nanometers thick and arranged in a plane parallel to the electrode, thereby maintaining charge neutrality.
This accumulation of charge is known as the electrical double layer (EDL). [2,5] As the distance (d) between the ions and the electrode surface increases, the electrostatic potential around the electrode decreases. (**Figure 1.4.a**) The simplified Helmholtz double-layer (DL) capacitance is given by **Equation 1. 1.**

$$\boldsymbol{C_H = \varepsilon_0 \varepsilon_r \frac{S}{d} \ldots\ldots Euqation\ 1.1}$$

where ε_0 is the vacuum permittivity ($\varepsilon_0 = 8.854\times10^{-12}$ F/m), ε_r is the relative permittivity of dielectric electrolyte, S is the surface area of electrode, and d is the effective thickness of Helmholtz double layer, which is often approximated as the Debye length.

However, because the Helmholtz model does not account for ion diffusion in the electrolyte or for interactions between solvent dipoles and the electrode surface, Gouy and Chapman proposed another model of the EDL in 1910. According to this model, the electrostatic potential decays exponentially from the electrode surface toward the bulk electrolyte (**Figure 1.4.b**).

The Gouy-Chapman model is insufficient for highly charged double layers. Therefore, in 1924, Stern developed a revised model that combines the Helmholtz and Gouy-Chapman models, accounting for the motion of ionic species in the diffuse layer and the accumulation of ions near the electrode surface. (**Figure 1.4.c**) The two layers in the Stern model (Stern/Helmholtz layer and diffusion layer) can be treated as two capacitors connected in series; the total capacitance of the double layer can be expressed by **Equation 1.2.**

$$\frac{1}{C_{DL}} = \frac{1}{C_{Helmholtz}} + \frac{1}{C_{diffusion}} \ldots\ldots Equation\ 1.2$$

The previous equation is derived from a supercapacitor with a planar electrode surface; EDL behavior is determined by the electric field distribution, the nature of the electrolyte ions, the solvation of the electrolyte by solvent, and the specific interactions between adsorbed ions and the electrode surface. However, the electrodes in high-performance supercapacitors are typically high-surface-area porous materials; their EDL dynamics are more complex than those predicted by an idealized planar model. Within these confined architectures, ion transport is strongly affected by steric hindrance, tortuous diffusion pathways, internal ohmic resistance, and the wettability of the pore surfaces.

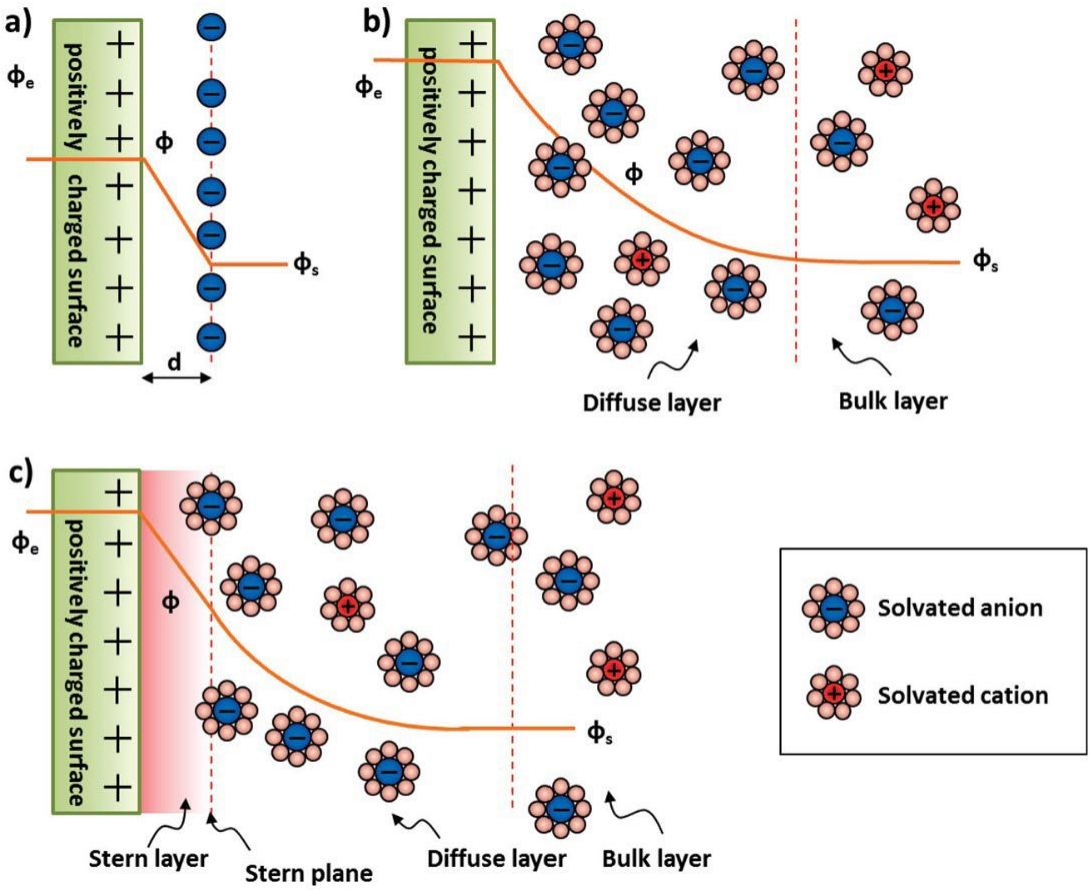


Figure 1.4. (a) Helmholtz, (b) Gouy-Chapman, and (c) Stern Model of the electrical double layer formed at a positively charged electrode in aqueous electrolyte. The electric potential (ϕ) decreases when transitioning from the electrode (ϕe), the bulk electrolyte away from the electrode surface (ϕs). The Stern plane defines the closest approach between ions and the charged surface. The Stern layer is free of mobile ions, while the diffuse layer begins farther from the electrode surface, typically within 10 to 100 nm. [5]

In a porous carbon electrode-based EDLC, when an electric potential is applied, electrostatic charges and electrolyte ions accumulate at the electrode/electrolyte interfaces to maintain charge neutrality. Specifically, the negative surface charge on the cathode is balanced by an equal number of accumulated cations, while the positive surface charge on the anode is balanced by attracted anions. (**Figure 1.5**) Consequently, a two- electrode supercapacitor behaves as two independent double-layer capacitors connected in series, where the total equivalent capacitance (C) is expressed according to **Equation 1.3**

$$\frac{1}{C} = \frac{1}{C_+} + \frac{1}{C_-} \dots\dots Equation\ 1.3$$

Where $CC+$, $CC-$ and C are the capacitance of the positive electrode, negative electrode and the full device.

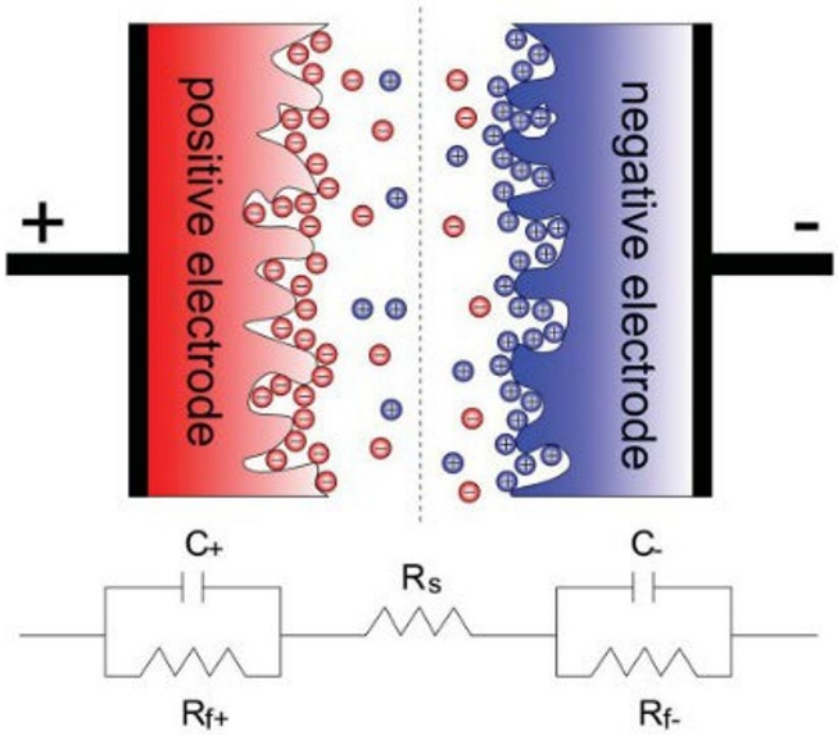


Figure 1.5. The charge state of symmetric porous carbon electrode EDLC and its corresponding equivalent circuit. R represents resistors and C represents capacitors. [5]

1.2.2. Pseudocapacitance

Although increasing surface area by tailoring porous structure and the surface roughness can optimize performance, the maximum achievable capacitance of conventional EDLCs remains fundamentally limited. Consequently, achieving high energy densities demands alternative technological approaches. Pseudocapacitors involve fast, reversible redox reactions that correspond to the charge and discharge processes. [2,6] Owing to the Faradaic charge-transfer process, pseudocapacitors can achieve higher capacitance and, consequently, higher energy density than EDLCs. As a result, pseudocapacitors can offer improved device performance relative to EDLCs. There are three main pseudocapacitive mechanisms: underpotential deposition, redox pseudocapacitance, and intercalation pseudocapacitance. (**Figure 1.6**) Pseudocapacitance typically arises from specific electrode materials, including transition-metal oxides [4–9], conducting polymers (such as polyaniline, polypyrrole, etc.) [10–15], and heteroatom-doped carbons (O-doped or N-doped) [7–11]. Alternatively, pseudocapacitance charge storage can originate from redox reactions of active electrolyte species.

The first mechanism is underpotential deposition **(Figure 1.6.a)**; it occurs when metal ions form an adsorbed monolayer on the surface of another metal at a potential higher than the metal ions' equilibrium redox potential. The second is redox pseudocapacitance (**Figure 1.6.b**); it occurs when ions are electrochemically adsorbed onto the electrode surface and is accompanied by Faradaic charge transfer. The latter is intercalation pseudocapacitance **(Figure 1.6.c)**, which occurs when ions insert into the interstitial sites or layers of a redox-active material and involves Faradaic charge transfer without inducing a crystallographic phase transition. [6]

Underpotential deposition (UPD) is a mechanism in which metal ions deposit onto a different substrate at a potential higher than their equilibrium potential because interactions between the depositing metal and the substrate are stronger than the cohesive forces between the depositing metal atoms themselves. A typical example is the deposition of copper onto a gold electrode. [12] Generally, UPD happens when a metal with

a lower work function is deposited onto one with a higher work function. However, because UPD is highly sensitive to environmental factors and complex synergistic effects, its exact mechanism remains unresolved, limiting its practical applications.

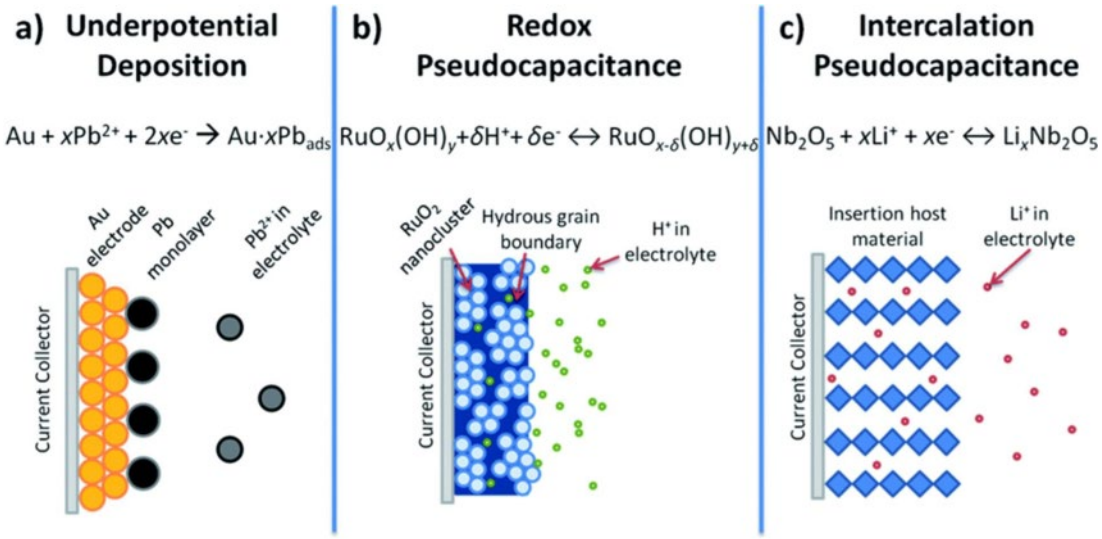


Figure 1.6. Different types of reversible redox mechanisms that give rise to pseudocapacitance: (a) underpotential deposition, (b) redox pseudocapacitance, and (c) intercalation pseudocapacitance. [6]

Redox pseudocapacitance is the most common charge-storage mechanism that bridges the gap between conventional capacitors and batteries. In this mechanism, electrolyte ions are electrochemically adsorbed onto or near the electrode surface, where they participate in rapid Faradaic charge-transfer reactions that enable energy storage. [2,6,13] Ruthenium oxide (RuO_2) is a great example of a pseudocapacitive material. Due to its excellent electrical conductivity and highly reversible surface redox chemistry, its electrochemical performance in acidic electrolyte has been widely investigated in recent years. [1,6,14,15] In particular, amorphous hydrous ruthenium oxide ($RuO_2{\cdot}xH_2O$) exhibits higher specific capacitance (720 F/g) than anhydrous ruthenium oxide. The improvement of the hydrous product is attributed to the mixed proton–electron conductivity of the hydrous structure, in which surface-confined redox reactions proceed through a coupled proton–electron double injection and expulsion mechanism, as described in the following reaction:

$$RuO_x(OH)_y + \delta H^+ + e^- \rightarrow RuO_{x-\delta}(OH)_{y+\delta}$$

where $RuO_x(OH)_y$ and $RuO_{x-\delta}(OH)_{y+\delta}$ represent the interfacial oxyruthenium species at higher and lower oxidation states. In acidic media, the charge can be stored via redox transitions among different oxyruthenium states, such as Ru (IV)/ Ru (III)/ Ru (II). [14,15]

Intercalation pseudocapacitance is the third charge-storage mechanism in pseudocapacitors and is observed in materials with intrinsic tunnels or layered structures. [2] In this process, electrolyte ions are inserted into the internal channels or interlayer spaces of the host material and undergo rapid Faradaic redox reactions. Unlike the intercalation processes in lithium-ion batteries, this mechanism proceeds without a phase transition of the active material. Due to its unique advantages, a growing number of novel materials have been developed based on intercalation pseudocapacitance, demonstrating excellent electrochemical performance and considerable potential for high-rate energy storage applications. MnO_2 is another popular pseudocapacitor material; it can store charge through the variable valence states of Mn. [1,6,13,16–18] For a MnO_2 electrode, ions from the electrolyte are reversibly adsorbed and desorbed at or near the electrode surface by electrochemical reactions, which can be expressed as: [16]

$$(MnO_2)_{surface} + M^+ + e^- \rightarrow (MnO_2^- \ldots M^+)_{surface}$$

where M^+ = metal cations in electrolyte. The metal ions in the electrolyte can be attracted to the oxygen atom in the MnO_6 octahedron structure, and the charges transfer to adjacent Mn atoms, which change Mn^{4+} to

Mn^{3+}. [19] The electrolyte cations or protons can store charge via intercalation and deintercalation within the bulk phase of MnO2-based electrode materials [16,17], which can be expressed as:

$$MnO_2 + M^+ + e^- \rightarrow MnOOM$$

where M^+ = metal cations in the electrolyte. However, the bulk capacitance of MnO_2 is limited by its poor electrical conductivity and slow ion diffusion; its pseudo-capacitive behavior is strongly dependent on the thickness of the subsurface layer.

1.2.3. Hybrid capacitor

Hybrid capacitors are promising energy storage devices that can bridge the gap between supercapacitors and batteries. They generally offer higher specific capacitance and energy density than electric double-layer capacitors and pseudocapacitors, while maintaining higher power density but lower energy density than batteries. Typically, hybrid capacitors consist of one electrical double-layer electrode paired with either a pseudocapacitive electrode or a battery-type electrode. [2] These asymmetric hybrid supercapacitors can achieve both high energy and power densities by combining different materials. For hybrid capacitors, ion adsorption and desorption occur at the EDLC electrode, and ion intercalation/deintercalation occur at the battery-type electrode simultaneously under working conditions, enabling high energy delivery at high power output while maintaining long cycle life.

1.3. Carbon-based supercapacitors

There are several critical factors in the selection of electrode materials for supercapacitors, including high specific surface area, an interconnected pore network, pore sizes tailored to the dimensions of electrolyte ions, high electrical conductivity, strong wettability with the electrolyte, and the presence of electrochemically stable surface functional groups. [1,3,5,19,20] Carbon is one of the most widely used supercapacitor materials, due to its low cost, abundant sources, high electrical conductivity, large surface area, and stable long-term cycling stability. [5,8,20,21] Therefore, carbon materials with diverse microstructures and broad availability are highly attractive for energy storage applications. Recent studies indicate that the pore size and shape within these materials are critical factors; they not only facilitate efficient energy storage via battery-type or intercalation pseudocapacitive mechanisms but also directly dictate the resulting electrochemical performance. [5,20]

Nanostructured carbon-based materials are one of the most widely employed as electrodes for EDLCs because of their high surface area, excellent electrical conductivity, low cost, environmental compatibility, simple synthesis, and outstanding chemical, electrochemical, and thermal stability. [20] Historically, activated carbons (ACs) with large specific surface areas have been the most commonly used materials. [20] Nowadays, advanced carbon nanostructures such as carbon nanotubes (CNTs) and graphene have attracted increasing attention. Graphene possesses excellent mechanical and structural properties, high carrier mobility, large specific surface area, and superior chemical stability.

1.3.1. Activated carbons (ACs) based supercapacitors

Activated carbons (ACs) are the most widely used carbon electrode materials due to their large specific surface area, good electrical properties, and low cost, and can be produced by physical or chemical activation of various carbon precursors (such as wood, coal, and other biomass materials). Physical activation is generally carried out at high temperatures, typically 700–1200 °C. In contrast, chemical activation is performed at a lower temperature range, typically 400-700 °C, using activating agents such as phosphoric acid, potassium hydroxide, sodium hydroxide, or zinc chloride to etch the template surface, thereby increasing the surface area. The CO_2 and KOH treatments are two of the most widely used techniques. [22–24] Depending on the activation method and the precursor employed, ACs with a wide range of physicochemical properties and surface areas up to 3000 m^2/g can be obtained and investigated for electrochemical applications. The porous structure of activated carbons usually exhibits a broad pore-size distribution, including micropores (<2 nm), mesopores (2–50 nm), and macropores (>50 nm). However,

many studies have shown that capacitance does not scale proportionally to surface area, suggesting that not all pores store charge effectively. [25] Therefore, in addition to surface area, the pore-size distribution, pore shape, electrical conductivity, and surface functionality are critical factors that determine the electrochemical performance of ACs.

In addition to the porous structure of ACs, surface functionalities also play an important role in determining carbon electrode performance by influencing electrolyte wettability and contributing additional pseudocapacitance. An activated carbon with a high concentration of oxygen-containing functional groups and relatively low porosity (BET specific surface area = 270 m^2/g) was prepared by one-step carbonization of an oxygen-rich seaweed biopolymer. [26] This material exhibited good electrochemical performance, delivering an energy density of 10 Wh/kg even at high power densities approaching 10 kW/kg in acidic electrolyte. [26] Moreover, its capacitance remained stable after 10,000 cycles, suggesting that the carbon surface contained relatively few catalytically active sites, likely because of its comparatively small specific surface area. Therefore, both surface functionality and porosity should be carefully optimized to improve long-term performance.

As a result, ACs have been widely investigated as supercapacitor electrode materials; however, their limited energy storage and low-rate capability restrict their commercial applications. To improve energy storage performance, ACs need to have a high specific surface area, interconnected pores, and a narrow pore-size distribution. Even though ACs have high specific surface area, precise control of pore size and distribution remains a major challenge. Therefore, other carbon-based materials have been considered as candidates for supercapacitors. Also, in most cases, these carbon materials are powders and require binder chemicals to fabricate final electrodes, which can only be 2D sheet electrodes. The binder not only shields the carbon's active surface area but also exhibits poor long-term stability.

1.3.2. Carbon Nanotubes (CNTs) based supercapacitors

Carbon nanotubes (CNTs) have attracted considerable attention for supercapacitor electrode applications because of their unique pore structure, highly accessible surface area, excellent electrical conductivity, and good mechanical and thermal stability. [5,20,27,28] For energy storage applications, ideal electrode materials must have high active surface areas to facilitate electrochemical processes with highly controllable architectures. The good electrical conductivity and highly accessible surface area make CNTs a good choice for high-power electrode materials, and the high mechanical integrity and open structure also make them a good electrode to composite with other active materials. [29] 2D CNT films are considered promising electrodes for flexible energy storage and conversion devices due to their structural flexibility, low weight, high conductivity, and ease of fabrication. [30] Moreover, the interconnected pores within the CNT film enable coordination with other active materials. For instance, Aval et al. fabricated a symmetric supercapacitor with 2D CNT electrodes and a polyvinyl alcohol (PVA)/H_2SO_4 gel electrolyte, which exhibits 164 F/g at 150 mV/s and 411 F/g at 20 mV/s, and a specific capacitance of 520 F/g at 0.06 mA/cm^2. [31] Cao et al. reported a new type of highly stretchable supercapacitor with an aligned CNT forest as the electrode, which can sustain 800% stretchability and exhibit an areal capacitance of 5 mF/cm^2 at 50 mV/s. [32] Moreover, the CNT electrode can be incorporated with other active materials, such as graphene [33], conducting polymers, and metal oxides (MnO_2 [34], MoS_2 [35], and Co_3O_4 nanoparticles [36]).

Although ACs deliver high specific surface area and CNTs provide excellent electrical conductivity and 1D charge-transport pathways, both are still constrained by ion diffusion resistance and limited electrolyte accessibility. To address these limitations, three-dimensional (3D) carbon architectures—including hierarchical porous networks, CNT/graphene scaffolds, and 3D printed monoliths—have attracted growing interest for simultaneously maximizing accessible surface area, preserving continuous conductive pathways, and enabling efficient ion transport; the next chapter will therefore focus on how to use additive manufacturing f or 3D electrodes fabrication, examining how their design principles, fabrication strategies, and resulting electrochemical properties enhance performance in supercapacitors and related energy storage devices.

1.4. 3D supercapacitors

Traditionally, the primary focus of energy storage performance research has been the intrinsic properties of active materials; however, architectural design has attracted increasing attention as a means of enhancing electrochemical performance. [3,37] Previous research has already shown that thicker electrodes can increase the active materials component in the energy storage device, while simultaneously enhancing energy and power densities. (**Figure 1.7**) Conventional 2D electrodes are usually prepared by simple slurry casting of active materials onto current collectors; by contrast, 3D electrodes offer many more advantages: [3,37]

- Precise control over complex geometries
- Broad material compatibility, allowing all kinds of materials such as polymers, carbon, ceramics, metals, and other composites for 3D electrodes
- Direct deposition of active materials on the 3D structure
- Formation of interconnected porous architecture for ion and electron transport
- High-resolution fabrication
- Efficient and eco-friendly manufacturing process
- Higher active materials content in the overall energy storage device

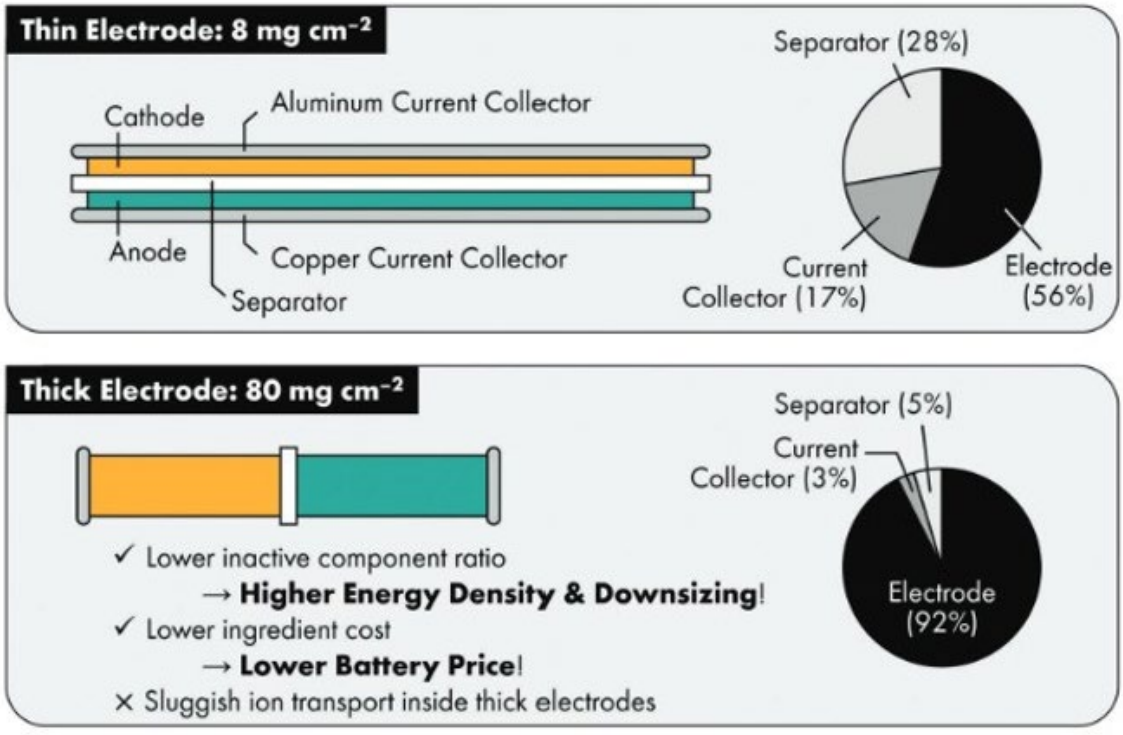


Figure 1.7. The cell configuration of thin and thick electrodes with the weight ratios of the electrodes to other inactive materials (current collectors and separators). [22]

1.4.1. 3D printing supercapacitor

The fabrication of electrodes is a crucial step in supercapacitor manufacturing. 3D printing (3DP) has become a promising technology for fabricating electrochemical energy storage devices, offering high design freedom, shape conformality, and material versatility. In the past, the primary focus in the performance of energy storage systems was on the intrinsic properties of the active material; however, electrode architecture also plays a critical role in enhancing electrochemical performance and has recently attracted increasing attention. The global 3D printing market was valued at approximately $20.37 billion in 2023 and is projected

to reach $135.4 billion by 2033, growing at a compound annual growth rate of 21.2% from 2023 to 2033. (**Figure 1.8**) [38]

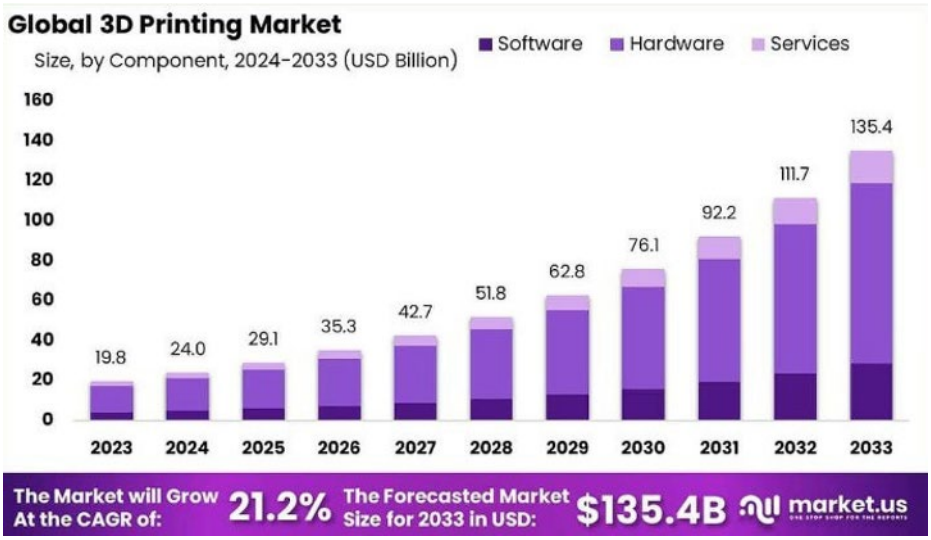


Figure 1.8. Approximate global 3D printing market during the 10 years from 2023 to 2033. [38]

Additive manufacturing, especially 3DP, has been a useful tool for the design and fabrication of high-performance energy storage devices. Compared with traditional 2D electrodes, which are usually prepared by slurry casting of active materials onto current collectors, 3D-printed electrodes offer the following advantages.

(1) 3D printing offers precise control over complex structural design.
(2) Direct deposition of active materials onto a 3D structure without additional treatment
(3) A much wider range of material selection; 3D printing can be used for polymers, carbons, ceramics, metals, and composite materials.
(4) 3D printing can form interconnected porous structures for better ion transport.
(5) 3DP is a more efficient and eco-friendlier manufacturing process that reduces material waste.

3D printing techniques are a broad term encompassing various methods for fabricating 3D electrodes, building functional material layer by layer according to computer-aided design (CAD) models. These 3DP methods enable precise control over structure and material composition, making them highly attractive for fabricating 3D electrodes. The major 3DP approaches used for electrode fabrication can be broadly classified into several categories:

(1) Material extrusion: Direct ink writing (DIW) [3,21,37,39,40] and fused deposition modeling (FDM) [3,37,41,42]
(2) Laser powder bed fusion: Selective laser sintering (SLS) [3,37]
(3) Vat polymerization: Stereolithography (SLA), digital light processing (DLP), direct laser writing via 2-photon polymerization (DLW-2PP), projection micro stereolithography (PμSL), and continuous liquid interface production (CLIP).

1.4.1.1. Direct ink writing (DIW)

Direct ink writing (DIW), which offers a wide range of ink materials and high-resolution capability, is the most widely used 3D printing method for fabricating 3D electrodes in energy storage devices. The working mechanism of DIW printing is exhibited in **Figure 1.9**. The viscous ink is extruded out through the nozzle and constructs a 3D structure. The DIW ink can be composed of a wide range of materials, including

polymers, metals, ceramics, and composites, that must exhibit rheological properties.

A critical rheological requirement for DIW is the shear-thinning effect: the ink must flow easily under pressure during extrusion and rapidly recover its shape after deposition, so that filaments do not collapse or fuse during 3D printing. The printability of DIW is governed by both material formulation and printing parameters, such as nozzle diameter, extrusion pressure, printing speed, the ratio between extrusion rate and printhead movement, filament stretching, and resolution. Smaller nozzles generally improve resolution but demand higher pressures and increase build time. After printing, solidification—via solvent evaporation, gelation, photocuring, or thermal treatment—stabilizes the structure prior to any post-processing. [39,40]

DIW is the most versatile 3D printing technique for the broadest range of materials; other 3D printing methods have their own limitations in material selection. For instance, fused deposition modeling (FDM, also known as fused filament fabrication, FFF) is generally used for 3D printing thermoplastic polymers; digital light processing (DLP) and stereolithography (SLA) are typically used for photoresins. Therefore, DIW is the most common additive manufacturing method to generate 3D carbon structures. [39,40,43]

To make a 3D carbon electrode, we need a carbon-based ink for DIW; however, carbon cannot be transferred into a liquid state. For carbon-based DIW, the printing ink typically contains a carbon precursor or carbon-rich material, along with binders, rheology modifiers, or sacrificial components that preserve the printed shape until carbonization. During carbonization, organic components and binders are converted into a conductive carbon network while volatile species are removed, leaving a porous carbon architecture with extremely high specific surface area but low mechanical integrity.

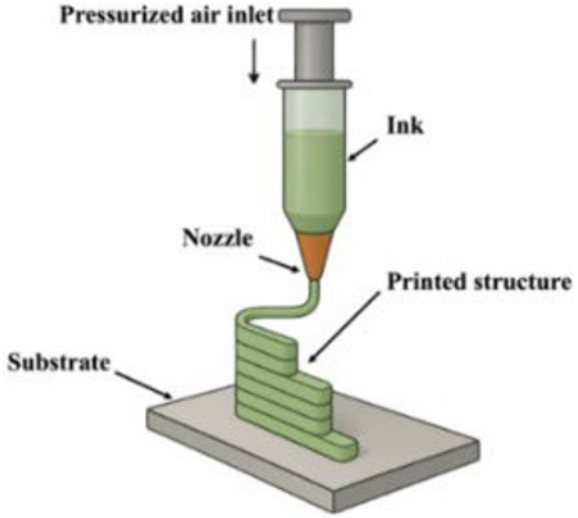


Figure 1.9. Schematic of the direct ink writing process. [43]

1.4.1.2. Fused deposition modeling (FDM)

Fused deposition modeling (FDM), also known as fused filament fabrication (FFF), is another material-extrusion-based 3DP technology widely used to fabricate complex products. FDM technology employs a mechanism similar to that of DIW but uses solid thermoplastic filaments as printed material. [41,44] The most common thermoplastic filament materials utilized in the FDM technique are polystyrene (PS) [45], polypropylene (PP) [46], acrylonitrile butadiene styrene (ABS) [47], and polylactic acid (PLA) [42,48].

The solid thermoplastic filaments are heated to their melting temperature in the machine, and then the molten material is extruded layer by layer through a nozzle. When the materials leave the nozzle, they cool and solidify immediately, forming 3D structures. Similar to DIW, FDM also uses CAD software to control the

movements of the nozzle and extrusion head. The working mechanism of FDM printing is exhibited in **Figure 1.10**. FDM is widely used as a 3D printing technology, but it is rarely used in energy storage devices because thermoplastic filaments have low electrical conductivity. Therefore, other conductive nanomaterials, such as graphene oxide, CNT, carbon black, and metallic materials, can be mixed with thermoplastic filaments to enhance electrical conductivity. [43,44,48]

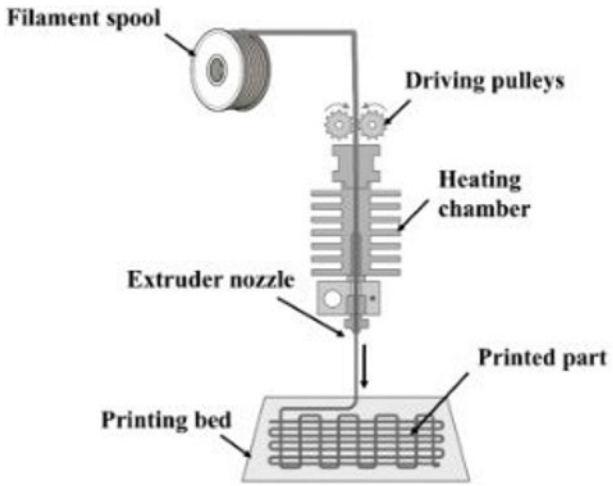


Figure 1.10. Schematic of the fused deposition modeling process. [43]

1.4.1.3. Power-bed selective laser sintering (SLS)

Selective laser sintering (SLS) is a powder-bed additive manufacturing process developed in the 1980s that uses a high-power laser to selectively fuse or sinter layers of powdered material into a solid part. The working mechanism of SLS printing is exhibited in Figure **1.11**. In the process, a thin layer of powder is spread across the build platform, the laser scans the cross-section of the part, and the platform lowers before the next layer is applied; the surrounding powder also acts as built-in support, allowing complex geometries without separate support structures. [49] SLS is widely used for rapid prototyping and low-volume production in industries such as aerospace, automotive, medical, consumer goods, and architecture. Its main advantages are design freedom, good mechanical performance, no support removal, and efficient use of material, while its drawbacks include high machine cost, the need for post-processing, limited material choices, surface roughness, and relatively long cooling and build times. The SLS mechanism uses a high-power laser to selectively melt and fuse material particles in a powder bed, including metallic, polymer, and ceramic particles. [37,43,49]

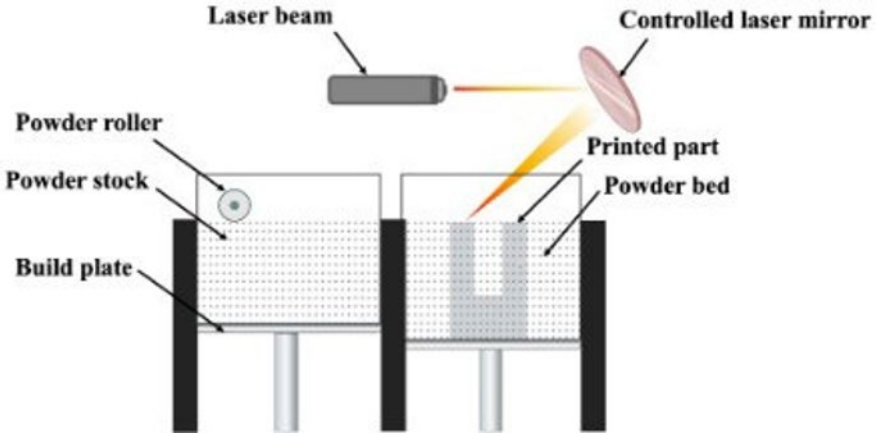


Figure 1.11. Schematic of the powder bed fusion process.[43]

1.4.1.4. Stereolithography (SLA)

Vat polymerization 3D printing is a huge category of additive manufacturing that use selective curing of photoresins to generate 3D structures, including digital light processing (DLP) [50,51], scanning stereolithography (SLA) [52,53], direct laser writing via 2-photon polymerization (DLW-2PP) [54,55], projection micro stereolithography (PμSL) [56,57], and continuous liquid interface production (CLIP) [58,59]. Stereolithography (SLA) [52,53] is a promising 3D printing technique for fabricating high-resolution architectures from photocurable resins with precise control of 3D structural design. The photocurable resins consist of cross-linkable monomers and oligomers with photo-initiators. In the 3DP process, specific ultraviolet (UV) light induces photopolymerization in the exposed area, solidifying the resin layer by layer with different patterns via a moving z-axis stage, forming a photo-crosslinked 3D architecture. [43]

The working mechanism of SLA printing is exhibited in **Figure 1.12**. In the stereolithography (SLA) technique, after the 3D printing process, the UV curing parameters, such as wavelength, intensity, and exposure dose, are also critical to achieving high mechanical integrity and structural accuracy in 3D-printed structures. The first key factor is the UV light intensity. The light intensity affects both the curing speed and the resin's penetration depth; with higher light intensity, the exposure time can be shortened to speed up the 3D printing process. The second key factor of SLA is exposure time. Underexposure leads to incomplete polymerization, while overexposure results in excessive cross-linking and structural brittleness. The SLA is usually followed by a post-curing process as the final step to ensure full polymerization and improve mechanical integrity. However, most commercially available photocurable resins are 100% polymeric, which limits their direct use in the fabrication of electrochemical devices. [37,43]

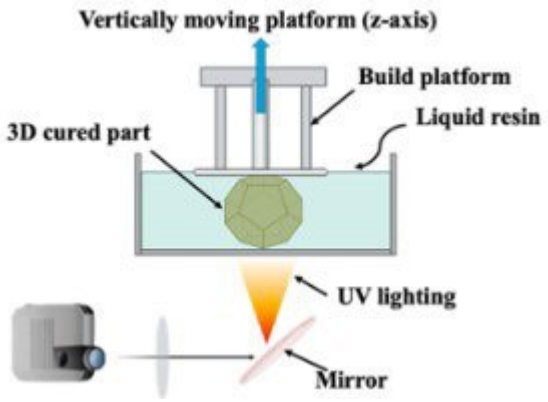


Figure 1.12. Schematic of the stereolithography process.[43]

1.4.1.5. Digital light processing (DLP)

Digital Light Processing (DLP) 3D printing is a resin-based additive manufacturing technique that uses a projected image of each layer to cure liquid photopolymer resin into a solid part, layer by layer. The working mechanism of DLP printing is exhibited in Figure 1.13. Introduced as an adaptation of digital projection technology, it became popular because it can cure an entire layer at once rather than tracing a path point by point, which greatly improves printing speed while maintaining high resolution. [43,50,51] It uses a digital micromirror device (DMD) - a chip containing millions of microscopic mirrors—to modulate and project light.

DLP works by projecting UV or visible light onto a vat of photosensitive resin, where the exposed regions undergo photopolymerization and harden into the desired cross-section; the build platform then moves to allow the next layer to be formed. Because of this mechanism, DLP is widely used for dental models

and appliances, jewelry, micro-mechanical parts, medical devices, customized manufacturing, and precision prototyping. Its main advantages are fast build speed, excellent detail resolution, smooth surface finish, and strong dimensional accuracy. [43,50,51] Its limitations include smaller build volumes, the relatively high cost and handling requirements of photopolymer resins, the need for cleaning and UV post-curing, and the fact that standard resin parts can be more brittle than thermoplastic prints.

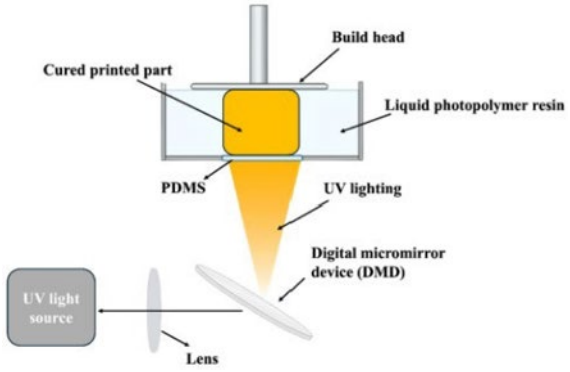


Figure 1.13. Schematic of the digital light processing method [43]

1.4.1.6. Direct laser writing via 2-photon polymerization (DLW-2PP)

Direct laser writing by two-photon polymerization (2PP) is a powerful technique that can generate complex 3D polymer structures with feature sizes down to 100 nm. [54,55] 2PP is a photochemical process initiated by the femtosecond laser beam focused tightly into the volume of the photosensitive resins by a high-numerical-aperture (NA) objective. A normal photopolymerization process consists of three steps: initiation, propagation, and termination. In the initiation process, the photoinitiators will reach the excited state by absorbing two photons and decompose into two free radicals. In the propagation step, radicals react with monomers to form monomer radicals, thereby initiating polymerization. The termination process occurs through multiple pathways: (i) radical combination, where two radicals recombine to form a single covalent bond [54] or (ii) disproportionation, involving hydrogen abstraction between chains to yield one saturated chain and one unsaturated chain. [54,55,60]

- Initiation process: $PI \xrightarrow{photons} PI* \rightarrow R\cdot + R\cdot$
- Propagation process: $R\cdot + M \rightarrow RM\cdot \xrightarrow{M} RMM\cdot + RM_n\cdot$
- Termination process 1: $RM_m\cdot + RM_n\cdot \rightarrow RM_{m+n}R$ (radical combination)
- Termination process 2: $RM_m\cdot + RM_n\cdot \rightarrow RM_mH + RM_n(=)$ (disproportionation)

where RM_mH means saturated polymer (gains H atom), and $RM_n(=)$ means unsaturated polymer with terminal C=C double bond (loses H atom)

This technique is widely used to fabricate micro- and nanostructures for photonics, microfluidics, tissue engineering scaffolds, micromechanics, and other devices that require submicron features and complex freeform geometries. Its main advantages are exceptional spatial resolution, design freedom, and the ability to create intricate 3D structures without masks, while its drawbacks include slow writing speed, limited build volume, expensive instrumentation, and the need for specialized photosensitive resins.

1.4.1.7. Projection micro stereolithography (PμSL)

Projection micro stereolithography (PμSL) is an advanced additive manufacturing technology that combines the top-down methodology of traditional stereolithography (SLA) with the mask-projection capability of digital light processing (DLP), producing complex, high-resolution microstructures by curing

photopolymer resins with ultraviolet (UV) light. [56,57] This process begins by converting a 3D model into a sequence of 2D digital patterns. These patterns are transferred to a digital micro-mirror device (DMD) chip, which controls the UV light source. The modulated UV light, with the same shape as the 2D patterns, then passes through the reduced lens that projects the patterns onto the resin surface at a reduced scale. Upon impact, the localized UV exposure triggers photopolymerization, solidifying a precise layer of the structure. A translational stage then lowers the printing platform, allowing the UV projection system to solidify the subsequent layer. This layer-by-layer sequence repeats continuously until fabrication is complete. A schematic illustration of this projection micro-stereolithography process is shown in **Figure 1.14.**

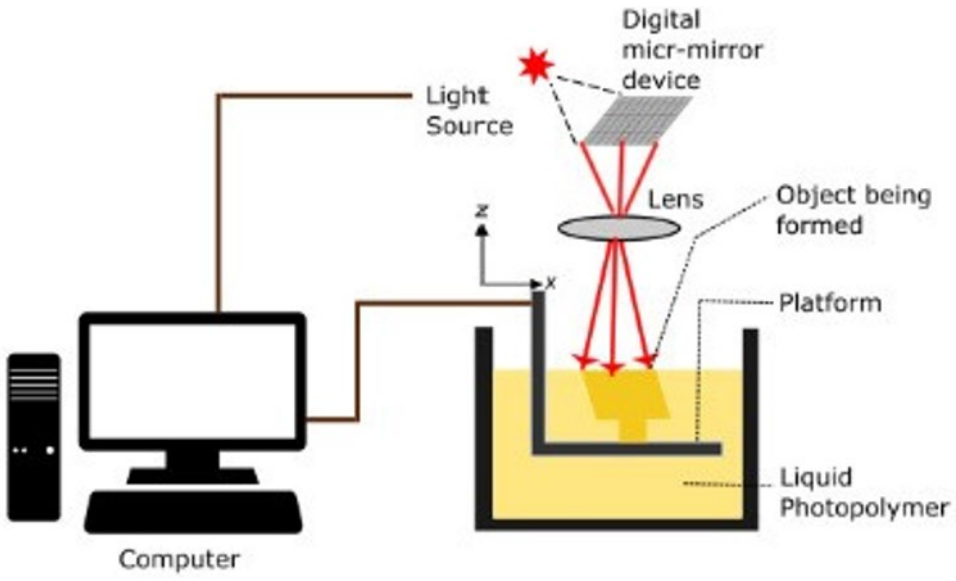


Figure 1.14. Schematic illustration of projection micro-stereolithography. [61]

1.4.1.8. Continuous liquid interface production (CLIP)

Continuous Liquid Interface Production (CLIP) is a photochemical 3D printing technology that "grows" objects continuously from a pool of liquid resin rather than building them layer by layer. This uninterrupted growth is achieved using an oxygen-permeable window positioned below the ultraviolet projector. The window allows oxygen to pass through, creating a "dead zone" - a persistent liquid interface where photopolymerization is inhibited—preventing the curing resin from adhering to the window. [58,62]

The detailed mechanism and operation of a CLIP are shown in **Figure 1.15**. The process works by projecting a continuous sequence of UV patterns from a digital light-processing (DLP) engine through a UV-transparent, oxygen-permeable window at the base of the resin pool. This creates a stable liquid "dead zone" directly above the window, keeping the interface beneath the advancing part entirely fluid. As the curing part is drawn upward continuously, the resulting suction forces continually draw in fresh resin. This process stands in sharp contrast to conventional bottom-up stereolithography, where UV exposure, part translation, and resin recoating must occur in separate, sequential steps.

The main advantages of CLIP are very high printing speed, smooth surface morphology, good mechanical properties, and the ability to produce complex parts without visible layer lines, while its drawbacks include proprietary hardware, limited material choices compared with other 3D printing processes, resin/post- processing requirements, and higher system complexity and cost. [58,62]

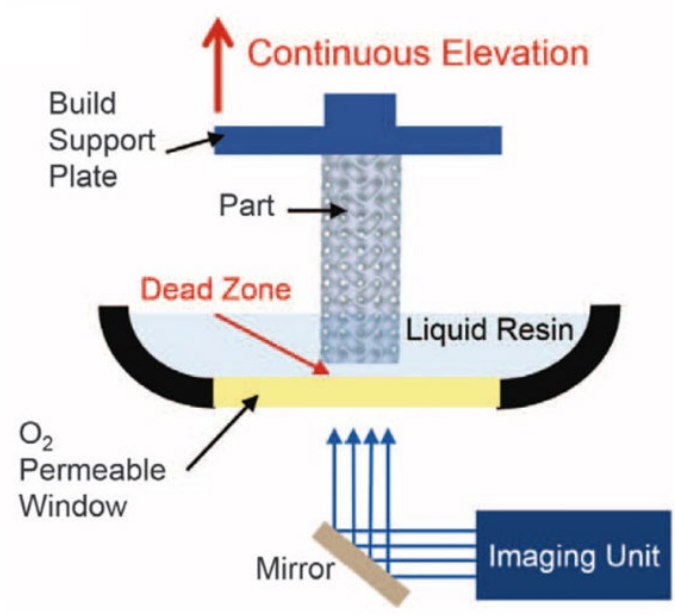


Figure 1.15. Schematic of CLIP continuous printing. The part is printed by elevating the build support plate while dynamically projecting 2D cross-sectional UV images. An oxygen-permeable window maintains a "dead zone" (a persistent liquid interface) beneath the rising part, preventing adhesion to the window. [58]

1.4.1.9. Limitation of 3DP electrode for energy storage

Nowadays, the applications of 3D printing in energy storage are limited by factors such as processing limitations, scalability, material properties, and cost. The most commonly used materials in 3D printing methods, such as polymers, suffer from low electronic conductivity, severe thermal degradation, and loss of mechanical integrity at high temperatures, limiting their application in most energy systems. [3,38,43,63] Another major problem with 3D-printed electrodes is mechanical integrity: they often exhibit lower mechanical strength than conventional 2D or bulk electrodes due to their high void fraction in 3D structures, which limits their use in high-stress energy components.

The second problem is cost and scalability: compared to conventional electrode manufacturing methods such as slurry casting, the 3D printing process is much slower and incurs higher production costs. Moreover, the selection of printable materials such as high-performance alloys, technical ceramics, and specialized polymer resins further increases the production costs of 3D printing. [40] Also, most 3D printing techniques are constrained by sample size, limiting their applicability to large-scale energy storage systems.

Last but not least, every type of 3D printing material has its own limitations. Polymers are the most widely used materials due to their ease of 3D printing and low fabrication costs. However, polymers possess low electrical conductivity, thermal stability, and mechanical strength, which limit their application in high- performance energy storage devices. Therefore, most 3D-printing polymers require post-treatments to address these problems. Metals, on the other hand, exhibit high conductivity and mechanical strength, making them ideal candidates for energy storage systems. However, the difficulty and high production costs of the 3D printing process, along with low chemical stability that requires additional post-treatment, strongly restrict its application.

1.4.2. 3D Pyrolytic Carbon for Energy Storage

Although 3D printing offers great geometric design freedom, the direct fabrication of pure carbon structures cannot be used without post-processing. To exploit the excellent electrical conductivity and chemical stability of carbon for 3D electrode applications, printed polymeric architectures must undergo pyrolysis. This high- temperature pyrolysis treatment under an inert atmosphere such as argon or nitrogen carbonizes the polymeric chains, converting them into conductive carbonaceous structures. Carbon materials produced by pyrolysis are generally classified into three types: amorphous, semicrystalline (glassy), and highly crystalline (graphitic). During pyrolysis, non-carbon elements in the polymer chain, such as oxygen and hydrogen, are removed as degradation gases, promoting graphitization and the formation of highly conductive sp2- hybridized carbon structures. The high electrical conductivity of glassy and graphitic carbon originates from their delocalized π-electrons, which exhibit high mobility throughout the material framework.

The synthesis of structurally stable glassy/graphitic pyrolytic carbon requires a high surface area-to-volume (SV) ratio to facilitate the escape of volatile byproducts generated during carbonization. If these volatiles become trapped during pyrolysis, the resulting internal stress can cause severe deformation and structural defects. In addition, thick solid structures often create high heat-transfer gradients, resulting in uneven temperatures between the surface and the bulk, further increasing structural heterogeneity. On the other hand, 3D printing polymer architectures with thinner struts and higher void fractions can shorten degradation gas diffusion paths, enabling rapid outgassing without structural deformation caused by internal stress from the high heat-transfer gradient.

Additive manufacturing is uniquely suited to this strategy because it can produce complex, high-SV architectures, such as beam-based lattices, that inherently satisfy these requirements. Accordingly, pyrolysis of 3D-printed polymer lattices offers an attractive and scalable route to pure carbon frameworks. This approach has been successfully used to create high-SV structures for applications in structural materials, heterogeneous electrocatalysis, biosensors, and renewable energy storage. Another major advantage of converting 3D-printed polymer architecture into carbon is the significantly improved mechanical integrity of the resulting frameworks. In conventional carbon printing methods, such as direct ink writing (DIW) and fused deposition modeling (FDM), carbon is typically introduced as a discrete particulate filler held together by sacrificial polymeric binders to ensure printability. To achieve sufficient electrical conductivity, these binders must subsequently be removed via high-temperature post-treatment. However, this binder burnout inevitably leaves behind a network of substantial voids and structural defects, severely compromising the mechanical strength of the final 3D architecture. Therefore, very limited mechanical data have been reported for conventional 3D-printed carbon structures (such as graphene aerogels). By contrast, the direct pyrolytic conversion of a continuous polymer precursor avoids these localized phase defects, yielding a far more cohesive and robust carbon structure.

Pyrolysis of carbon precursors to make carbon-based materials can be traced back to the production of charcoal in ancient times. In modern days, pyrolysis has been used to fabricate high-strength, electrically conductive carbon structures from carbon precursors. By combining the intrinsic material properties of carbon with architected 3D geometry, architected 3D pyrolytic carbon exhibits exceptional mechanical and functional properties that are significantly superior to those of bulk carbon materials. For energy storage applications, ideal electrode materials must have high active surface areas to facilitate electrochemical processes with highly controllable architectures. Consequently, activated pyrolytic carbon (PyC) derived from various organic precursors has been extensively investigated owing to its high specific surface area, making it an excellent candidate for advanced electrodes.

Today, additive manufacturing, also known as 3D printing, enables much more complicated structural geometries than conventional methods allow. Advanced laser-based micro- and nanofabrication 3D printing techniques have pushed these capabilities into the sub-micron, high-resolution regime. The primary challenge in fabricating three-dimensional architected pyrolytic carbon (PyC) structures is the polymer-to-carbon conversion that occurs during pyrolysis. Importantly, the physicochemical properties of

3D micro- and nano- architected PyC differ significantly from those of bulk PyC, largely due to size effects—especially pronounced in nano-architected materials—and the design freedom afforded by complex geometries. Also, we summarize current additive micro- and nanomanufacturing strategies for architected PyC, emphasizing their accessible geometric length scales and structural limitations.[48]

One of the most common methods for carbon microelectrode fabrication involves patterning an epoxy/acrylate-based photoresist using UV photolithography, followed by carbonization in an inert atmosphere. (Shown as **Table 1.2**) The standard process consists of projecting UV light through a light mask to selectively crosslink and solidify an exposed photoresist resin, allowing the resin in unexposed areas to be washed away in the following process. When combined with pyrolysis, this rapid, highly cost-effective, and precise structural control process transforms the resulting substrate-bound polymer structures into robust carbon architectures. In 2004, Marc Madou and his team fabricated high-aspect-ratio carbon microstructures (>10) using negative-tone photoresists, and Madou also coined the term "C-MEMS" (Carbon MEMS) for this breakthrough, a designation that now defines the modern intersection of photolithography and pyrolytic carbon synthesis. [49] However, bulky structures hinder the complete degassing of the precursor during pyrolysis because trapped gaseous products generate high internal pressure, which can eventually cause structural collapse and fracture. Therefore, the 3D-printed templates should have a high surface-to-volume ratio to facilitate gas release during pyrolysis and achieve ideal structure retention.

Stereolithography has emerged as a prominent method for fabricating 3D pyrolytic carbon structures, achieving a manufacturing resolution of roughly hundreds of μm. This is due to the low cost of commercial SLA printers, which offer reasonable printing quality and resolution, a straightforward fabrication process, and a wide range of commercial resins. For example, Wang et al. used SLA-printed pyrolytic carbon to fabricate a symmetric supercapacitor. [50] To further increase the specific surface area of the 3D pyrolytic carbon electrodes, they are activated with KOH. The KOH-activated 3D pyrolytic carbon electrode exhibits a 5.85-fold increase in cyclic voltammetry peak current density compared to conventional carbon paper. In addition to using 3D pyrolytic carbon directly as the electrode, Rezaei et al. also used SLA-printed pyrolytic carbon as a template to form Mn_3O_4/carbon hybrid supercapacitor electrodes. [51] The Mn_3O_4 active materials were deposited onto the 3D-printed polymer template via a one-step chemical reduction process, thereby improving the interfacial contact between the active materials and the final carbon template.

Table 1.2. Summary of sample feature sizes of current additive manufacturing used in combination with pyrolysis for generation of pyrolytic carbon template in energy storage applications. [63]

AM methods	Pyrolyzed feature size	3D printing resin or ink	Pyrolysis conditions	Ref
DIW	100 μm	Hydroxypropyl methylcellulose and GO	1050 °C (2 °C/min)	[18]
	600 μm	Cellulose and ZIF-8 MOF	1000 °C (5 °C/min)	[64]
FDM	500 μm	Cellulose, lignosulfonate mixture	1000 °C, various holds (0.2 °C/min)	[65]
	mm scale	polyacrylonitrile	1000 °C, 200 °C and 260 °C hold (0.5 °C/min)	[66]
DLP	133 μm	Elegoo	1000 °C and 900 °C at CO_2	[22]
	200 μm	Elegoo	1000 °C, hold at 400°C (10 °C/min)	[67]
	33 μm	Elegoo	1000 °C, hold at 400 °C (10 °C/min)	[68]
	28 μm	PR48	1000 °C, hold at	[69]

			300 and 400 °C (5 °C/min)	
SLA	316 μm	SU-8 2035, Formlabs HT V1	900 °C	[70]
	33 μm	Phenolic epoxy resin, methacrylate monomer, photoinitiators	400 °C 4 h hold, 1000 °C 4h (10 °C/min)	[71]
	15 μm	pentaerythritol tetraacrylate (PETA) and divinylbenzene (DVB)	300 °C 6 h hold (air, 10 °C/min), 900 °C 15 min (Ar, 3.3 °C/min), 880 °C 6 h (CO_2)	[72]

1.4.3. Selection of 3D printing resin for 3D pyrolytic carbon

To obtain ideal pyrolytic carbon structures for energy storage applications, selecting a 3D printing resin that forms a highly conductive pyrolytic carbon structure is critical. Various commercial resins have been used in 3D printing and pyrolysis to produce three-dimensional carbon structures; most of them are acrylate- or epoxy-based materials, including commercial resins such as PR48 [63,69,73–75], Elegoo [22,71,76], TEC PIC100 [77], etc. (**Table 1.3**)

These resins can yield conductive carbon after pyrolysis; however, they often suffer substantial dimensional shrinkage, frequently shrinking over 70%, and exhibit very low char yields. In addition to challenges associated with shape retention and char yield, pyrolytic carbon derived from polymer resins typically shows only moderate electrical conductivity. Although additional modifications, such as incorporating conductive materials like graphene oxide and using aromatic polymer precursors, have been introduced to increase char yield after pyrolysis, there is still significant room for improvement in achieving ideal pyrolytic carbon structures.

To achieve a well-defined pyrolytic carbon structure from a 3D-printed polymer precursor, four critical factors must be carefully considered: high char yield, high mechanical integrity, and high-resolution features. First, high char yield is essential because pyrolytic carbon is derived only from the fraction of the polymer that survives thermal decomposition; a higher char yield reduces mass loss, limits dimensional shrinkage, and helps preserve the structural geometry after pyrolysis. Secondly, high mechanical integrity is equally important because the printed polymer template must withstand the high stresses generated during the processing; weak or poorly crosslinked structures are more likely to warp, crack, or collapse as volatiles escape and the material densifies. Moreover, high-resolution features also matter due to the high surface-to-volume ratio. A higher Sv ratio helps ensure that degradation gases generated during pyrolysis are not trapped within the bulk polymer, thereby preventing the formation of distorted and hollow structures that would diminish the mechanical properties of 3D electrodes. In our work, we first selected PR48 as our carbon precursor due to its high-resolution printability to investigate the effects of different metal catalysts on its conversion into conductive pyrolytic carbon structures. Then, we switched to using Elegoo as a carbon precursor since it has a higher char yield (8~9 wt%) than PR48 (4~5 wt%).

Table 1.3. Composition and characteristics of the commercial 3D printing resins that have been used to generate pyrolytic carbon by pyrolysis. [63]

Commercial resin	chemicals	AM methods	Ref
PR48	Acrylate-based: Allnex Ebecryl 8210 (39.8 wt %), Genomer 1122 (19.9 wt %), Sartomer SR 494 (39.8 wt %), 2,4,6-Trimethylbenzoyldiphenylphosphineoxide (TPO, 0.4 wt %), Mayzo OB+ UV blocker (0.16 wt %), and undisclosed aliphatic urethane acrylate	DLP, CLIP, PμSL	[63,69,73–75]
Elegoo	Acrylate-based: trimethyl cyclohexyl acrylate (53%), Isopropylidenediphenol (26%), (5-ethyl-1,3-dioxan-5-yl) methyl acrylate (14%), Ethyl phenyl (2,4,6- trimethylbenzoyl) phosphinate (5%), titanium dioxide (1.5%), carbon black (0.5%)	DLP	[22, 71, 76]
Kayaku Advanced Materials SU-8	Epoxy-based: epoxy novolac resin with average epoxide group functionality of 8 (no wt % provided)	SLA	[70, 78, 79]
PIC100 (EnvisionTEC)	Acrylate-based: Methacrylated oligomer (50−90%), methacrylated monomer (5−40%), phosphine oxide photoinitiator (1−2%)	SLA	[77]
Boston MicroFabrication HTL yellow resin	Acrylate-based: Tris[2-(acryloyloxy) ethyl] isocyanurate (5−40%), Acylic Ester (20−80%), 4-(1-oxo-2-propenyl)- Morpholine (10−30%)	SLA	[80]
IP-S (Nanoscribe GmbH)	Acrylate-based: methacrylate carbamate mixture (>95%), butyrolactone (<5%), aromatic ketone photoinitiator (<1%)	DLW-2PP	[81]
VisiJet FTX Green	Acrylate-based: Triethylene glycol diacrylate (40−55%), Tricyclodecane dimethanol diacrylate (15−25%), TPO (1.5−2.5%)	SLA	[82]

References

[1] G. Wang, L. Zhang, J. Zhang, A review of electrode materials for electrochemical supercapacitors, Chem. Soc. Rev. 41 (2012) 797–828. https://doi.org/10.1039/C1CS15060J.

[2] L. Liu, X. Zhang, Y. Liu, X. Gong, Electrochemical Energy Storage Devices─Batteries, Supercapacitors, and Battery–Supercapacitor Hybrid Devices, ACS Appl. Electron. Mater. 7 (2025) 2233–2270. https://doi.org/10.1021/acsaelm.5c00069.

[3] C. Kim, B.Y. Ahn, S. Cho, J. Jung, I. Kim, 3D Printing for Energy Storage Devices: Advances, Challenges, and Future Directions, Advanced Materials 37 (2025) e05943. https://doi.org/10.1002/adma.202505943.

[4] H. Sun, J. Zhu, D. Baumann, L. Peng, Y. Xu, I. Shakir, Y. Huang, X. Duan, Hierarchical 3D electrodes for electrochemical energy storage, Nat Rev Mater 4 (2018) 45–60. https://doi.org/10.1038/s41578-018-0069-9.

[5] F. Béguin, V. Presser, A. Balducci, E. Frackowiak, Carbons and Electrolytes for Advanced Supercapacitors, Advanced Materials 26 (2014) 2219–2251. https://doi.org/10.1002/adma.201304137.

[6] V. Augustyn, P. Simon, B. Dunn, Pseudocapacitive oxide materials for high-rate electrochemical energy storage, Energy Environ. Sci. 7 (2014) 1597–1614. https://doi.org/10.1039/C3EE44164D.

[7] E. Frackowiak, G. Lota, J. Machnikowski, C. Vix-Guterl, F. Béguin, Optimisation of supercapacitors using carbons with controlled nanotexture and nitrogen content, Electrochimica Acta 51 (2006) 2209–2214. https://doi.org/10.1016/j.electacta.2005.04.080.

[8] D. Hulicova, J. Yamashita, Y. Soneda, H. Hatori, M. Kodama, Supercapacitors Prepared from Melamine-Based Carbon, Chem. Mater. 17 (2005) 1241–1247. https://doi.org/10.1021/cm049337g.

[9] G. Lota, K. Lota, E. Frackowiak, Nanotubes based composites rich in nitrogen for supercapacitor application, Electrochemistry Communications 9 (2007) 1828–1832. https://doi.org/10.1016/j.elecom.2007.04.015.

[10] H.M. Jeong, J.W. Lee, W.H. Shin, Y.J. Choi, H.J. Shin, J.K. Kang, J.W. Choi, Nitrogen-Doped Graphene for High-Performance Ultracapacitors and the Importance of Nitrogen-Doped Sites at Basal Planes, Nano Lett. 11 (2011) 2472–2477. https://doi.org/10.1021/nl2009058.

[11] Nitrogen-Enriched Nonporous Carbon Electrodes with Extraordinary Supercapacitance, (n.d.). https://doi.org/10.1002/adfm.200801100.

[12] E. Herrero, L.J. Buller, H.D. Abruña, Underpotential Deposition at Single Crystal Surfaces of Au, Pt, Ag and Other Materials, Chem. Rev. 101 (2001) 1897–1930. https://doi.org/10.1021/cr9600363.

[13] R. Chen, M. Yu, R.P. Sahu, I.K. Puri, I. Zhitomirsky, The Development of Pseudocapacitor Electrodes and Devices with High Active Mass Loading, Advanced Energy Materials 10 (2020) 1903848. https://doi.org/10.1002/aenm.201903848.

[14] J.P. Zheng, P.J. Cygan, T.R. Jow, Hydrous Ruthenium Oxide as an Electrode Material for Electrochemical Capacitors, J. Electrochem. Soc. 142 (1995) 2699. https://doi.org/10.1149/1.2050077.

[15] C.-C. Hu, K.-H. Chang, M.-C. Lin, Y.-T. Wu, Design and Tailoring of the Nanotubular Arrayed Architecture of Hydrous RuO2 for Next Generation Supercapacitors, Nano Lett. 6 (2006) 2690–2695. https://doi.org/10.1021/nl061576a.

[16] J. Liu, J. Bao, X. Zhang, Y. Gao, Y. Zhang, L. Liu, Z. Cao, MnO2 -based materials for supercapacitor electrodes: challenges, strategies and prospects, RSC Adv. 12 (2022) 35556–35578. https://doi.org/10.1039/D2RA06664E.

[17] Z. Sun, Y. Zhang, Y. Liu, J. Fu, S. Cheng, P. Cui, E. Xie, New insight on the mechanism of electrochemical cycling effects in MnO2-based aqueous supercapacitor, Journal of Power Sources 436 (2019) 226795. https://doi.org/10.1016/j.jpowsour.2019.226795.

[18] B. Yao, S. Chandrasekaran, J. Zhang, W. Xiao, F. Qian, C. Zhu, E.B. Duoss, C.M. Spadaccini, M.A. Worsley, Y. Li, Efficient 3D Printed Pseudocapacitive Electrodes with Ultrahigh MnO2 Loading, Joule 3 (2019) 459–470. https://doi.org/10.1016/j.joule.2018.09.020.

[19] S. Zhu, W. Huo, X. Liu, Y. Zhang, Birnessite based nanostructures for supercapacitors: challenges, strategies and prospects, Nanoscale Adv. 2 (2020) 37–54. https://doi.org/10.1039/C9NA00547A.

[20] L.L. Zhang, X.S. Zhao, Carbon-based materials as supercapacitor electrodes, Chem. Soc. Rev. 38 (2009) 2520–2531. https://doi.org/10.1039/B813846J.

[21] S. Chandrasekaran, B. Yao, T. Liu, W. Xiao, Y. Song, F. Qian, C. Zhu, E. B. Duoss, C. M. Spadaccini, Y. Li, M. A. Worsley, Direct ink writing of organic and carbon aerogels, Materials Horizons 5 (2018) 1166–1175. https://doi.org/10.1039/C8MH00603B.

[22] Y. Katsuyama, N. Haba, H. Kobayashi, K. Iwase, A. Kudo, I. Honma, R.B. Kaner, Macro- and Nano-Porous 3D-Hierarchical Carbon Lattices for Extraordinarily High Capacitance Supercapacitors, Advanced Functional Materials 32 (2022) 2201544. https://doi.org/10.1002/adfm.202201544.

[23] B. Yan, L. Feng, J. Zheng, Q. Zhang, S. Jiang, C. Zhang, Y. Ding, J. Han, W. Chen, S. He, High performance supercapacitors based on wood-derived thick carbon electrodes synthesized via green activation process, Inorg. Chem. Front. 9 (2022) 6108–6123. https://doi.org/10.1039/D2QI01914K.

[24] B. Yan, J. Zheng, L. Feng, C. Du, S. Jian, W. Yang, Y.A. Wu, S. Jiang, S. He, W. Chen, Wood-derived biochar as thick electrodes for high-rate performance supercapacitors, Biochar 4 (2022) 50. https://doi.org/10.1007/s42773-022-00176-9.

[25] K. Kierzek, E. Frackowiak, G. Lota, G. Gryglewicz, J. Machnikowski, Electrochemical capacitors based on highly porous carbons prepared by KOH activation, Electrochimica Acta 49 (2004) 515–523. https://doi.org/10.1016/j.electacta.2003.08.026.

[26] E. Raymundo-Piñero, F. Leroux, F. Béguin, A High-Performance Carbon for Supercapacitors Obtained by Carbonization of a Seaweed Biopolymer, Advanced Materials 18 (2006) 1877–1882. https://doi.org/10.1002/adma.200501905.

[27] Z. Yang, J. Tian, Z. Yin, C. Cui, W. Qian, F. Wei, Carbon nanotube- and graphene-based nanomaterials and applications in high-voltage supercapacitor: A review, Carbon 141 (2019) 467–480. https://doi.org/10.1016/j.carbon.2018.10.010.

[28] Y. Han, H. Ha, C. Choi, H. Yoon, P. Matteini, J.Y. Cheong, B. Hwang, Review of Flexible Supercapacitors Using Carbon Nanotube-Based Electrodes, Applied Sciences 13 (2023) 3290. https://doi.org/10.3390/app13053290.

[29] P. Forouzandeh, V. Kumaravel, S.C. Pillai, [Review] Electrode Materials for Supercapacitors: A Review of Recent Advances, Catalysts 10 (2020) 969. https://doi.org/10.3390/catal10090969.

[30] S. Jiang, P.-X. Hou, M.-L. Chen, B.-W. Wang, D.-M. Sun, D.-M. Tang, Q. Jin, Q.-X. Guo, D.-D. Zhang, J.-H. Du, K.-P. Tai, J. Tan, E.I. Kauppinen, C. Liu, H.-M. Cheng, Ultrahigh-performance transparent conductive films of carbon-welded isolated single-wall carbon nanotubes, Sci. Adv. 4 (2018) eaap9264. https://doi.org/10.1126/sciadv.aap9264.

[31] L.F. Aval, M. Ghoranneviss, G.B. Pour, High-performance supercapacitors based on the carbon nanotubes, graphene and graphite nanoparticles electrodes, Heliyon 4 (2018). https://doi.org/10.1016/j.heliyon.2018.e00862.

[32] C. Cao, Y. Zhou, S. Ubnoske, J. Zang, Y. Cao, P. Henry, C.B. Parker, J.T. Glass, Highly Stretchable Supercapacitors via Crumpled Vertically Aligned Carbon Nanotube Forests, Advanced Energy Materials 9 (2019) 1900618. https://doi.org/10.1002/aenm.201900618.

[33] Q. Cheng, J. Tang, J. Ma, H. Zhang, N. Shinya, L.-C. Qin, Graphene and carbon nanotube composite electrodes for supercapacitors with ultra-high energy density, Phys. Chem. Chem. Phys. 13 (2011) 17615. https://doi.org/10.1039/c1cp21910c.

[34] P. Wu, S. Cheng, L. Yang, Z. Lin, X. Gui, X. Ou, J. Zhou, M. Yao, M. Wang, Y. Zhu, M. Liu, Synthesis and Characterization of Self-Standing and Highly Flexible δ-MnO2@CNTs/CNTs Composite Films for Direct Use of Supercapacitor Electrodes, ACS Appl. Mater. Interfaces 8 (2016) 23721–23728. https://doi.org/10.1021/acsami.6b07161.

[35] Y. Wang, Z. Ma, Y. Chen, M. Zou, M. Yousaf, Y. Yang, L. Yang, A. Cao, R.P.S. Han, Controlled Synthesis of Core–Shell Carbon@MoS2 Nanotube Sponges as High-Performance Battery Electrodes, Advanced Materials 28 (2016) 10175–10181. https://doi.org/10.1002/adma.201603812.

[36] Y. Chen, Y. Wang, Z. Wang, M. Zou, H. Zhang, W. Zhao, M. Yousaf, L. Yang, A. Cao, R.P.S. Han, Densification by Compaction as an Effective Low-Cost Method to Attain a High Areal Lithium Storage Capacity in a CNT@Co3O4 Sponge, Advanced Energy Materials 8 (2018) 1702981. https://doi.org/10.1002/aenm.201702981.

[37] C. Zhu, T. Liu, F. Qian, W. Chen, S. Chandrasekaran, B. Yao, Y. Song, E.B. Duoss, J.D. Kuntz, C.M. Spadaccini, M.A. Worsley, Y. Li, 3D printed functional nanomaterials for electrochemical energy storage, Nano Today 15 (2017) 107–120. https://doi.org/10.1016/j.nantod.2017.06.007.

[38] T. Pangarkar, 3D Printing Statistics and Facts (2026), Market.Us Scoop (2026). https://scoop.market.us/3d-printing-statistics/ (accessed June 8, 2026).

[39] S. Tagliaferri, A. Panagiotopoulos, C. Mattevi, Direct ink writing of energy materials, Mater. Adv. 2 (2021) 540–563. https://doi.org/10.1039/d0ma00753f.

[40] M. a. S.R. Saadi, A. Maguire, N.T. Pottackal, M.S.H. Thakur, M.Md. Ikram, A.J. Hart, P.M. Ajayan, M.M. Rahman, Direct Ink Writing: A 3D Printing Technology for Diverse Materials, Advanced Materials 34 (2022) 2108855. https://doi.org/10.1002/adma.202108855.

[41] F. Ning, W. Cong, J. Qiu, J. Wei, S. Wang, Additive manufacturing of carbon fiber reinforced thermoplastic composites using fused deposition modeling, Composites Part B: Engineering 80 (2015) 369–378. https://doi.org/10.1016/j.compositesb.2015.06.013.

[42] R.B. Kristiawan, F. Imaduddin, D. Ariawan, Ubaidillah, Z. Arifin, A review on the fused deposition modeling (FDM) 3D printing: Filament processing, materials, and printing parameters, Open Engineering 11 (2021) 639–649. https://doi.org/10.1515/eng-2021-0063.

[43] Y.I. Mesbah, R.A. Hassan, N.K. Allam, A Review on Three-Dimensional Printing for Energy

Conversion and Storage: Recent Advances and Future Prospects, Energy Fuels 39 (2025) 20084– 20103. https://doi.org/10.1021/acs.energyfuels.5c03606.

[44] A. Asghar, K. Khan, M.S. Rashid, M. Hamza, Z. Liu, C. Liu, Z. Chen, Extrusion-Based Additive Manufacturing of Carbonaceous and Non-Carbonaceous Electrode Materials for Electrochemical Energy Storage Devices, Advanced Materials Technologies n/a (n.d.) 2400136. https://doi.org/10.1002/admt.202400136.

[45] Z. Rymansaib, P. Iravani, E. Emslie, M. Medvidović-Kosanović, M. Sak-Bosnar, R. Verdejo, F. Marken, All-Polystyrene 3D-Printed Electrochemical Device with Embedded Carbon Nanofiber- Graphite-Polystyrene Composite Conductor, Electroanalysis 28 (2016) 1517–1523. https://doi.org/10.1002/elan.201600017.

[46] O.S. Carneiro, A.F. Silva, R. Gomes, Fused deposition modeling with polypropylene, Materials & Design 83 (2015) 768–776. https://doi.org/10.1016/j.matdes.2015.06.053.
[47] S.-H. Ahn, M. Montero, D. Odell, S. Roundy, A. Et., Anisotropic material properties of fused deposition modeling ABS, Rapid Prototyping Journal (2002). https://doi.org/10.1108/13552540210441166.

[48] C.W. Foster, M.P. Down, Y. Zhang, X. Ji, S.J. Rowley-Neale, G.C. Smith, P.J. Kelly, C.E. Banks, 3D Printed Graphene Based Energy Storage Devices, Sci Rep 7 (2017) 42233. https://doi.org/10.1038/srep42233.

[49] S. Kumar, Selective laser sintering: A qualitative and objective approach, JOM 55 (2003) 43–47. https://doi.org/10.1007/s11837-003-0175-y.

[50] R. Chaudhary, P. Fabbri, E. Leoni, F. Mazzanti, R. Akbari, C. Antonini, Additive manufacturing by digital light processing: a review, Prog Addit Manuf 8 (2023) 331–351. https://doi.org/10.1007/s40964-022-00336-0.

[51] J. Nam, M. Kim, Advances in materials and technologies for digital light processing 3D printing, Nano Convergence 11 (2024) 45. https://doi.org/10.1186/s40580-024-00452-3.

[52] M.M. Emami, F. Barazandeh, F. Yaghmaie, Scanning-projection based stereolithography: Method and structure, Sensors and Actuators A: Physical 218 (2014) 116–124. https://doi.org/10.1016/j.sna.2014.08.002.

[53] J. Huang, Q. Qin, J. Wang, A Review of Stereolithography: Processes and Systems, Processes 8 (2020) 1138. https://doi.org/10.3390/pr8091138.

[54] X. Zhou, Y. Hou, J. Lin, A review on the processing accuracy of two-photon polymerization, AIP Advances 5 (2015) 030701. https://doi.org/10.1063/1.4916886.

[55] A. Mao, H. Mitsuboshi, M. Trochon, X. Zhang, L. Trinh, S. Keynia, P. Fan, N. Kraiem, X. Huang, N. Li, P. Li, Z. Wu, W. Sun, B. Cui, J.-F. Silvain, M. Hara, M. Yoshimura, K.L. Marshall, M. Anthamatten, Y. Lu, Evolution of chemical and mechanical properties in two-photon polymerized materials during pyrolysis, Carbon 208 (2023) 384–389. https://doi.org/10.1016/j.carbon.2023.03.061.

[56] Q. Ge, Z. Li, Z. Wang, K. Kowsari, W. Zhang, X. He, J. Zhou, N.X. Fang, Projection micro stereolithography based 3D printing and its applications, Int. J. Extrem. Manuf. 2 (2020) 022004. https://doi.org/10.1088/2631-7990/ab8d9a.

[57] C. Sun, N. Fang, D.M. Wu, X. Zhang, Projection micro-stereolithography using digital micro-mirror dynamic mask, Sensors and Actuators A: Physical 121 (2005) 113–120. https://doi.org/10.1016/j.sna.2004.12.011.

[58] J.R. Tumbleston, D. Shirvanyants, N. Ermoshkin, R. Janusziewicz, A.R. Johnson, D. Kelly, K. Chen, R. Pinschmidt, J.P. Rolland, A. Ermoshkin, E.T. Samulski, J.M. DeSimone, Continuous liquid interface production of 3D objects, Science 347 (2015) 1349–1352. https://doi.org/10.1126/science.aaa2397.

[59] G. Lipkowitz, T. Samuelsen, K. Hsiao, B. Lee, M.T. Dulay, I. Coates, H. Lin, W. Pan, G. Toth, L. Tate, E.S.G. Shaqfeh, J.M. DeSimone, Injection continuous liquid interface production of 3D objects, Science Advances 8 (2022) eabq3917. https://doi.org/10.1126/sciadv.abq3917.

[60] S. O'Halloran, A. Pandit, A. Heise, A. Kellett, Two-Photon Polymerization: Fundamentals, Materials, and Chemical Modification Strategies, Adv Sci (Weinh) 10 (2022) 2204072. https://doi.org/10.1002/advs.202204072.

[61] Microscale 3D Printing: A Review, (2022). https://www.cademix.org/microscale-3d-printing-a-review/ (accessed July 1, 2026).

[62] G. Lipkowitz, T. Samuelsen, K. Hsiao, B. Lee, M.T. Dulay, I. Coates, H. Lin, W. Pan, G. Toth, L. Tate, E.S.G. Shaqfeh, J.M. DeSimone, Injection continuous liquid interface production of 3D objects, Science Advances 8 (2022) eabq3917. https://doi.org/10.1126/sciadv.abq3917.

[63] P.R. Onffroy, S. Chiovoloni, H.L. Kuo, M.A. Saccone, J.Q. Lu, J.M. DeSimone, Opportunities at the Intersection of 3D Printed Polymers and Pyrolysis for the Microfabrication of Carbon-Based Energy Materials, JACS Au 4 (2024) 3706–3726. https://doi.org/10.1021/jacsau.4c00555.

[64] N.R. Catarineu, D. Lin, C. Zhu, D.I. Oyarzun, Y. Li, High-performance aqueous zinc-ion hybrid capacitors based on 3D printed metal-organic framework cathodes, Chemical Engineering Journal 465 (2023) 142544. https://doi.org/10.1016/j.cej.2023.142544.

[65] Y. Shao, C. Guizani, P. Grosseau, D. Chaussy, D. Beneventi, Use of lignocellulosic materials and 3D printing for the development of structured monolithic carbon materials, Composites Part B: Engineering 149 (2018) 206–215. https://doi.org/10.1016/j.compositesb.2018.05.035.

[66] M. Usselmann, J. Bansmann, A.J.C. Kuehne, Switchable Polyacrylonitrile-Copolymer for Melt-Processing and Thermal Carbonization—3D Printing of Carbon Supercapacitor Electrodes with High Capacitance, Advanced Materials 35 (2023) 2208484. https://doi.org/10.1002/adma.202208484.

[67] A. Kudo, K. Kanamaru, J. Han, R. Tang, K. Kisu, T. Yoshii, S. Orimo, H. Nishihara, M. Chen, Stereolithography 3D Printed Carbon Microlattices with Hierarchical Porosity for Structural and Functional Applications, Small 19 (2023) 2301525. https://doi.org/10.1002/smll.202301525.

[68] Y. Katsuyama, A. Kudo, H. Kobayashi, J. Han, M. Chen, I. Honma, R.B. Kaner, A 3D-Printed, Freestanding Carbon Lattice for Sodium Ion Batteries, Small 18 (2022) 2202277. https://doi.org/10.1002/smll.202202277.

[69] K. Narita, M.A. Citrin, H. Yang, X. Xia, J.R. Greer, 3D Architected Carbon Electrodes for Energy Storage, Advanced Energy Materials 11 (2021) 2002637. https://doi.org/10.1002/aenm.202002637.

[70] J.Y. Pan, B. Rezaei, T.A. Anhøj, N.B. Larsen, S.S. Keller, Hybrid microfabrication of 3D pyrolytic carbon electrodes by photolithography and additive manufacturing, Micro and Nano Engineering 15 (2022) 100124. https://doi.org/10.1016/j.mne.2022.100124.

[71] Y. Katsuyama, A. Kudo, H. Kobayashi, J. Han, M. Chen, I. Honma, R.B. Kaner, A 3D-Printed, Freestanding Carbon Lattice for Sodium Ion Batteries, Small 18 (2022) 2202277. https://doi.org/10.1002/smll.202202277.

[72] H. Steldinger, A. Esposito, K. Brunnengräber, J. Gläsel, B.J.M. Etzold, Activated Carbon in the Third Dimension—3D Printing of a Tuned Porous Carbon, Advanced Science 6 (2019) 1901340. https://doi.org/10.1002/advs.201901340.

[73] A. Kudo, F. Bosi, Nanographitic coating enables hydrophobicity in lightweight and strong microarchitected carbon, Commun Mater 1 (2020) 72. https://doi.org/10.1038/s43246-020-00073-3.

[74] M.D. Reale Batista, S. Chandrasekaran, B.D. Moran, M. Salazar De Troya, A. Pinongcos, Z. Wang, R. Hensleigh, A. Carleton, M. Zeng, T. Roy, D. Lin, X. Xue, V.A. Beck, D.A. Tortorelli, M. Stadermann, R. Zheng, Y. Li, M.A. Worsley, Design and additive manufacturing of optimized electrodes for energy storage applications, Carbon 205 (2023) 262–269. https://doi.org/10.1016/j.carbon.2023.01.044.

[75] H.-L. Kuo, P.R. Onffroy, S.P. Chiovoloni, L. Williams, J.M. DeSimone, J. Lu, Engineered 3D micro-architected carbon structures via conformal deposition of multifunctional transition metal catalysts, Carbon 247 (2026) 121043. https://doi.org/10.1016/j.carbon.2025.121043.

[76] A. Kudo, K. Kanamaru, J. Han, R. Tang, K. Kisu, T. Yoshii, S. Orimo, H. Nishihara, M. Chen, Stereolithography 3D Printed Carbon Microlattices with Hierarchical Porosity for Structural and Functional Applications, Small 19 (2023) 2301525. https://doi.org/10.1002/smll.202301525.

[77] H. Korhonen, L.H. Sinh, N.D. Luong, P. Lehtinen, T. Verho, J. Partanen, J. Seppälä, Fabrication of graphene-based 3D structures by stereolithography, Physica Status Solidi (a) 213 (2016) 982–985. https://doi.org/10.1002/pssa.201532761.

[78] S. Hemanth, C. Caviglia, S.S. Keller, Suspended 3D pyrolytic carbon microelectrodes for electrochemistry, Carbon 121 (2017) 226–234. https://doi.org/10.1016/j.carbon.2017.05.090.

[79] R. Natu, M. Islam, R. Martinez-Duarte, Shrinkage Analysis of Carbon Micro Structures Derived from SU-8 Photoresist, ECS Trans. 72 (2016) 27. https://doi.org/10.1149/07201.0027ecst.

[80] M. Taale, B. Schamberger, M.A. Monclus, C. Dolle, F. Taheri, D. Mager, Y.M. Eggeler, J.G. Korvink, J.M. Molina-Aldareguia, C. Selhuber-Unkel, A.D. Lantada, M. Islam, Microarchitected Compliant Scaffolds of Pyrolytic Carbon for 3D Muscle Cell Growth, Advanced Healthcare Materials 13 (2024) 2303485. https://doi.org/10.1002/adhm.202303485.

[81] C. Yang, Q. Cao, P. Puthongkham, S.T. Lee, M. Ganesana, N.V. Lavrik, B.J. Venton, 3D-Printed Carbon Electrodes for Neurotransmitter Detection, Angewandte Chemie International Edition 57 (2018) 14255–14259. https://doi.org/10.1002/anie.201809992.

[82] P. Tian, C. Chen, J. Hu, J. Qi, Q. Wang, J.C.-M. Chen, J. Cavanaugh, Y. Peng, M.M.-C. Cheng, A novel fabrication method of carbon electrodes using 3D printing and chemical modification process, Biomed Microdevices 20 (2018) 4. https://doi.org/10.1007/s10544-017-0247-3.

Chapter 2 - Design of 3D Carbon Electrodes via Metal-Catalyzed Conversion of 3D-Printed Polymer PR48 Templates

Three-dimensional (3D) carbon architecture has attracted significant attention for energy storage and conversion applications. Although conventional porous carbons offer high surface areas, their poorly defined pore structures often contain inaccessible or closed pores, limiting the effective electrochemical surface area. Converting 3D polymer templates into engineered carbon architecture provides a promising route to achieve well-defined structures with high accessible surface area and low tortuosity, thereby enabling efficient volumetric electrochemical processes. However, direct pyrolysis of polymers typically yields low carbon yields and severe structural shrinkage. [1,2]

Here, I present a strategy to enhance the carbonization yield and the dimensional stability of 3D-printed polymer structures using low-cost transition-metal salts. Through metal–ester coordination, transition-metal ions are conformally deposited onto the polymer framework prior to pyrolysis. During thermal treatment, these metal species serve dual roles by catalyzing polymer-to-carbon conversion and promoting graphitization. Among the tested salts, $FeCl_3$ exhibits pronounced catalytic activity, increasing the carbon yield (defined as the pyrolyzed mass divided by the original polymer mass) from 4.2 wt% for the pristine polymer to 21.4 wt%. In addition to catalytic effects, the Fe-rich coating acts as a structural scaffold that preserves the original geometry during pyrolysis. Dense polymer lattices with initial strut diameters of 50 μm, which typically shrink to approximately 10 μm, retain diameters of 43 μm after carbonization. This approach enables precise control over carbon yield, dimensional retention, graphitization, and porosity, offering a scalable pathway to fabricate highly engineered 3D micro-architected carbons for advanced applications.

2.1. Selection of metal catalyst for graphitization

Transition metals exhibit promising catalytic activity due to their unique electronic structures, with partially filled d and f orbitals that allow easier electron transfer, variable oxidation states, and effective interactions with reactants. The transition metals can lower activation barriers by regulating charge distribution, adsorption energies, and binding to reaction intermediates. [3]

2.1.1. Catalytic graphitization

Catalytic graphitization is a widely accepted process, but the underlying mechanism remains incompletely understood. [4] One of the most proposed pathways of catalytic graphitization is the dissolution-precipitation mechanism. The solid carbon precursors will begin to decompose and transform into disordered amorphous carbon at high temperatures; at the same time, metal precursors are reduced to metal particles, and the disordered carbon around the metal particles dissolves and diffuses into the metal, forming metal carbides.[4] The carbon inside the metal and metal carbides will be precipitated out as graphitic carbon by two different routes:

(i) The metal carbides decompose into graphitic carbon and metal at higher temperatures.

(ii) After a sufficient time at a given temperature, the metal particles reach saturation with carbon. Upon cooling, the carbon-saturated metal becomes supersaturated with respect to disordered carbon.

$$M + C \rightarrow MC \rightarrow M + graphitic\,carbon$$

Therefore, the dissolution-precipitation mechanism is controlled by two factors: (1) the solubility of carbon in metals, and (2) the formation and thermal stability of metal carbides. [4] The first factor of catalytic

graphitization ability of transition metals is carbon solubility. Fe and Ni dissolve significant amounts of carbon at high temperatures, allowing carbon to diffuse into the catalyst and precipitate as graphitic carbon on cooling. At 900 ºC, Fe holds a few tens of wt% carbon (varying by phase, such as ferrite, austenite) (**Figure 2.1**), while the carbon solubility of Ni is around 0.1–0.2 wt% (**Figure 2.2**). In contrast, Cu has minimal carbon solubility and does not form stable carbides (**Figure 2.3**), limiting carbon uptake and inhibiting catalytic graphitization. [4] On the other hand, the formation and stability of metal carbides play a critical role in determining the extent of graphitization.

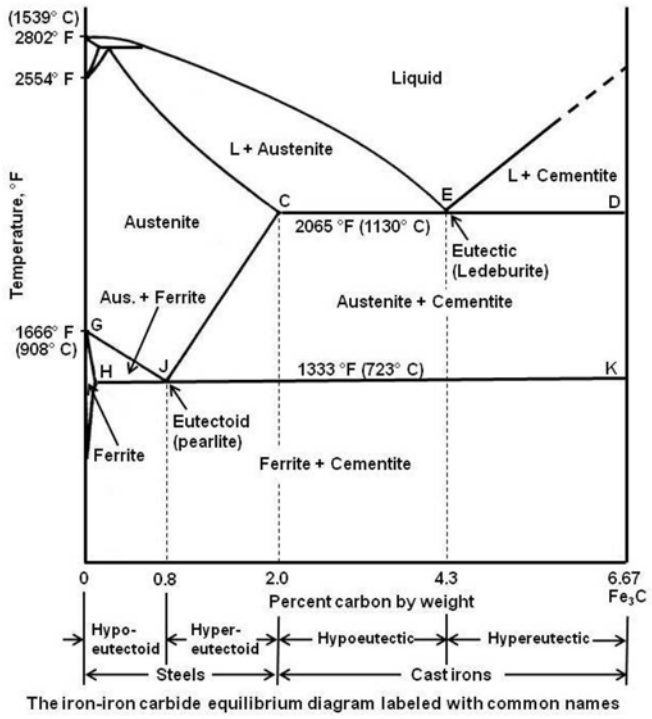


Figure 2.1. Phase diagram of Fe and carbon. [5]

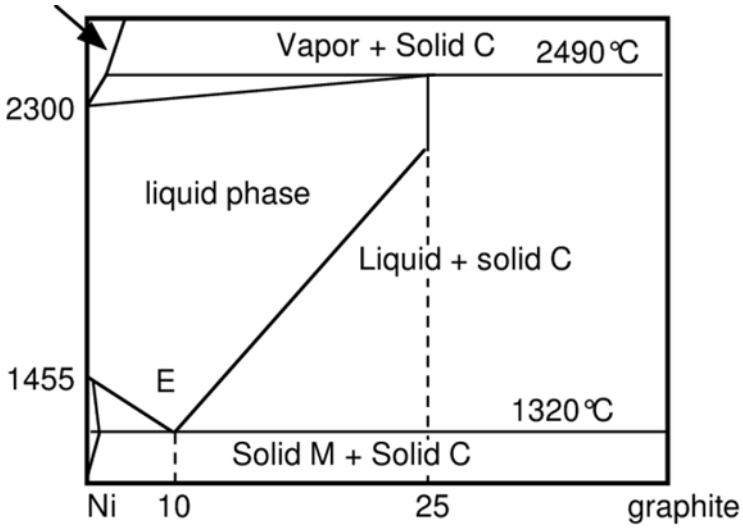


Figure 2.2. Phase diagram of Ni and carbon. [6]

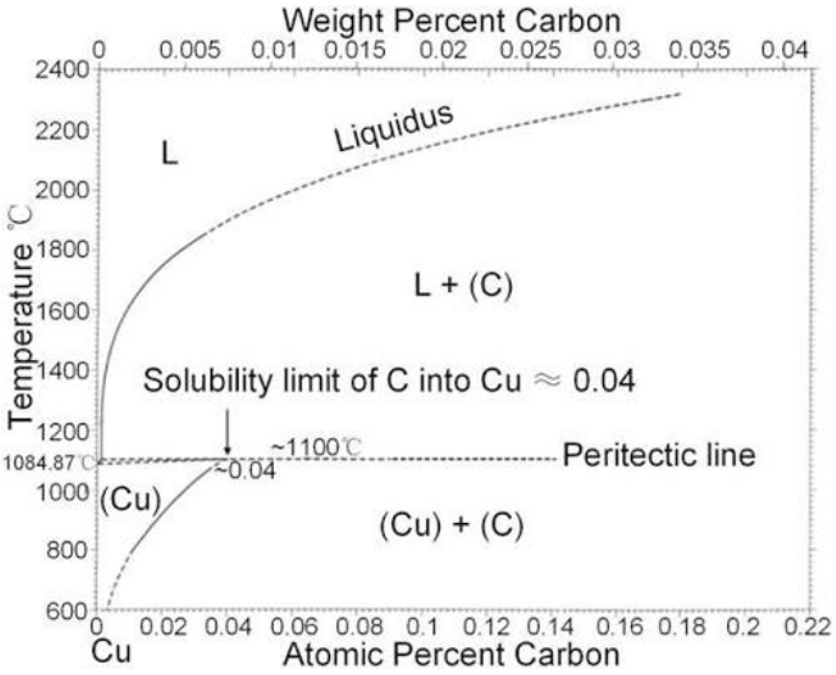


Figure 2.3. Phase diagram of Cu and carbon.[7]

The catalytic activity of transition metals in chemical processes is strongly related to the number of d-shell vacancies in free atoms. [4] The electron configuration of a copper atom is [Ar] $3d^{10}$ $4s^{1}$, so copper has no vacancies in its 3d orbitals. Therefore, the Cu atom has limited reactivity to form covalent bonds with other atoms due to its completely filled d-orbital electrons. On the other hand, the electron configuration of Fe is [Ar] $3d^{6}$ $4s^{2}$, and that of Ni is [Ar] $3d^{8}$ $4s^{2}$; both have incomplete d orbitals. The energy of these electron configurations changes very little when they accept additional electrons from carbon. As a result, these metals can react with carbon to form covalent bonds, thereby promoting carbon dissolution.

2.1.2. Thermal decomposition

Transition-metal catalysts play a critical role in promoting the thermal decomposition of carbon precursors in the early stages of pyrolysis. Much research indicates that transition metals in their oxidized states can interact with organics and macromolecules at lower temperatures during the early stage of pyrolysis, altering their degradation pathways, as evidenced by variations in the observed liquid and gas products. [4,8–11] At the same time, transition metals facilitate the removal of heteroatoms (e.g., O, N, and H) through redox-mediated processes, enhancing aromatization and the formation of conjugated carbon networks. Ji et al. indicate that transition-metal oxides can lower the onset temperature of thermal decomposition and modify the degradation pathways in PVC pyrolysis. [12] Xia et al. investigated the catalytic effect of iron-based salts on the pyrolysis of biomass and found that these salts promote biomass decomposition and lower the onset decomposition temperature [13].

2.1.3. Capture hydrocarbon byproducts from degradation gases

Transition-metal catalysts can also be used to capture hydrocarbon degradation products as additional carbon sources during polymer pyrolysis. The mechanism for capturing hydrocarbon gases involves surface chemical absorption, dissociation, recombination, and desorption at metal active sites [4]. During pyrolysis, the degraded carbon-containing gases trapped by the catalyst shell can transform into graphene sheets, carbon nanotubes, and nanofibers on a metallic surface. [14–16] These gases interact with the metals in a manner similar to chemical vapor deposition. Yao et al. [16] use Fe and Ni catalysts to capture and convert hydrocarbon byproducts released during polypropylene pyrolysis. As shown in **Figure 2.4**, Hydrocarbon byproducts are dissociated and reassembled into multi-walled carbon nanotubes, while the dehydrogenation reaction simultaneously produces a hydrogen-rich gas.

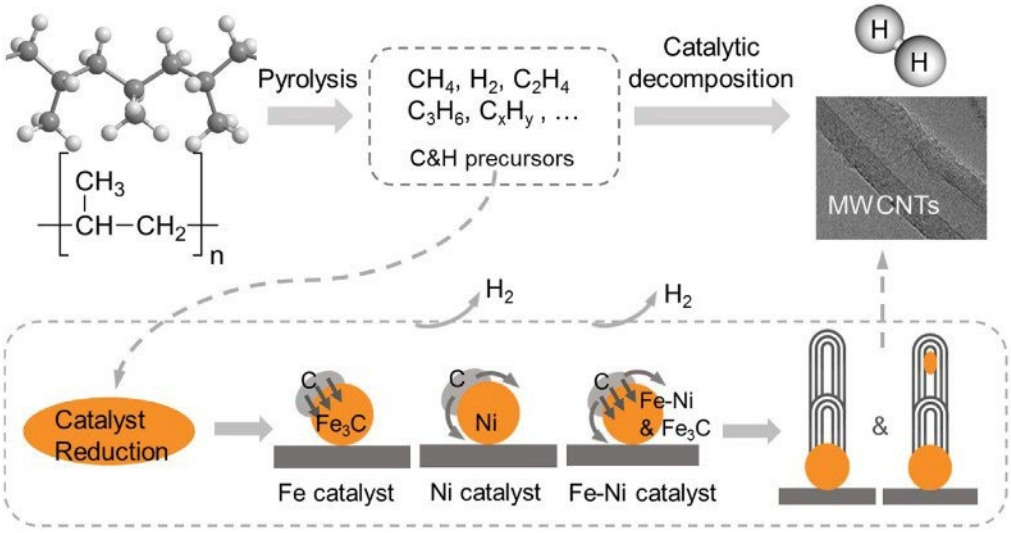


Figure 2.4 Schematic depiction of pyrolysis and catalytic decomposition for hydrogen gas and CNTs growth with Fe/Ni catalysts [16]

2.2. Selection of metal chloride salts

Numerous studies have revealed the impact of counter anions in metal salts on carbonization. [11,17–22] For instance, while $Fe(NO_3)_3$ promotes hydrolysis reactions enhancing polymer degradation [18], $FeCl_3$ improves char yield through the synergistic interaction between Fe^{3+} and Cl^- to enable crosslinking, aromatization, and subsequent graphitization with the formation of carbon nanofibers. [20,22] Researchers have also found that adding $CuCl_2$ to the Ni catalyst system increases char yield considerably. [17] It is believed that the chlorine radicals generated during pyrolysis play a critical role in transforming polymeric materials into carbon structures. [17] Due to their strong electrophilic and hydrogen-abstracting reactivity, chlorine radicals attack C-H bonds, abstracting H atoms and forming HCl as a byproduct, thereby promoting dehydrogenation and cyclization to form carbon precursors [21,23]. Chlorides are known to promote chain scission and increase the amount of olefin bonds. [21,23] Furthermore, chlorides can facilitate cyclization and dehydrogenation reactions, thereby making aromatics the major products. [17–19,22,24,25] Yu et al. proposed a combined catalytic pathway involving halogen-based catalysts in the carbonization of polypropylene during combustion [17]. (Shown as **Figure 2.5**) The halide (X) radicals will be formed when heating halogenated compounds at higher temperatures, and halide radicals can attack the hydrogen atom

attached to the degradation products of polypropylene, forming HX products, accelerating the dehydrogenation process. Due to the strong catalytic effect of halide (X) on the dehydrogenation of degradation products, hydrogen transfer, isomerization, cyclization, and aromatization occur in the combustion, facilitating the formation of aromatic hydrocarbons in the degradation products.

Another study shows that the carbon nanotube yield can be enhanced by tailoring the ratio of Ni^{2+} vs. Cl^- [19]. Moreover, Figure 2.6 shows that chloride-based metal salts also have the highest carbon-to-solid product ratio [13], leading to higher char yield and better structural retention. Based on these findings, I selected metal salts with Cl− counterions. Based on these findings, I selected metal salts with Cl^- counterions as our graphitization catalysts.

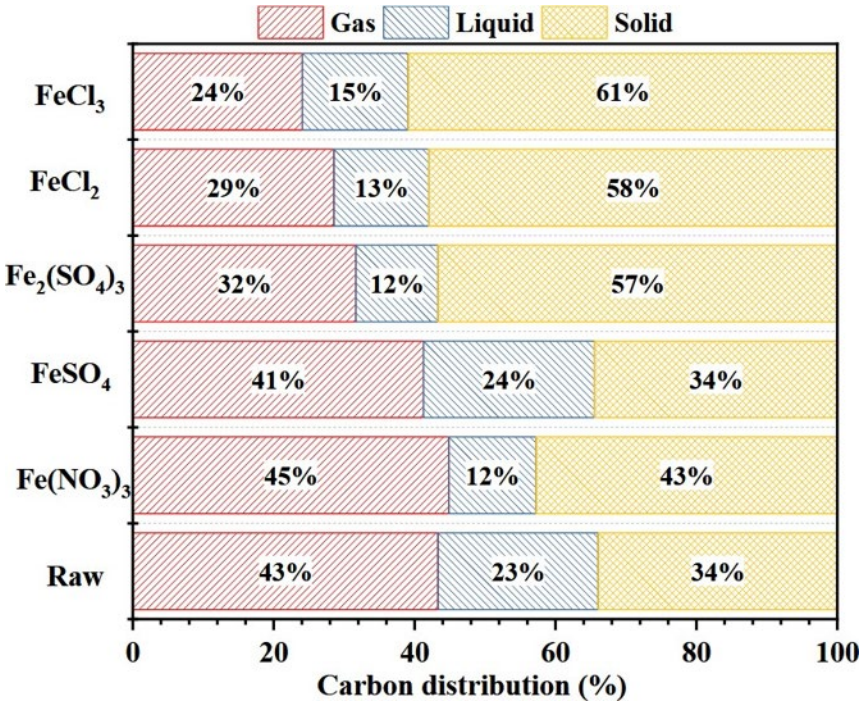


Figure 2.6. Carbon distribution in products after pyrolysis with different Fe salts. [13]

2.3. Experimental section

Two methods were developed in this study for the selective deposition and incorporation of transition metal catalysts onto 3D polymer template surfaces (**Figure 2.7.a**). The first method involved soaking 3D polymer templates in their respective metal salt solutions under ambient conditions, which allowed the metal cations to interact with O–C=O groups on the polymer surfaces and impinge into the polymer lattice to form coordination bonds. (**Figure 2.8**) The second method is to heat a metal salt solution containing a 3D polymer template, then slowly evaporate the solvent, thereby forming a relatively thick, conformal catalyst crust on the template surface.

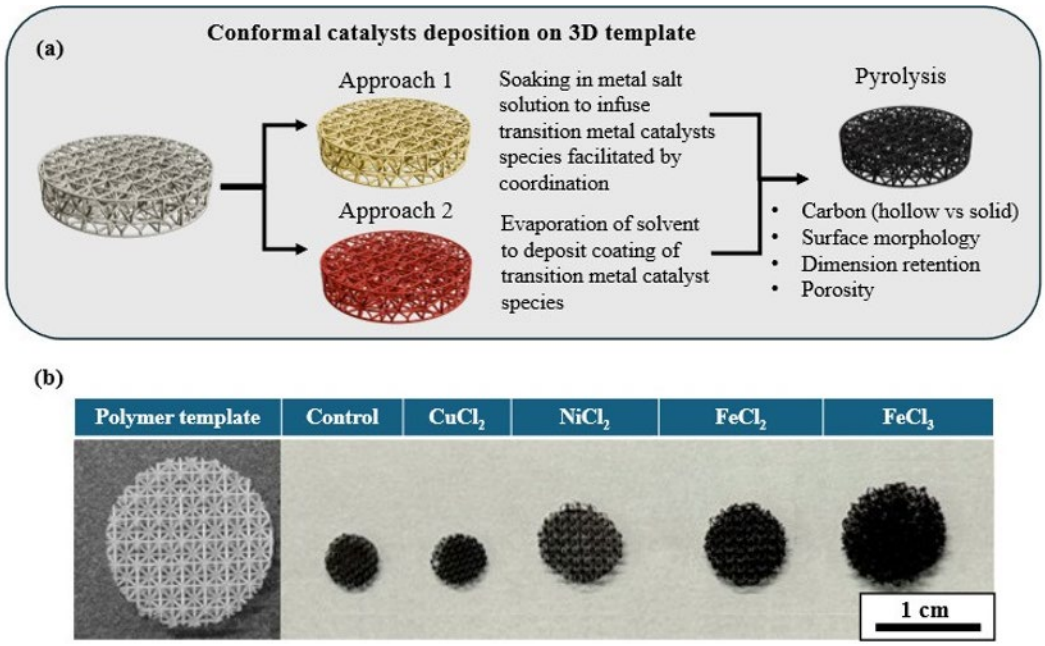


Figure 2.7. (a) Schematic illustration of the process flow for selective metal salt impregnation onto 3D polymer templates via two approaches; (b) Optical images of the polymer template (leftmost) and the resulting 3D carbon after pyrolysis at 900 °C using approach 1, showing areal retention and density. [1]

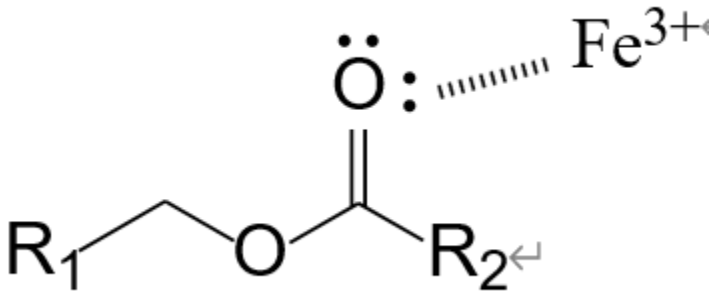


Figure 2.8. Illustration of metal cations interacting with O–C=O groups on the polymer surfaces and infiltrating into the polymer lattice to form coordination bonds

2.3.1. Metal catalyst impregnation process

Approach 1

Low-resolution PR48 polymer templates were cleaned by mild sonication in ethanol for 24 h. After cleaning and drying, templates were soaked in 0.05 M ethanol solutions of each metal salt ($FeCl_3 \cdot 6H_2O$, $FeCl_2 \cdot 4H_2O$, $CuCl_2 \cdot 2H_2O$, or $NiCl_2 \cdot 6H_2O$) for 3 days unless otherwise specified. High-resolution PR48 polymer templates were soaked in solutions for 24 h.

For $FeCl_2$, both templates and the solution were purged with Ar to remove O_2. The soaking was conducted in a glovebox (MBraun Lab master 130) under an Ar atmosphere to prevent oxidation of Fe to Fe^{3+} in solution. All other metal salt treatments were performed under ambient atmospheric conditions. After soaking, samples were spin-dried for 1 min using a commercially available kitchen salad spinner, then placed under vacuum at room temperature for 16 h to remove any remaining solvent.

Approach 2

A modified solvothermal approach is used to encase 3D architected PR48 electrode templates in a graphitization catalyst precursor shell. The as-printed PR48 templates were submerged in a 0.2 M $FeCl_3 \cdot 6H_2O$ ethanol solution in a 25 mL Teflon container and placed in a 50 mL stainless steel autoclave jacket without a complete seal. The samples were heated to 170 °C for 3 h. This enabled the slow evaporation of ethanol from the autoclave jacket. As ethanol evaporates, the concentration of catalysts in the solution increases, leading to saturation and subsequent deposition on the template surface, thereby forming a shell.

2.3.2. Pyrolysis procedure

Based on TGA analysis (See **Section 2.4.3**), the pyrolysis process was conducted in an Atomate three-zone furnace with feedback loop control of temperature, flow rate, and pressure. The temperature first increased from room temperature to 120 °C at 5 °C/min, then ramped more slowly to 300 °C at 1 °C/min. The sample was then held isothermally at 300 °C for 1 h to minimize the volatile mass loss and prevent structural deformation. Subsequently, the temperature increased to 550 °C at 1 °C/min, and further to 900 °C at 2 °C/min. The final temperature of 900 °C was maintained for 2 h to complete the pyrolysis. Continuous argon flow ensured an inert environment.

2.3.3. Material characterization

Optical microscopy (OM; Keyence VHX-X1F) was used for initial sample inspection and to measure strut size and unit cell dimensions of polymer samples, while scanning electron microscopy (SEM; Zeiss Gemini 500) was used to examine sample morphology after pyrolysis, with strut diameters measured from SEM images using ImageJ software. Scanning electron microscopy with energy-dispersive X-ray spectroscopy (SEM-EDS; Thermo Fisher Phenom XL Desktop SEM) was used to analyze elemental distributions in the cross-sections of carbonized samples. Nexus X-ray photoelectron spectrometer (XPS; Thermo Fisher) equipped with an Al Kα (1486.6 eV) source and a 400-μm X-ray source spot size was used to investigate the chemical composition of the catalyst-coated polymer samples. The degree of graphitization was examined by Raman spectroscopy (WiTec Alpha 300 spectrometer) over the wavenumber range of 1000–2000 cm^{-1}.

2.3.4. Strut size calculation

ImageJ software was used to quantitatively analyze the SEM images and measure the unit cell size, strut diameter, and unit cell area of the pyrolytic 3D-printed carbon lattices. First, the ImageJ software was calibrated using the scale bars in the SEM images, and then the relevant features were manually identified for measurement. The strut size was determined by measuring the two thickest and two thinnest regions of each carbon strut and averaging them. For each sample, three individual struts were measured to represent the sample's average strut size. (**Figure 2.9**)

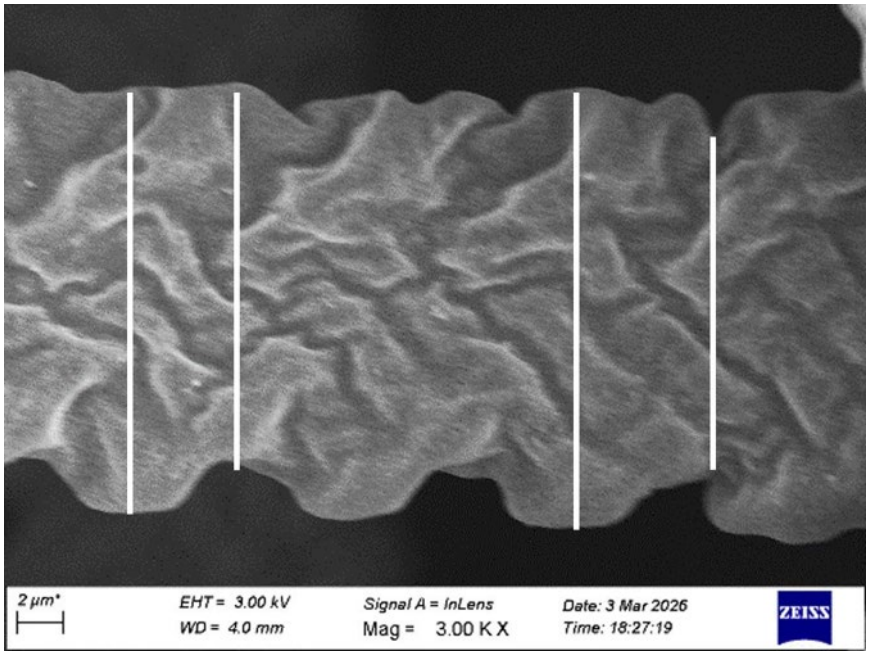


Figure 2.9. Using ImageJ software to measure strut size by the two thickest and two thinnest regions of each carbon strut.

2.4. Results and discussion

2.4.1. Conformal deposition of catalysts on 3D polymer template

Metal complexation facilitates a conformal coating of the catalyst layer on 3D polymers. This conclusion is supported by optical microscopy images of the samples, which show no clogging and a uniform color (**Figure 2.10**). After the formation of the metal-rich shell on a 3D polymer structure, pyrolysis induces chemical and thermal carbonization, transforming the polymer into carbon. **Fig. 2.7.b** shows the size variation of pyrolyzed samples prepared using different metal salts by approach 1, compared with the untreated sample; Ni^{2+}, Fe^{2+}, and Fe^{3+} exhibit greater dimensional retention than the untreated polymer, with Fe^{3+} resulting in the lowest shrinkage. In contrast, the Cu^{2+}-treated sample exhibited overall dimensions similar to the pure polymer. The corresponding estimated carbon and bulk densities indicate that the Cu^{2+}-treated carbon has the highest values, whereas the Ni2+-treated sample displays the lowest (**Table 2.1**). The lower carbon density observed in samples soaked in Fe^{3+}, Ni^{2+}, and Fe^{2+} solutions suggest that the resulting carbon may contain pores and voids.

Table 2.1. shows the effect of catalysts on carbon density and geometric retention.

Sample	Pure polymer	Cu^{2+}	Ni^{2+}	Fe^{2+}	Fe^{3+}
Areal retention (%)	11	10	21	21	36
Bulk density (mg/cm^3)	164	248	62	137	93
Resulting carbon density (g/cm^3)	1.22	1.76	0.46	1.1	0.74

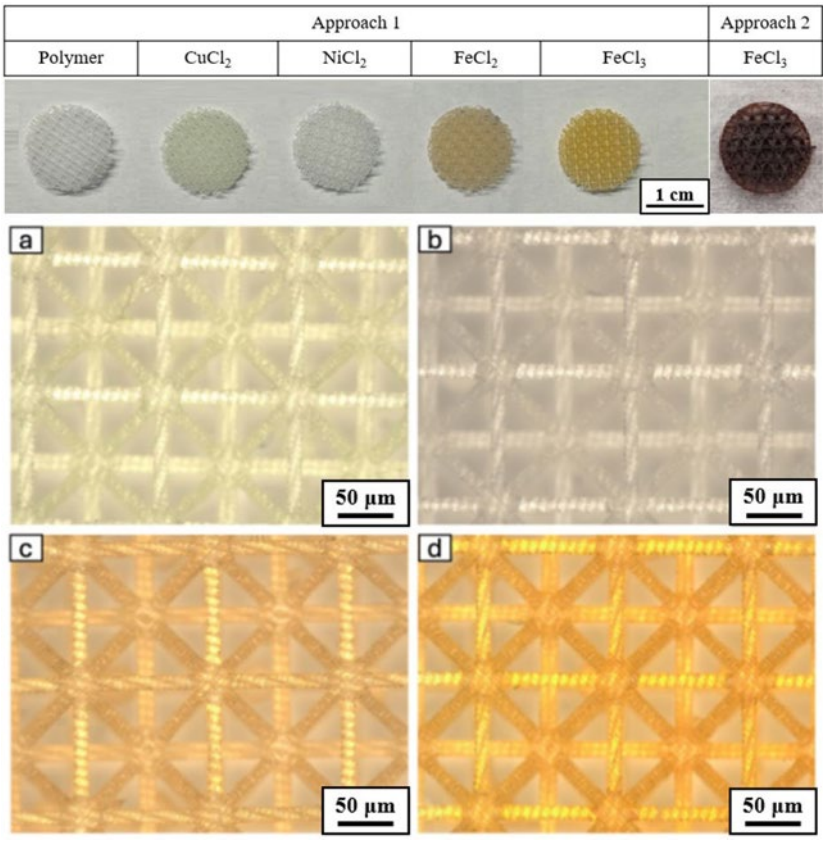


Figure 2.10. Photo images of samples after soaking in 50 mM metal chloride solution in ethanol for 72 hours (Approach 1) and after solvent evaporation for Fe^{3+} catalyst deposition (Approach 2; Bottom: Optical images of catalyst infused samples using approach 1, (a) 50 mM $CuCl_2$, (b) 50 mM $NiCl_2$, (c) 50 mM $FeCl_2$, (d) 50 mM $FeCl_3$ in ethanol solution. (Each condition was tested in triplicate, and all replicates yielded consistent results)

Carbon yield is sensitive to the selected metal catalysts. **Figure 2.11** displays the average carbon yield after pyrolysis at 900 °C for 2 h. Fe^{3+} triples the carbon yield over the untreated polymer control sample. The error bar represents the run-to-run variation based on four runs. The substantial variation in carbon yield generated by Fe^{2+} likely results from different degrees of air exposure, since Fe^{2+} can be easily oxidized into Fe^{3+}. The density of the Ni-treated sample is the lowest, at 62 mg/cm3, suggesting that the carbon derived from the Ni-treated polymer is porous. On the other hand, the copper sample offers a higher density (248 mg/cm^3) than the pure polymer.

The carbon strut morphology of all samples pyrolyzed at 900 °C was also analyzed (**Figure 2.12**). The Ni^{2+}- treated sample, subjected to carbothermal reaction, produced thin, distorted carbon struts. In contrast, the surface pinning effect in Fe^{2+} and Fe^{3+}-treated samples led to significantly enhanced dimensional retention. After pyrolysis at 900 °C, the Fe^{3+}-treated samples had an average strut diameter of 140 µm, a twofold increase over the 70 µm carbon struts from untreated polymer templates (which were 300 µm in diameter before pyrolysis). **Table 2.3** presents the average strut size calculated from three data points. Size retention can be adjusted by the thickness of the metal shell.

The high carbon density observed in Cu-treated samples is due to a combination of their low dimensional retention and higher carbon yield than that of the pure polymer (as shown in Tables **2.1 and 2.2**). Cu is known to chelate CO/CO_2, generating reactive carbon species (C*) that produce hydrocarbons via

electrochemical and thermal pathways [26,27]. It has been reported that a higher yield of aromatic products is observed at 800°C or above in the presence of copper, as the catalytic interaction of copper promotes the coupling of halogenated aromatic rings [28,29]. The lack of copper oxide prevents the carbothermal reaction from producing a porous carbon structure. Therefore, the overall carbon density of Cu-treated samples is substantially higher than that of Fe- and Ni-treated ones, as shown in **Table 2.1**.

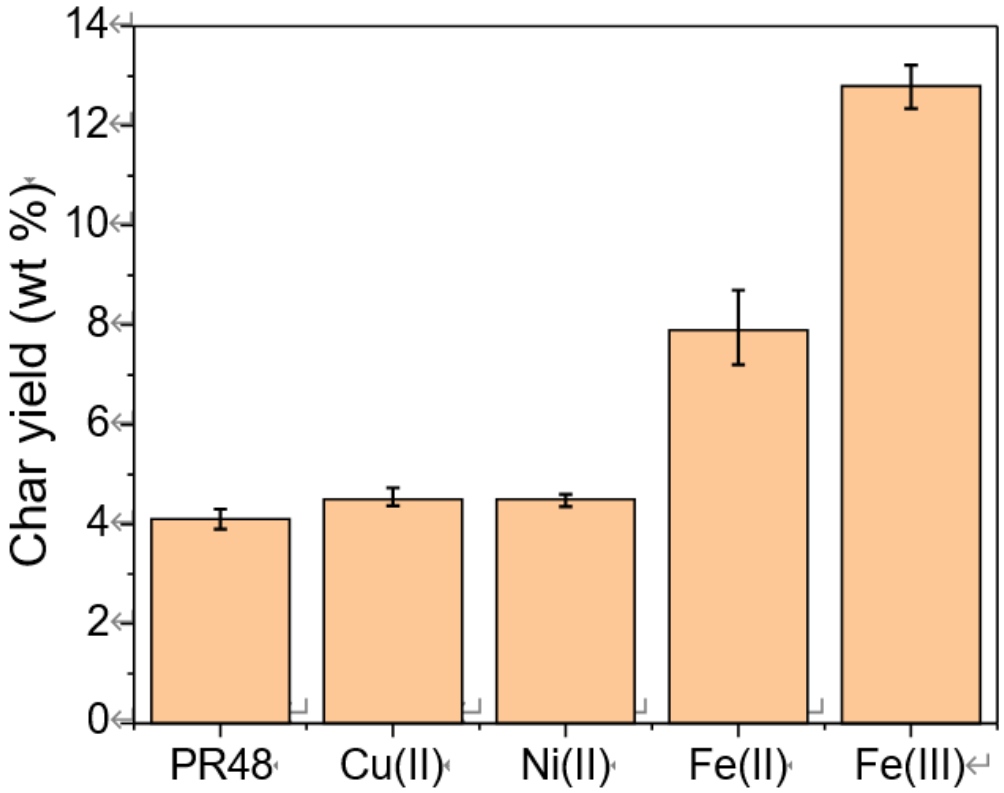


Figure 2.11. Carbon yield and range (based on three runs) of metal-treated PR48 versus neat polymer.

Table 2.2. Carbon yield of PR48 samples soaked in different metal catalysts.

Metal salt	Carbon yield (wt%)
$FeCl_3$	12.8
$FeCl_2$	7.9
Ni Cl_2	4.5
Cu Cl_2	4.5
PR48	4.1

Carbon samples derived from $NiCl_2$-treated samples exhibit similar dimensional retention to those of the $FeCl_2$-treated samples, which are smaller than $FeCl_3$ and significantly larger than those treated with $CuCl_2$ (**Figure 2.3b**). Infusion with Ni^{2+} produces highly porous carbon with the lowest density (62 mg/cm³ after 900 °C pyrolysis) because NiO triggers carbothermal reactions at 700 °C that etch the carbon and generate porosity. In contrast, Fe_2O_3 generated during pyrolysis requires a higher temperature than NiO to initiate carbothermal reactions. Since there is no substantial weight loss (< 3 wt%) between samples pyrolyzed at 800 °C and 900 °C, we conclude that only minimal carbothermal reaction occurred in our Fe samples.

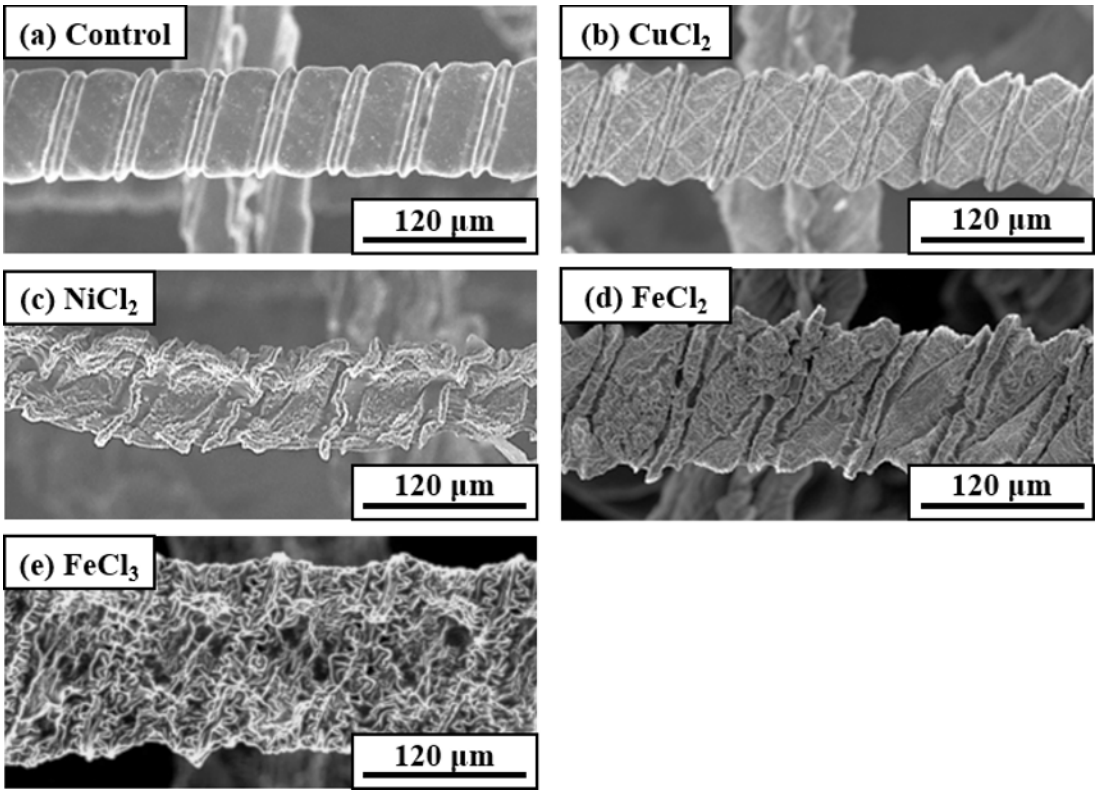


Figure 2.12. SEM images for carbon struts with different treatments: (a) control, (b) Cu^{2+}, (c) Ni^{2+}, (d) Fe^{2+} and (e) Fe^{3+}, prepared from polymer pyrolyzed at 900 °C for 2 h.

Table 2.3. Variation in strut diameter of pyrolyzed PR48 samples soaked in different transition-metal catalysts using approach 1.

Sample	Strut diameter (µm) based on 3 data points (3 different struts in 1 sample)
$FeCl_3$	138
$FeCl_2$	112
Ni Cl_2	71
Cu Cl_2	76
PR48-control	72

2.4.2. Metal catalyst formation of coordination complexes and metal hydroxides/oxides on polymer surface

X-ray photoelectron spectroscopy (XPS) was used to investigate the interaction between 3D polymer templates and metal salts, with an electron flood gun used to minimize surface charging [30]. As shown in **Figure 2.13**, the O(1s) spectra of the metal-soaked samples obtained by approach 1 show a shift of the oxygen peak associated with O-C=O groups on the polymer chains. This peak, initially at 532.5 eV in pure polymer, shifts to a lower binding energy, which is about 800 meV lower for Fe^{2+} and up to 1700 meV lower for Fe^{3+}. The shift in binding energy arises from changes in the electronic environment of oxygen species, resulting from the combined effects of complexation and electrostatic interactions.

Abundant ester groups on polymer surfaces enable the formation of metal acetate-like bonding (M^{+}–CH_3COO^{-}), which exhibits both ionic and coordination bonding characteristics. The negative charge is delocalized over two oxygen atoms, resulting in an electron-rich environment that leads to a redshift in binding energy. The stronger interaction between metal ions and ester groups typically results in greater charge transfer, which in turn leads to larger shifts in binding energy. [31,32] It is known that trivalent cations such as Fe^{3+} form strong coordination bonds with oxygen-containing groups, including hydroxyl, carboxyl, and carbonyl groups. [22,33] This was evidenced by detectable changes in fluorescence resulting from the interaction between carbonyl groups on carbon quantum dots and Fe^{3+} [34]. This could explain why the Fe^{3}-impregnated sample shows a pronounced shift to a lower binding energy compared with divalent cations. The appearance of a new peak centered at 529.4 eV in both Fe^{3+} and Fe^{2+}-treated samples supports the formation of Fe–O lattices in the form of Fe_xO_y and $FeO(OH)_x$ [35,36]. This finding corroborates the understanding that, according to Pourbaix diagrams, Fe salts tend to form stable hydroxides and oxides over a wider pH range compared to Ni and Cu salts. [37,38]

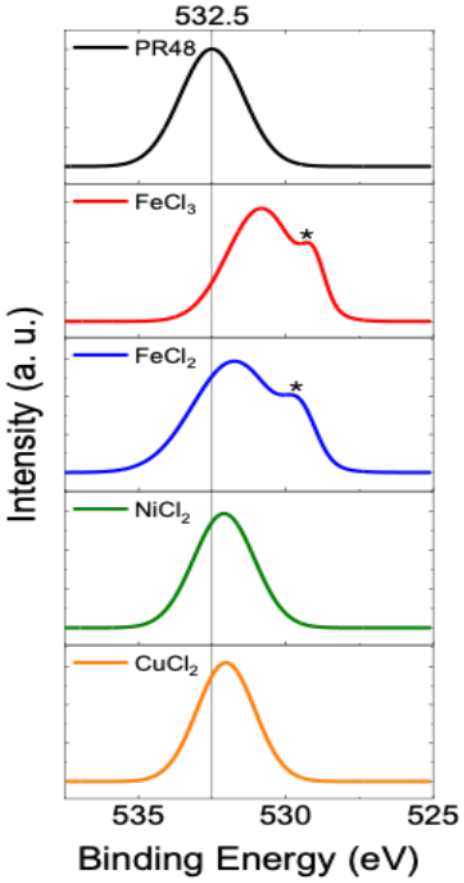


Figure 2.13. XPS O(1s) spectra, displaying the shift of the ester group's binding energy from its undisturbed polymer center upon interaction with transition metal cations. (Peak values of Cu^{2+} are at 532.1 eV, Ni^{2+} are 532.0 eV, Fe^{2+} are 531.7 eV, and Fe^{3+} are 530.8 eV vs 532.5 eV untreated) The peaks are associated with metal oxides and hydroxides marked with *.

Table 2.4. Average metal content, as determined by XPS survey scans of 4-5 samples for each treatment.

Metal salts	Surface metal content (atom %)
$FeCl_3$	7.3 (6.2-8.8)
$FeCl_2$	5.9 (5.2-7.3)
$NiCl_2$	2.0 (1.5-2.3)
$CuCl_2$	1.7 (1.3-2.2)
PR48	0.0

A redshift of 400 – 800 meV in the O 1s peak is observed for divalent-infused samples (**Figure 2.13**), indicating weaker interactions with oxygen-containing groups on the polymer chains. According to Pearson's hard and soft acid–base (HSAB) theory, Fe^{3+} forms strong coordination bonds with hard bases, such as the oxygen atoms in ester groups (*e.g.,* in esters and carboxylic acids) present in PR48. Fe^{2+} sites are less acidic than the Fe^{3+} sites [31]. Divalent metal cations generally interact to a lesser extent with hard bases than trivalent cations, with the interaction strength following the order: $Fe^{2+} \geq Ni^{2+} > Cu^{2+}$ [39,40]. Stronger metal-ligand bonds, combined with the tendency of Fe species to form metal oxides and hydroxides that serve as nucleation sites, explain why Fe^{3+} interacts most strongly with the polymer surface. The relatively weak interaction between Cu^{2+} and the polymer surfaces accounts for the low metal content observed on the Cu^{2+}modified polymer sample. The XPS survey results also indicate that the samples coated with Fe^{3+} achieve higher metal content on the polymer surface than the other metals tested. (**Table 2.4**)

Ni^{2+} is less likely than Fe^{2+} to form oxide or hydroxide clusters, and hydroxides formed from Ni salts are more reversible, as shown in the Pourbaix diagram **(Figure 2.14)** [37,38]. NiO exhibits its main O 1s feature near 529 eV (oxide oxygen), while $Ni(OH)_2$ exhibits its main O 1s peak near 531 eV corresponding to hydroxyl oxygen. The absence of these two peaks in Ni^{2+} samples confirm that no oxide or hydroxide clusters are present on and near the polymer surface. The formation of Cu^{2+}-facilitated hydroxides and oxides, as predicted by the Pourbaix diagram, is more likely than that facilitated by Ni^{2+} **(Figure 2.14)**. The O 1s binding energy for CuO centers around 529.8 eV, whereas for $Cu(OH)_2$ it occurs near 531.8 eV. However, due to the weak interactions between the O groups on polymer chains and Cu^{2+} [35], Cu in the form of hydroxide and oxide was not detected either. This study suggests that strong interactions between metal cations and ester groups in the polymer, combined with the tendency to form metal hydroxides and oxides, play a significant role in the formation of a conformal catalyst coating on the polymer surface.

2.4.3. Catalytic degradation demonstrated with lowered decomposition temperature

(Sample preparation and TGA are done by Sam and me, but DTG analysis is done by Samuel P. Chiovoloni)

According to thermogravimetric analysis (TGA) at a heating rate of 20 °C/min, significant mass loss occurs around 410 – 460 °C **(Figure 2.15.a)**, which shifts slightly to 380 – 430 °C at a lower heating rate of 2.5 °C/min. All metal-salt-infused samples reduced the polymer degradation temperatures (**Figure 2.15.a**). Among them, Fe^{3+} catalyzed polymer degradation at a considerably lower temperature, slightly below 200 °C, compared to 260 °C for the unmodified polymer. The DTG (Derivative Thermogravimetric) curves (**Figure 2.15.b**) indicate that Ni^{2+}, Fe^{2+}, and Fe^{3+} infused polymers undergo substantial mass loss at lower temperatures relative to pure PR48 and the Cu^{2+} infused sample. These findings support the contention that metal salts, Ni^{2+}, Fe^{2+}, and Fe^{3+}, are effective decomposition catalysts, with their catalytic effectiveness correlating well with their coordination affinity for oxygen groups on the polymer.

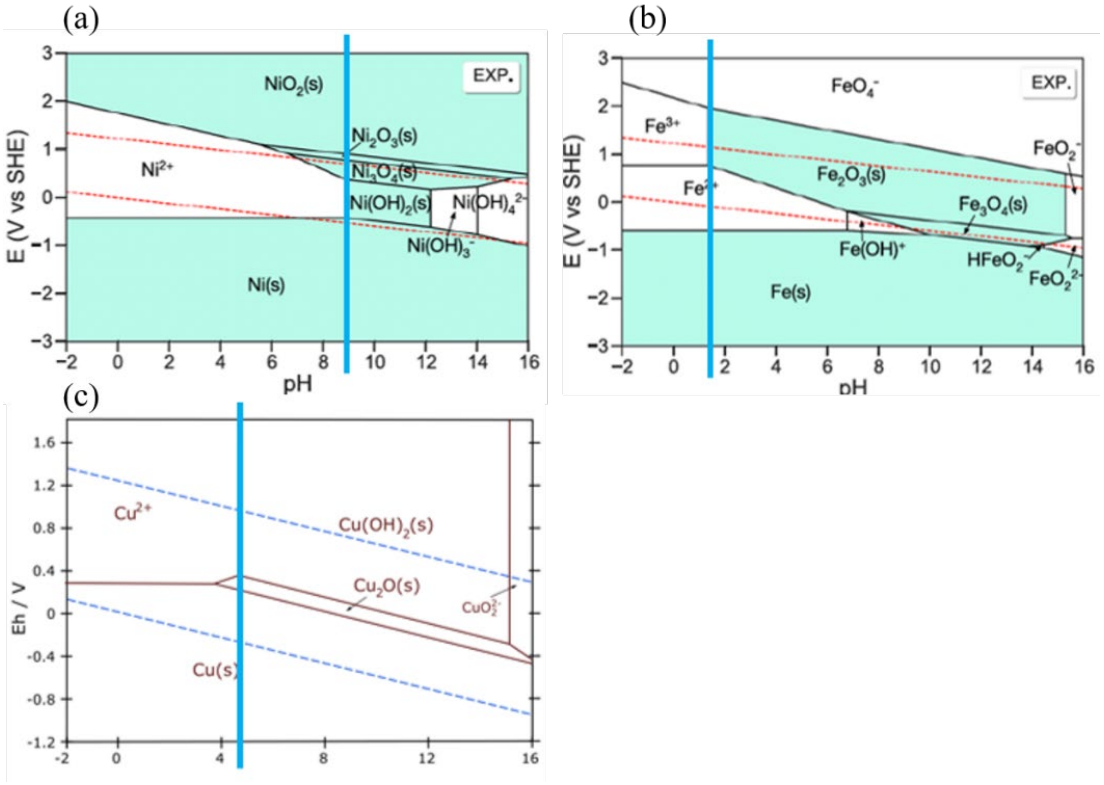


Figure 2.14. Pourbaix diagram of (a) Ni, (b) Fe, (c) Cu, showing the energy for metal oxide reduced to metal Cu^{2+} < Ni^{2+} <Fe^{3+} (orange line $\Delta G = -nF\Delta E$ (potential)) and onset pH for the formation of Ni and Fe hydroxides and oxides (blue vertical line).

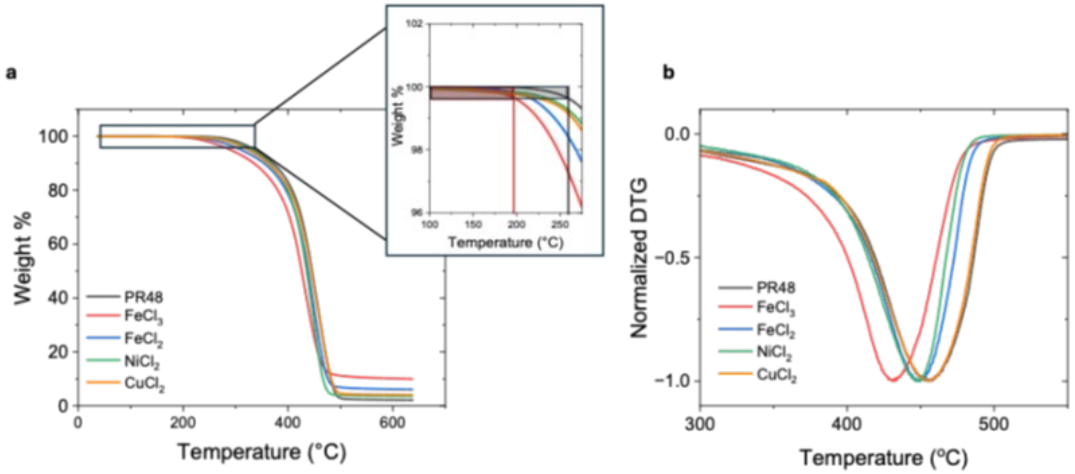
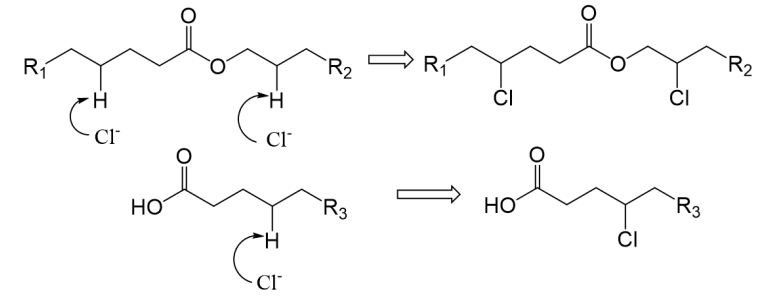


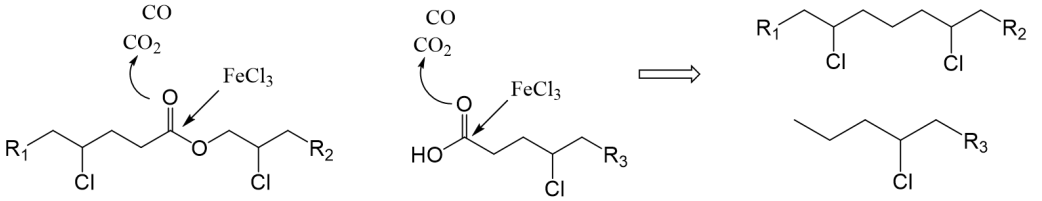
Figure 2.15. (a) Thermogravimetric analysis (TGA) results for metal salt-soaked PR48 samples (via approach 1) with an inset to highlight the variance of the onset; (b) normalized derivative thermogravimetric (DTG) curves of mass loss rate vs. temperature showing the degradation profile variation of different metal species.

Among all the catalysts tested, $FeCl_3$ lowers the decomposition temperature the most, likely because Fe^{3+} ions have the highest electron affinity and the highest loading on the 3D polymer samples after soaking. **Figure 2.16** illustrates the hypothesis for how $FeCl_3$ catalyzes polymer-to-carbon conversion at elevated temperatures [21,23,41,42]. As a strong Lewis acid, $FeCl_3$ breaks polymer chains during thermal annealing by allowing chlorine anions (Cl^-) to substitute for hydrogen atoms on the polymer backbone (**Figure 2.16**, reaction 1). $FeCl_3$ catalyzes decarboxylation, decarbonylation, and hydrogenation in addition to hydrolysis [18], leading to the formation of olefin-containing polymers (**Figure 2.16**, reactions 2-3). Further Cl^- on the polymer chains can be incorporated into $FeCl_3$ to produce $FeCl_4^-$, which leads to the formation of carbenium ions. These carbenium ions induce crosslinking between olefins or conjugated unsaturated polymer chains (**Figure 2.16**, reaction 5) [21,23,43]. Additionally, thermally activated parallel reactions such as isomerization, aromatization, and cyclization further contribute to char formation (**Figure 2.16**, reaction 6).

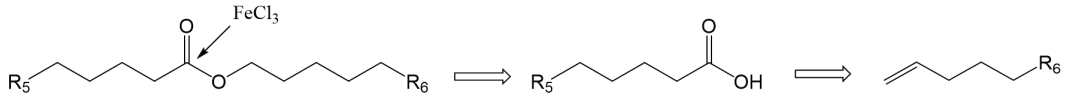
Reaction 1. Chlorine ion substitutes for hydrogen atoms by breaking the C-H bond to form Cl substitution



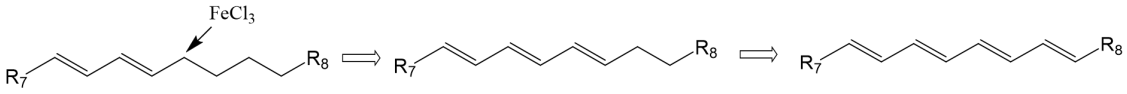
Reaction 2. $FeCl_3$ induced decarbonylation and decarboxylation



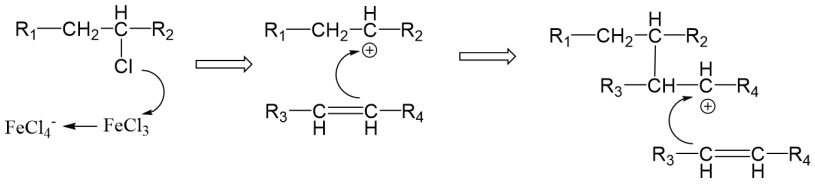
Reaction 3. $FeCl_3$ promotes hydrolysis



Reaction 4. $FeCl_3$ catalyzes dehydrogenation



Reaction 5. $FeCl_3$ crosslinks polymer chains to form carbon precursors



Reaction 6. $FeCl_3$ induces dehydrogenation and subsequent thermal decomposition of olefins leads to cyclization, Diels-Alder reaction

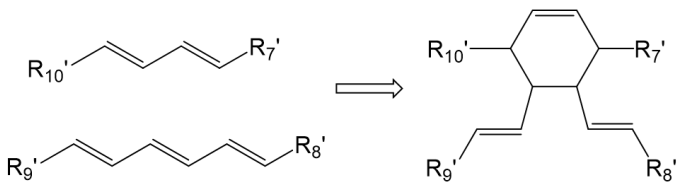


Figure 2.16. Schematic reactions promoted by $FeCl_3$ during pyrolysis. [21,23,41,42]

2.4.4. Enhanced graphitization with different transition metal catalysts

(Samples prepared by me, and Raman spectra are collected by Samuel P. Chiovoloni)

Raman spectroscopic analysis was used to evaluate the graphitic quality of the pyrolyzed carbon from 3D polymer templates. The characteristic Raman features are the first-order G-band at 1580–1600 cm^{-1} and D-band at 1340–1360 cm^{-1}.[44] The G-band is associated with the stretching of sp^2-hybridized C=C pairs, caused by single resonance scattering, while the D band is attributed to sp^3 carbon, caused by edge and defective effects [45,46].

Here, we selected a four-peak (G, D1, D3, D4) deconvolution model for the Raman spectra of our 3D-printed pyrolytic carbon samples because of its stability and clarity of different carbon contributions, which is the most commonly used model to investigate pyrolytic carbons.[44,47–50] Two- and three-peak models cannot separately account for the amorphous carbon contribution (D3, ~1500 cm^{-1}, very disordered) and the low wavenumber sp^2–sp^3 or edge mode (D4, ~1150–1200 cm^{-1}), leading to systematic misallocation of intensity between the G and D1 bands and unreliable ID/IG ratios.[44] In contrast, adding a fifth peak (D2, ~1620 cm^{-1}) offered only marginal improvements in fitting but introduced large instability in the extracted intensity ratios.[44,51,52] Also, D2 is only visually obvious in highly graphitic materials, and it merges with the G band in sufficiently disordered carbons (**Figure 2.17**). Because the 3D pyrolytic carbons are glassy carbons combined with graphitic carbon rather than highly graphitic carbon only, the D2 feature is not physically resolvable and is effectively subsumed into the asymmetric G band.

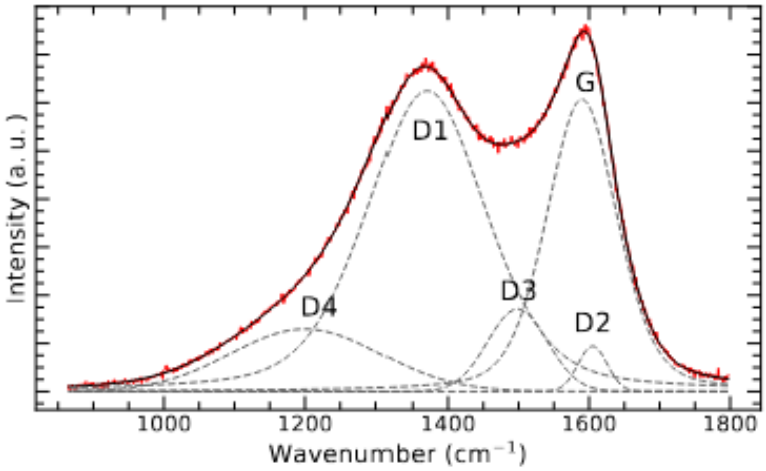


Figure 2.17. Example spectrum of standard modulus carbon fiber with possible peak components shown: D1, D2, D3, D4, G band. [44]

Figure 2.18 displays the Raman spectra in the D and G band region for the metal-soaked samples via approach 1. The broad D peak can further be broken down into the sp^3 edge defect-related contribution D1 (1350 cm^{-1}), the graphitic ordering contribution D2 (1620 cm^{-1}), the amorphous sp^3 contribution D3 (1500 cm^{-1}), and impurity contribution D4 (1180 cm^{-1}) [53], as shown in **Figure 2.19**. The Cu^{2+}-treated and neat polymer both exhibit a higher degree of amorphous character and contain greater amounts of impurities (D4) than other metal-catalyst-treated samples, indicating a lower graphitic ratio in their carbon structures.

The intensity ratio of the D1 and G bands (I_{D1}/I_G) is widely used to represent the degree of graphitization, with a lower I_{D1}/I_G ratio corresponding to a more graphitic state. Enhanced graphitization is observed in samples infused with Fe^{3+} salts, as demonstrated by the lowest I_{D1}/I_G ratio. This result aligns with previous studies of biomass conversion using Fe-based catalysts. [21,23,41,54] $FeCl_3$ has the lowest I_{D1}/I_G value, indicating it has the most graphitic carbon content, due to its highest loading and highest catalytic

graphitization activity.

Among the three divalent metal-treated samples, Fe^{2+} and Ni^{2+} resulted in higher graphitic content than Cu^{2+}, consistent with the fact that Ni and Fe promote the transformation of hydrocarbons into graphitic carbon and carbon nanostructures [54–56]. In contrast, the Cu^{2+} sample exhibits the highest defect level, comparable to that observed in the untreated polymer. I hypothesize that this is because $CuCl_2$ can absorb some degradation products during pyrolysis but can't promote the graphitization of the resulting amorphous carbon at high temperatures due to its filled d orbitals. The amorphous carbons derived from the hydrocarbon byproducts have a higher defect ratio than the glassy carbons derived from the polymer template, making the $CuCl_2$-treated samples have the highest I_{D1}/I_G ratio. Another interesting phenomenon is that Fe^{2+}-treated samples have a higher I_{D1}/I_G ratio than Ni^{2+}-treated samples, which is contradictory to the catalytic graphitization effect. My hypothesis is that $FeCl_2$ can capture more degraded hydrocarbon gases and convert them into carbon during pyrolysis; however, the Fe loading in $FeCl_2$-treated samples is insufficient to graphitize the excess carbon into graphitic carbon, as in $FeCl_3$-treated samples. The carbons derived from the hydrocarbon byproducts are only partially transferred into ordered glassy/graphitic carbons, making the $FeCl_2$-treated samples have a higher I_{D1}/I_G ratio than the $NiCl_2$-treated samples.

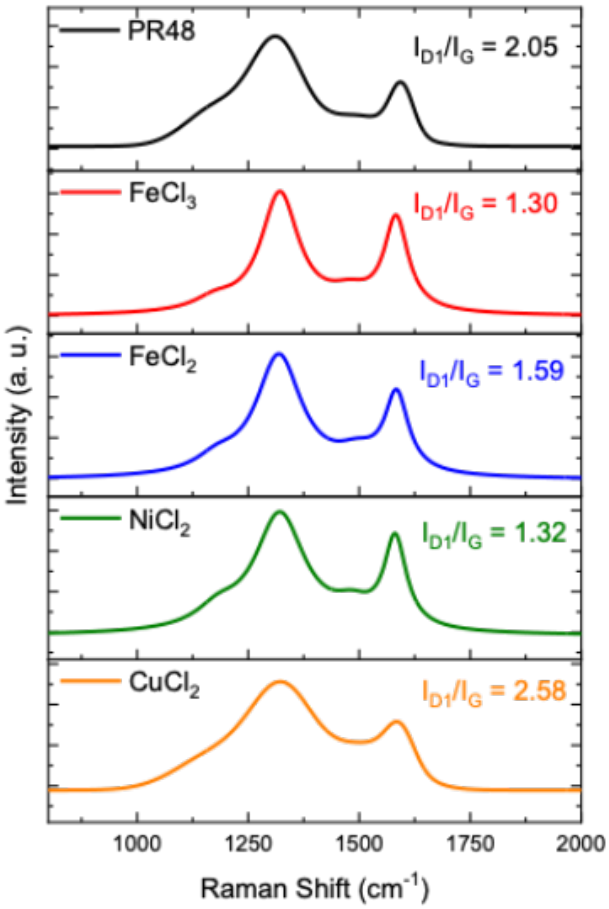


Figure 2.18. Raman spectra of carbon samples after 900°C pyrolysis and ratios of D1 and G bands used to distinguish between amorphous and graphitic carbon content. For XPS measurements, two samples were analyzed for each condition at six different locations.

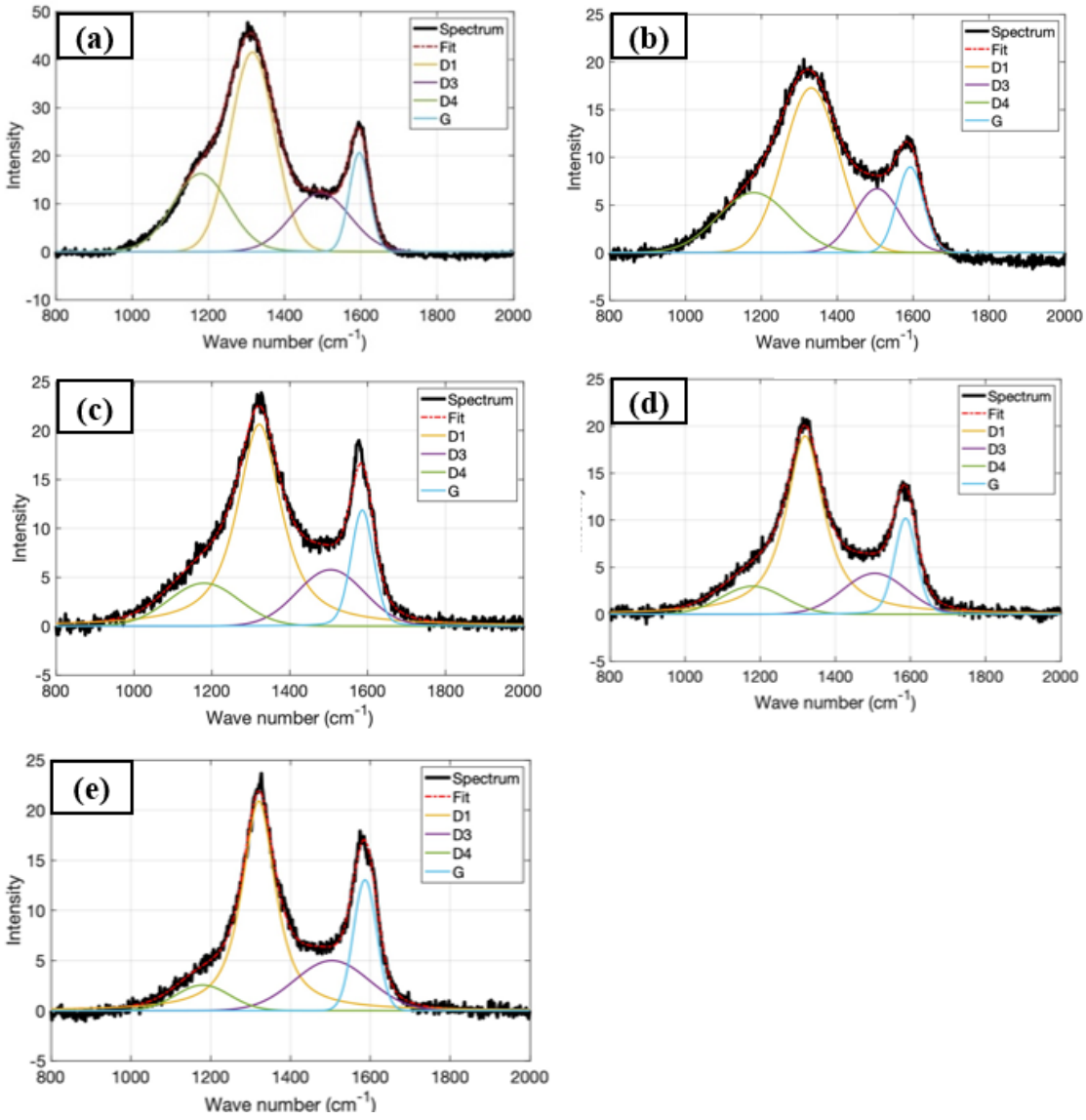


Figure 2.19. Raman data fitted by a four-peak model using Gaussian functions of the Figure 4 spectra demonstrating a more precise distinction of D1, D3, D4, and G band peaks. (a) Neat polymer, (b) $CuCl_2$, (c) $NiCl_2$, (d) $FeCl_2$ and (e) $FeCl_3$.

2.5. Conclusion

This work presents a simple and cost-effective strategy for fabricating geometrically tailored carbon microstructures with tunable properties by converting high-throughput 3D-printed polymers coated with a conformal catalyst layer. These results show that the redox activity and partially filled d-orbitals of transition metals play a critical role in promoting both carbonization and graphitization, with the synergistic coupling of these processes being essential for enhancing carbon yield. Raman analysis confirms that Ni- and Fe-based treatments significantly increase the degree of graphitization.

The choice of metal catalyst strongly influences the resulting carbon structure. When pyrolyzing a polymeric template at 900 °C, Ni^{2+}-treated samples yield porous carbon, whereas Fe^{2+}- and Fe^{3+}-treated samples produce at least a twofold increase in char yield. In contrast, Cu^{2+} treatment results in dense carbon

struts with serious dimensional shrinkage. The dimensional retention follows the trend $Cu^{2+} < Ni^{2+} < Fe^{2+} < Fe^{3+}$, while final strut size follows $Ni^{2+} < Cu^{2+} < Fe^{2+} < Fe^{3+}$, highlighting the critical role of catalyst selection in dictating structural outcomes.

Among the different catalysts studied, environmentally benign and low-cost $FeCl_3$ is the most effective, enabling both enhanced graphitization and superior dimensional retention. By tuning the thickness of the catalyst overcoat, carbon yield, morphology, and structural fidelity can be systematically controlled; a 6~8 μm coating increases carbon yield by up to fivefold. Additionally, Ni^{2+} functions as a trifunctional catalyst: during pyrolysis, NiO undergoes carbothermal reduction, enabling one-step formation of porous carbon. Fe- and Ni-based overcoats also induce a pinning effect that stabilizes the polymer framework during pyrolysis, prolonging graphitization while suppressing structural collapse. Using high-resolution polymer lattices with 50 μm struts, Fe^{3+} treatment yields carbon struts of approximately 43 μm, corresponding to more than a fourfold improvement in dimensional retention compared to untreated samples. This high-fidelity polymer-to-carbon conversion enables dense micro-architected carbon structures with high fill factors, thereby increasing accessible surface area and supporting enhanced volumetric electrochemical performance.

In summary, the catalyst overcoat alters polymer decomposition pathways by promoting dehydrogenation, decarbonylation, decarboxylation, cyclization, and aromatization. Concurrently, it helps retain degradation products, further boosting carbon yield and structural integrity. The conformally deposited metal salts partially infiltrate the polymer surface, and the synergistic interaction between metal cations and chloride anions is key to achieving these effects—behavior not observed with corresponding metal oxides.

This straightforward process, which uses transition metal catalysts to facilitate the transformation of 3D-printed polymers into carbon microstructures, represents a breakthrough in material processing with tunable properties, enabling applications in energy storage, electrochemical sensing, water purification, electronics cooling, and beyond.

Reference

[1] H.-L. Kuo, P.R. Onffroy, S.P. Chiovoloni, L. Williams, J.M. DeSimone, J. Lu, Engineered 3D micro-architected carbon structures via conformal deposition of multifunctional transition metal catalysts, Carbon 247 (2026) 121043. https://doi.org/10.1016/j.carbon.2025.121043.

[2] P.R. Onffroy, S. Chiovoloni, H.L. Kuo, M.A. Saccone, J.Q. Lu, J.M. DeSimone, Opportunities at the Intersection of 3D Printed Polymers and Pyrolysis for the Microfabrication of Carbon-Based Energy Materials, JACS Au 4 (2024) 3706–3726. https://doi.org/10.1021/jacsau.4c00555.

[3] X. Wang, S. Huo, Y. Chen, Z. Cai, G. Fu, Y. Dai, J. Zou, d-orbital hybridization in transition metal electrocatalysts: Correlating electronic structure with catalytic performance, Materials Science and Engineering: R: Reports 168 (2026) 101147. https://doi.org/10.1016/j.mser.2025.101147.

[4] Q. Yan, J. Li, X. Zhang, E.B. Hassan, C. Wang, J. Zhang, Z. Cai, Catalytic graphitization of kraft lignin to graphene-based structures with four different transitional metals, J Nanopart Res 20 (2018) 223. https://doi.org/10.1007/s11051-018-4317-0.

[5] Fe-FeC Phase Equilibrium Diagram, (n.d.). https://practicalmaintenance.net/?p=1315 (accessed July 29, 2026).

[6] H. Amara, J.-M. Roussel, C. Bichara, J.-P. Gaspard, F. Ducastelle, Tight-binding potential for atomistic simulations of carbon interacting with transition metals: Application to the Ni-C system, Phys. Rev. B 79 (2009) 014109. https://doi.org/10.1103/PhysRevB.79.014109.

[7] J.-F. Silvain, J.-M. Heintz, A. Veillere, L. Constantin, Y.F. Lu, A review of processing of Cu/C base plate composites for interfacial control and improved properties, Int. J. Extrem. Manuf. 2 (2020) 012002. https://doi.org/10.1088/2631-7990/ab61c5.

[8] Y.-L. Loow, T.Y. Wu, Y.S. Lim, K.A. Tan, L.F. Siow, J. Md. Jahim, A.W. Mohammad, Improvement of xylose recovery from the stalks of oil palm fronds using inorganic salt and oxidative agent, Energy Conversion and Management 138 (2017) 248–260. https://doi.org/10.1016/j.enconman.2016.12.015.

[9] C. Zhang, L. Zhang, Q. Li, Y. Wang, Q. Liu, T. Wei, D. Dong, S. Salavati, M. Gholizadeh, X. Hu, Catalytic pyrolysis of poplar wood over transition metal oxides: Correlation of catalytic behaviors with physiochemical properties of the oxides, Biomass and Bioenergy 124 (2019) 125–141. https://doi.org/10.1016/j.biombioe.2019.03.017.

[10] M. Ji, L. Chen, J. Que, L. Zheng, Z. Chen, Z. Wu, Effects of transition metal oxides on pyrolysis properties of PVC, Process Safety and Environmental Protection 140 (2020) 211–220. https://doi.org/10.1016/j.psep.2020.04.010.

[11] S. Xia, H. Yang, shuaishuai Lei, W. Lu, N. Cai, H. Xiao, Y. Chen, H. Chen, Iron salt catalytic pyrolysis of biomass: Influence of iron salt type, Energy 262 (2023) 125415. https://doi.org/10.1016/j.energy.2022.125415.

[12] M. Ji, L. Chen, J. Que, L. Zheng, Z. Chen, Z. Wu, Effects of transition metal oxides on pyrolysis properties of PVC, Process Safety and Environmental Protection 140 (2020) 211–220. https://doi.org/10.1016/j.psep.2020.04.010.

[13] S. Xia, H. Yang, S. Lei, W. Lu, N. Cai, H. Xiao, Y. Chen, H. Chen, Iron salt catalytic pyrolysis of biomass: Influence of iron salt type, Energy 262 (2023) 125415. https://doi.org/10.1016/j.energy.2022.125415.

[14] D. Pan, M. Ombaba, Z.-Y. Zhou, Y. Liu, S. Chen, J. Lu, Direct Growth of Carbon Nanofibers to Generate a 3D Porous Platform on a Metal Contact to Enable an Oxygen Reduction Reaction, ACS Nano 6 (2012) 10720–10726. https://doi.org/10.1021/nn303910w.

[15] C.P. Deck, K. Vecchio, Prediction of carbon nanotube growth success by the analysis of carbon–

catalyst binary phase diagrams, Carbon 44 (2006) 267–275. https://doi.org/10.1016/j.carbon.2005.07.023.

[16] D. Yao, C.-H. Wang, Pyrolysis and in-line catalytic decomposition of polypropylene to carbon nanomaterials and hydrogen over Fe- and Ni-based catalysts, Applied Energy 265 (2020) 114819. https://doi.org/10.1016/j.apenergy.2020.114819.

[17] H. Yu, Z. Jiang, J.W. Gilman, T. Kashiwagi, J. Liu, R. Song, T. Tang, Promoting carbonization of polypropylene during combustion through synergistic catalysis of a trace of halogenated compounds and Ni2O3 for improving flame retardancy, Polymer 50 (2009) 6252–6258. https://doi.org/10.1016/j.polymer.2009.10.068.

[18] Y. Sun, X. Lu, S. Zhang, R. Zhang, X. Wang, Kinetic study for Fe(NO3)3 catalyzed hemicellulose hydrolysis of different corn stover silages, Bioresource Technology 102 (2011) 2936–2942. https://doi.org/10.1016/j.biortech.2010.11.076.

[19] J. Gong, J. Liu, L. Ma, X. Wen, X. Chen, D. Wan, H. Yu, Z. Jiang, E. Borowiak-Palen, T. Tang, Effect of Cl/Ni molar ratio on the catalytic conversion of polypropylene into Cu–Ni/C composites and their application in catalyzing “Click” reaction, Applied Catalysis B: Environmental 117–118 (2012) 185–193. https://doi.org/10.1016/j.apcatb.2012.01.015.

[20] A. Gomez-Martin, A. Gutierrez-Pardo, J. Martinez-Fernandez, J. Ramirez-Rico, Binder-free supercapacitor electrodes: Optimization of monolithic graphitized carbons by reflux acid treatment, Fuel Processing Technology 199 (2020) 106279. https://doi.org/10.1016/j.fuproc.2019.106279.

[21] Z. Xu, Y. Zhou, Z. Sun, D. Zhang, Y. Huang, S. Gu, W. Chen, Understanding reactions and pore-forming mechanisms between waste cotton woven and FeCl3 during the synthesis of magnetic activated carbon, Chemosphere 241 (2020) 125120. https://doi.org/10.1016/j.chemosphere.2019.125120.

[22] W.-J. Liu, K. Tian, Y.-R. He, H. Jiang, H.-Q. Yu, High-Yield Harvest of Nanofibers/Mesoporous Carbon Composite by Pyrolysis of Waste Biomass and Its Application for High Durability Electrochemical Energy Storage, Environ. Sci. Technol. 48 (2014) 13951–13959. https://doi.org/10.1021/es504184c.

[23] J. Bedia, M. Peñas-Garzón, A. Gómez-Avilés, J.J. Rodriguez, C. Belver, Review on Activated Carbons by Chemical Activation with FeCl3, C 6 (2020) 21. https://doi.org/10.3390/c6020021.

[24] J. Ren, F.-F. Li, J. Lau, L. González-Urbina, S. Licht, One-Pot Synthesis of Carbon Nanofibers from CO2, Nano Lett. 15 (2015) 6142–6148. https://doi.org/10.1021/acs.nanolett.5b02427.

[25] H.S.C. O’Neill, Systems Fe-O and Cu-O: Thermodynamic data for the equilibria Fe-"FeO," Fe-Fe3O4, “feO”-Fe3O4, Fe3O4-Fe2O3, Cu-Cu2O, and Cu2O-CuO from emf measurements, American Mineralogist: An International Journal of Earth and Planetary Materials 73 (1988) 470–486.

[26] S.M. Grimes, H. Lateef, A.J. Jafari, L. Mehta, Studies of the effects of copper, copper(II) oxide and copper(II) chloride on the thermal degradation of poly(vinyl chloride), Polymer Degradation and Stability 91 (2006) 3274–3280. https://doi.org/10.1016/j.polymdegradstab.2006.06.010.

[27] J.-Y. Kim, D. Hong, J.-C. Lee, H.G. Kim, S. Lee, S. Shin, B. Kim, H. Lee, M. Kim, J. Oh, G.-D. Lee, D.-H. Nam, Y.-C. Joo, Quasi-graphitic carbon shell-induced Cu confinement promotes electrocatalytic CO2 reduction toward C2+ products, Nat Commun 12 (2021) 3765. https://doi.org/10.1038/s41467-021-24105-9.

[28] M. Blazsó, B. Zelei, Thermal decomposition of low-density polyethylene in the presence of iron and copper chlorides, Journal of Analytical and Applied Pyrolysis 36 (1996) 149–158. https://doi.org/10.1016/0165-2370(96)00928-X.

[29] L. Ji, A. Hervier, M. Sablier, Study on the pyrolysis of polyethylene in the presence of iron and copper chlorides, Chemosphere 65 (2006) 1120–1130. https://doi.org/10.1016/j.chemosphere.2006.04.029.

[30] B. Vincent Crist, XPS guide for insulators: Electron flood gun operation and optimization, surface

charging, controlled charging, differential charging, useful FWHMs, problems and solutions, and advice, Journal of Vacuum Science & Technology A 42 (2024) 032803. https://doi.org/10.1116/6.0003439.

[31] T. Devic, C. Serre, High valence 3p and transition metal based MOFs, Chemical Society Reviews 43 (2014) 6097–6115. https://doi.org/10.1039/C4CS00081A.

[32] S.L. Tait, Y. Wang, G. Costantini, N. Lin, A. Baraldi, F. Esch, L. Petaccia, S. Lizzit, K. Kern, Metal−Organic Coordination Interactions in Fe−Terephthalic Acid Networks on Cu(100), J. Am. Chem. Soc. 130 (2008) 2108–2113. https://doi.org/10.1021/ja0778186.

[33] M.D. Reale Batista, S. Chandrasekaran, B.D. Moran, M. Salazar De Troya, A. Pinongcos, Z. Wang, R. Hensleigh, A. Carleton, M. Zeng, T. Roy, D. Lin, X. Xue, V.A. Beck, D.A. Tortorelli, M. Stadermann, R. Zheng, Y. Li, M.A. Worsley, Design and additive manufacturing of optimized electrodes for energy storage applications, Carbon 205 (2023) 262–269. https://doi.org/10.1016/j.carbon.2023.01.044.

[34] S. Zhao, X. Song, X. Chai, P. Zhao, H. He, Z. Liu, Green production of fluorescent carbon quantum dots based on pine wood and its application in the detection of Fe3+, Journal of Cleaner Production 263 (2020) 121561. https://doi.org/10.1016/j.jclepro.2020.121561.

[35] J.-C. Wang, J. Ren, H.-C. Yao, L. Zhang, J.-S. Wang, S.-Q. Zang, L.-F. Han, Z.-J. Li, Synergistic photocatalysis of Cr(VI) reduction and 4-Chlorophenol degradation over hydroxylated α-Fe2O3 under visible light irradiation, Journal of Hazardous Materials 311 (2016) 11–19. https://doi.org/10.1016/j.jhazmat.2016.02.055.

[36] Q. Wu, B. Xiao, Q. Liu, H. Deng, Z. Ye, Y. Li, R. Yao, J. Zhu, New strategy for enhancing interfacial adhesion between carbon fiber and epoxy by using mussel-inspired polydopamine-Fe complex nanospheres, Composites Part B: Engineering 266 (2023) 111032. https://doi.org/10.1016/j.compositesb.2023.111032.

[37] File:Cu-pourbaix-diagram.svg - Wikipedia, (2007). https://commons.wikimedia.org/wiki/File:Cu-pourbaix-diagram.svg (accessed September 18, 2025).

[38] Z. Wang, X. Guo, J. Montoya, J.K. Nørskov, Predicting aqueous stability of solid with computed Pourbaix diagram using SCAN functional, Npj Comput Mater 6 (2020) 160. https://doi.org/10.1038/s41524-020-00430-3.

[39] S. Bruno, S. Bettati, M. Manfredini, A. Mozzarelli, M. Bolognesi, D. Deriu, C. Rosano, A. Tsuneshige, T. Yonetani, E.R. Henry, Oxygen binding by α(Fe2+)2β(Ni2+)2 hemoglobin crystals, Protein Science 9 (2000) 683–692. https://doi.org/10.1110/ps.9.4.683.

[40] Z. Cai, D. Zhou, M. Wang, S.-M. Bak, Y. Wu, Z. Wu, Y. Tian, X. Xiong, Y. Li, W. Liu, S. Siahrostami, Y. Kuang, X.-Q. Yang, H. Duan, Z. Feng, H. Wang, X. Sun, Introducing Fe2+ into Nickel–Iron Layered Double Hydroxide: Local Structure Modulated Water Oxidation Activity, Angewandte Chemie International Edition 57 (2018) 9392–9396. https://doi.org/10.1002/anie.201804881.

[41] X. Yang, Y. Zhao, R. Li, Y. Wu, M. Yang, A modified kinetic analysis method of cellulose pyrolysis based on TG–FTIR technique, Thermochimica Acta 665 (2018) 20–27. https://doi.org/10.1016/j.tca.2018.05.008.

[42] S. Xia, K. Li, H. Xiao, N. Cai, Z. Dong, C. xu, Y. Chen, H. Yang, X. Tu, H. Chen, Pyrolysis of Chinese chestnut shells: Effects of temperature and Fe presence on product composition, Bioresource Technology 287 (2019) 121444. https://doi.org/10.1016/j.biortech.2019.121444.

[43] S. Stoeva, M. Karaivanova, D. Benev, Poly(vinyl chloride) composition. II. Study of the flammability and smoke-evolution of unplasticized poly(vinyl chloride) and fire-retardant additives, Journal of Applied Polymer Science 46 (1992) 119–127. https://doi.org/10.1002/app.1992.070460112.

[44] Z.E. Brubaker, J.J. Langford, R.J. Kapsimalis, J.L. Niedziela, Quantitative analysis of Raman spectral

parameters for carbon fibers: practical considerations and connection to mechanical properties, J Mater Sci 56 (2021) 15087–15121. https://doi.org/10.1007/s10853-021-06225-1.

[45] A.C. Ferrari, Interpretation of Raman spectra of disordered and amorphous carbon, Phys. Rev. B 61 (2000) 14095–14107. https://doi.org/10.1103/PhysRevB.61.14095.

[46] Z. Li, L. Deng, I.A. Kinloch, R.J. Young, Raman spectroscopy of carbon materials and their composites: Graphene, nanotubes and fibres, Progress in Materials Science 135 (2023) 101089. https://doi.org/10.1016/j.pmatsci.2023.101089.

[47] J.Y. Cai, J. McDonnell, C. Brackley, L. O'Brien, J.S. Church, K. Millington, S. Smith, N. Phair-Sorensen, Polyacrylonitrile-based precursors and carbon fibers derived from advanced RAFT technology and conventional methods – The 1st comparative study, Materials Today Communications 9 (2016) 22–29. https://doi.org/10.1016/j.mtcomm.2016.09.001.

[48] Q. Niu, S. Zhao, K. Gao, L. Wang, Polyacrylonitrile-Based Nitrogen-Doped Carbon Materials with Different Micro-morphology Prepared by Electrostatic Field for Supercapacitors, J. Electron. Mater. 48 (2019) 5264–5272. https://doi.org/10.1007/s11664-019-07332-1.

[49] M.B. Vázquez-Santos, E. Geissler, K. László, J.-N. Rouzaud, A. Martínez-Alonso, J.M.D. Tascón, Comparative XRD, Raman, and TEM Study on Graphitization of PBO-Derived Carbon Fibers, J. Phys. Chem. C 116 (2012) 257–268. https://doi.org/10.1021/jp2084499.

[50] H. Xiao, Y. Lu, M. Wang, X. Qin, W. Zhao, J. Luan, Effect of gamma-irradiation on the mechanical properties of polyacrylonitrile-based carbon fiber, Carbon 52 (2013) 427–439. https://doi.org/10.1016/j.carbon.2012.09.054.

[51] G.A. Zickler, B. Smarsly, N. Gierlinger, H. Peterlik, O. Paris, A reconsideration of the relationship between the crystallite size *L*a of carbons determined by X-ray diffraction and Raman spectroscopy, Carbon 44 (2006) 3239–3246. https://doi.org/10.1016/j.carbon.2006.06.029.

[52] T. Zhang, L. Qi, S. Li, X. Chao, W. Tian, J. Zhou, Evaluation of the effect of PyC coating thickness on the mechanical properties of T700 carbon fiber tows, Applied Surface Science 463 (2019) 310–321. https://doi.org/10.1016/j.apsusc.2018.08.195.

[53] Z.E. Brubaker, J.J. Langford, R.J. Kapsimalis, J.L. Niedziela, Quantitative analysis of Raman spectral parameters for carbon fibers: practical considerations and connection to mechanical properties, J Mater Sci 56 (2021) 15087–15121. https://doi.org/10.1007/s10853-021-06225-1.

[54] Q. Yan, J. Li, X. Zhang, E.B. Hassan, C. Wang, J. Zhang, Z. Cai, Catalytic graphitization of kraft lignin to graphene-based structures with four different transitional metals, J Nanopart Res 20 (2018) 223. https://doi.org/10.1007/s11051-018-4317-0.

[55] D. Pan, M. Ombaba, Z.-Y. Zhou, Y. Liu, S. Chen, J. Lu, Direct Growth of Carbon Nanofibers to Generate a 3D Porous Platform on a Metal Contact to Enable an Oxygen Reduction Reaction, ACS Nano 6 (2012) 10720–10726. https://doi.org/10.1021/nn303910w.

[56] M. Acerce, S. Chiovoloni, Y. Hernandez, C. Ortuno, J. Qian, J. Lu, Poly(1,5-diaminonaphthalene)-Grafted Monolithic 3D Hierarchical Carbon as Highly Capacitive and Stable Supercapacitor Electrodes, ACS Appl Mater Interfaces 13 (2021) 53736–53745. https://doi.org/10.1021/acsami.1c13746.

Chapter 3 – Design of High-resolution 3D Carbon Electrodes via Tannic Acid and Metal Catalyst Integration from a 3D-Printed Elegoo Template

Graphitic carbon materials are widely used as electrode components in energy storage devices because their electronic conductivity, chemical stability, and tunable microstructure can directly influence charge transport and ion accessibility. [1–6] In particular, the ability to control graphitization and surface morphology is important for improving areal capacitance, since areal performance depends not only on intrinsic material properties but also on the density of active sites and the electrode surface area. Therefore, rational regulation of carbon structure has become a key strategy for designing high-performance electrodes. To improve the electrochemical and mechanical performance of pyrolytic 3D carbon derived from a polymer template, additional carbon precursors are introduced to play a decisive role during pyrolysis, as they determine the yield, microstructure, porosity, heteroatom content, and final performance of the carbon product. [7–9]

Here, we propose a post-printing, pre-pyrolysis treatment strategy that enhances both electrochemical performance and electrical conductivity, increases carbon yield, reduces shrinkage, and improves the degree of graphitization by introducing $FeCl_3$ and tannic acid as additional carbon precursors. Tannic acid is a promising additive carbon precursor 10–12], because it is rich in phenolic groups; it can undergo extensive crosslinking during thermal treatment and tends to promote char formation. Its aromatic structure promotes the formation of carbonaceous residues with relatively high carbon retention compared with those from simple small-molecule precursors. In addition, tannic acid can interact with metal species and polymer matrices, thereby creating a more homogeneous precursor network that is favorable for the fabrication of continuous carbon frameworks. [10,11,13]

As discussed in **Chapter 2**, $FeCl_3$ is the best catalyst to promote graphitization and carbon rearrangement during pyrolysis. During pyrolysis, Fe species can not only capture hydrocarbon byproducts generated during thermal decomposition but also facilitate the transformation of disordered carbon into more ordered graphitic domains, thereby improving electrical conductivity and reducing internal resistance. When the 3D acrylate-based Elegoo polymer template is soaked in the tannic acid–$FeCl_3$ ethanol solution, tannic acid readily impregnates and adsorbs onto the polymer surface via its abundant phenolic groups and strong affinity for polar sites on the template. At the same time, the phenolic hydroxyl groups of tannic acid coordinate with Fe^{3+} ions from $FeCl_3$, forming metal–polyphenol complexes that anchor the molecules more firmly onto the surface. [10,13]

Therefore, when Fe can act as a catalytic center for carbon rearrangement and graphitization during pyrolysis, TA coordinated with Fe can influence the chemical environment around it. By tuning the Fe/TA ratio, it is possible to regulate the extent of catalytic graphitization, the formation of graphitic and glassy carbon, and the development of surface features such as roughness, porosity, and hierarchical texture. These structural changes can significantly affect specific surface area, electrode–electrolyte contact, and electrical conductivity, all of which are critical for high areal capacitance.

3.1. Selection of tannic acid as carbon precursor

Common carbon precursors used for preparing carbon materials include tannic acid, chitosan, cellulose, glucose, sucrose, and other biomass-derived or polymeric compounds. (Shown in **Table 3.1**) Tannic acid is attractive because it is abundant, rich in aromatic and oxygen-containing groups, and can yield carbon with high carbonization efficiency and tunable surface functionality. In addition to these natural precursors, many synthetic organic and polymeric materials are also used when more controlled composition, morphology, or heteroatom doping is needed. These precursors are valued because they are often renewable, low-cost, and easy to process, and they can be converted into porous carbon frameworks by pyrolysis, hydrothermal carbonization, or activation. As a result, they are widely studied for supercapacitors, batteries, catalysts, adsorption, and other energy- and environment-related applications.

Table 3.1. Common carbon precursors for preparation of pyrolytic carbon materials

Precursor	Char yield and carbonization efficiency	Main advantages	Main limitations	Ref
Tannic acid	Char yield at 800 °C: 26-28 wt% (moderate to high); often good carbonization efficiency because it is aromatic and highly crosslinked, but values depend strongly on pyrolysis route and additives.	Phenolic/aromatic structure favors carbon formation; good source of heteroatom-containing carbon if coupled with N-doping or metal coordination.	More expensive than bulk biomass; not as scalable as agricultural wastes; properties depend on purity and formulation.	[7,10,11,14]
Chitosan	Char yield at 800 °C: 15 wt% (moderate); usually better than simple sugars and can be improved by crosslinking/activation; N-content helps retain useful functionality.	Intrinsic nitrogen content enables N-doped carbons	Lower char yield; serious shrinkage during carbonization.	[15]
Cellulose	Char yield at 800 °C: 5 wt% (low)	Abundant, cheap, renewable, high purity; excellent for making fibers, papers, aerogels, and templated carbons.	Low intrinsic carbon yield; weak graphitization without catalysts; can generate volatiles and low-density char.	[16–18]
Glucose	Char yield at 800 °C: 5~15 wt% (low-moderate); hydrothermal carbonization can improve carbonization yield, but dry pyrolysis gives relatively modest char.	Very controllable; easy to form spheres, hydrochars, and thin coatings; useful model precursor for mechanism studies.	Low char yield compared with lignin-rich biomass; carbon often needs activation or post-treatment to become highly conductive/porous.	[18,19]
Sucrose	Char yield at 800 °C: 20~30 wt% (moderate); similar to glucose as a small-molecule precursor, good hydrothermal/solvothermal carbon formation but limited intrinsic char yield.	Cheap, accessible, easy to carbonize; good for uniform carbon spheres and templated structures.	Low carbon yield and usually amorphous carbon unless strongly processed; needs activation for high surface area.	[20–22]
Lignin-rich biomass	Char yield of lignin at 800 °C: 35~45 wt% (high)	Highest natural carbon retention among plant biomacromolecules; aromatic structure favors higher yield	Composition is variable; extraction/purification can be difficult; the ash and impurities may affect	[17,23,24]

		and better carbon framework.	performance.	

Tannic acid (TA) is a natural polyphenol found in a wide variety of plants. It can be extracted from natural sources. Therefore, TA is one of the most abundant natural compounds of carbon precursors on Earth, surpassed only by cellulose, hemicellulose, chitosan, and lignin. In materials science, TA serves as a versatile supramolecular or chemical crosslinker, enabling the design of functional polymeric networks for various applications. Since TA is a complex polyphenolic compound containing numerous catechol and pyrogallol aromatic rings, it possesses the following unique chemical properties.

1. TA exhibits high solubility in water (exceeding 300 g/L) and maintains excellent stability once dissolved. [25,26]
2. As a low-cost, widely available natural polyphenol, TA is environmentally harmless and inherently biocompatible. Furthermore, it is both hydrolyzable and biodegradable.
3. TA can participate in diverse intermolecular interactions with various nucleophiles (such as amides, thiols, and amines). This multi-valent bonding capability endows it with robust adhesion across a wide range of material substrates.
4. The abundant hydroxyl groups on the TA structure allow it to effectively chelate metal ions.
5. Tannic acid has high intrinsic carbon content and aromatic polyphenolic structure. This property makes it an efficient building block for constructing metal-organic frameworks (MOFs), coordination networks, and a promising additive carbon precursor to improve 3D pyrolytic carbon char yield and mechanical integrity.

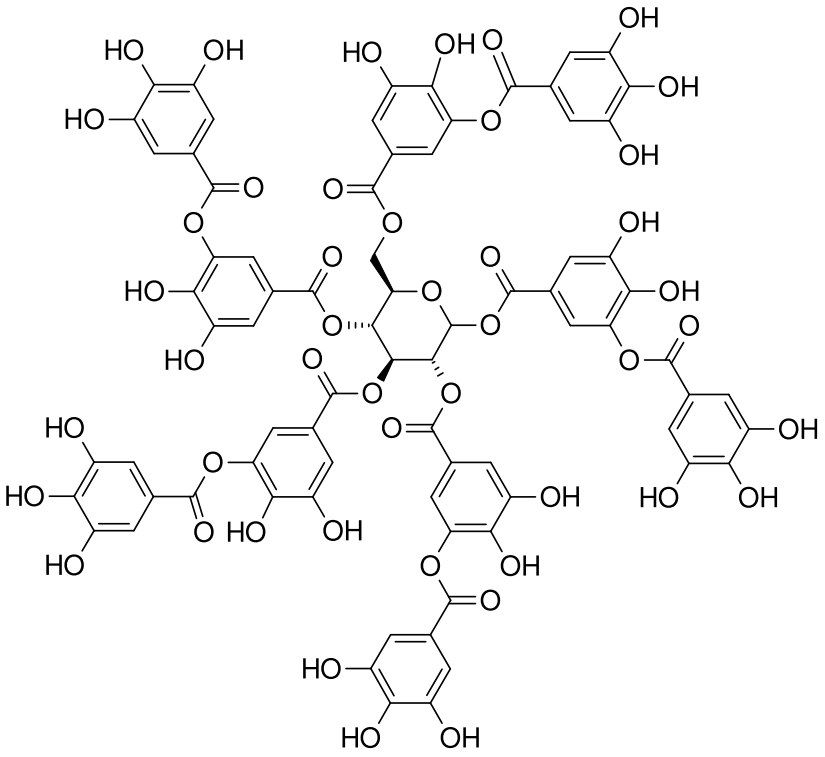


Figure 3.1. Chemical structure of tannic acid [10]

Tannic acid (TA) can interact with other chemicals through multiple different mechanisms, making it an effective natural crosslinker and interfacial binder. Its abundant phenolic hydroxyl groups enable strong hydrogen bonding with polar polymers, biomolecules, and surface functional groups, while its aromatic rings promote π–π stacking with conjugated or aromatic species.

1. Hydrogen bonding

Hydrogen bonding (H-bonding) is one of the most fundamental interactions in polyphenols, with strong adhesive capabilities across diverse surfaces. Since tannic acid (TA) contains a large number of phenolic groups, it can readily interact with various molecules containing a carboxyl group, hydroxyl group, amino group, or ester group through hydrogen bonding. [27] Therefore, the strong interactions mediated by hydrogen bonding among catechol or pyrogallol groups enable tannic acid derivatives to serve as underwater adhesives. [28] TA can also be used to crosslink polymers, such as poly(vinyl alcohol) (PVA), poly(ethylene glycol) (PEG), and poly(vinylpyrrolidone) (PVP), via hydrogen bonding in biomedical applications. [29]

2. π-π stacking

Tannic acid can interact with conjugated or aromatic species through π-π stacking. Graphene and tannic acid (TA) composite materials have attracted considerable interest for applications such as dye adsorption, material reinforcement, and the fabrication of three-dimensional (3D) graphene macrostructures. [12] Take graphene, for example; graphene has attracted considerable attention for its exceptional tensile strength, large specific surface area, and outstanding electrical conductivity.[30] However, graphene nanosheets are prone to aggregation and restacking due to strong π–π interactions, hydrophobic effects, and van der Waals forces, which significantly reduce their accessible surface area and limit their practical performance. To address this problem, Liu, Wang, and co-workers reported that natural phenolic compounds, such as TA, can effectively induce the self-assembly of graphene nanosheets into 3D architectures. [31] In their observation, TA strongly adsorbs onto the graphene surface through π–π interactions, thereby improving its dispersion stability in aqueous media. The phenyl rings in TA can interact with the basal graphene plane by enabling delocalized π-electrons to overlap and stabilizing the TA-graphene coordinated structure without covalent bonding. This interaction preserves the intrinsic electrical and chemical properties of graphene while providing abundant surface functional groups (hydroxyl and carbonyl) from TA that can participate in additional coordination, hydrogen bonding, or crosslinking. Additionally, TA serves as a reducing agent, converting graphene oxide (GO) into reduced graphene oxide (rGO), thereby enhancing the chemical stability of the resulting structure.

3. Metal-phenol network

Tannic acid (TA) can form metal–phenol networks by the strong chelation effect of its abundant catechol and pyrogallol hydroxyl groups with metal ions such as Fe^{3+}. Each galloyl unit in TA provides multiple adjacent phenolic –OH sites that can coordinate with Fe^{3+}, generating dense, crosslinked supramolecular networks via Fe–O coordination bonds. [8,13,14] When $FeCl_3$ interacts with TA, the coordinated Fe-TA structure combines a carbon-rich polyphenolic backbone with uniformly dispersed iron species. During pyrolysis, these well-distributed iron centers act as in situ catalysts that lower the onset temperature of thermal decomposition and promote graphitization at elevated temperatures. [8,13,14] This dual catalytic effect of Fe with TA yields highly conductive carbons with a homogeneous surface morphology and tailored porosity, making them promising materials for energy storage applications.

3.2. Experimental section

3.2.1. Preparation of high-resolution 3D-printed Elegoo sample

All high-resolution 3D-printed Elegoo samples were prepared by Philip Onffroy, DeSimone's Lab (Stanford). Continuous liquid interface production (CLIP) vat photopolymerization of microstructures was conducted using a pre-commercial high-resolution Carbon S2 printer with 5.4 μm pixel size. The geometry of the high-resolution diameter octet lattice disks was designed with 30 μm-diameter struts and 300 μm^3 unit cells using

nTop and printed on the Carbon S2 printer. The commercially available resin used was acrylate-based photo-curable resin (Elegoo, translucent standard photopolymer resin).

3.2.2. Preparation of tannic acid (TA)/$FeCl_3$ soaking solution

All high-resolution 3D-printed Elegoo samples received from DeSimone's Lab (Stanford) were first soaked in ethanol for 12 h to remove any uncured resin prior to $FeCl_3$-TA impregnation. To prepare the $FeCl_3$–TA soaking solution, stock solutions of $FeCl_3$ and TA were prepared separately, then mixed by adding the TA stock solution dropwise to the $FeCl_3$ stock solution while stirring continuously. This approach promotes the formation of a homogeneous tannic acid–Fe complex and helps prevent rapid precipitation or gel aggregation. Continuous stirring also facilitates rapid dispersion of freshly added TA throughout the bulk solution, allowing it to react evenly with Fe^{3+} rather than forming localized aggregation. This controlled mixing procedure is particularly important for TA–$FeCl_3$ systems, because the metal–phenol interaction occurs rapidly and can otherwise lead to nonuniform complexation.

The samples were first sonicated at 80 Hz for 30 min during soaking to facilitate infiltration of the solution into the hierarchical architecture, remove trapped air, and promote uniform distribution of chemical species throughout the internal surfaces. To prevent light-induced oxidation of tannic acid, both the samples and the soaking solutions were wrapped in aluminum foil during soaking. Tannic acid is thermodynamically stable in water and in neutral to slightly acidic aqueous solution at room temperature; it does not rapidly hydrolyze or decompose, and solutions can remain clear and usable for days to weeks. However, its polyphenolic structure is intrinsically redox-active; it is an excellent electron donor and can absorb UV or near-UV light, reach its excited state, and be oxidized by dissolved O_2. After soaking for 48 h, the samples were removed, wrapped in coffee filter paper, and centrifuged in a household salad spinner for 1 min to remove excess solution trapped in the fine inter-strut spaces of the high-resolution hierarchical structure. If the residual Fe–TA solution trapped between the struts is not fully removed, it can form an unwanted carbonaceous film that bridges adjacent struts, leading to inaccurate char-yield estimation and reduced electrolyte and ion accessibility during subsequent electrochemical measurements.

3.2.3. Pyrolysis procedure

The pyrolysis process was conducted in an Atomate three-zone furnace with feedback loop control of temperature, flow rate, and pressure. The temperature first increased from room temperature to 120 °C at 5 °C/min, then to 200 °C at 1 °C/min, and to 300 °C at 0.5 °C/min. The sample was then held isothermally at 300 °C for 1 h to minimize the volatile mass loss and prevent structural deformation. Subsequently, the temperature increased to 550 °C at 1 °C/min, and further to 900 °C at 2 °C/min. The final temperature of 900 °C was maintained for 2 h to complete the pyrolysis. Continuous argon flow ensured an inert environment during pyrolysis and cooling.

3.2.4. Carbon nanotubes growing mechanism

CNT growth on 3D pyrolytic carbon electrodes was performed in a quartz tube via chemical vapor deposition (CVD). For CNT synthesis, copper and nickel catalysts were alternately deposited via soaking in solutions of 25 mM $CuSO_4$ and 50 mM $NiNO_3$ for 12 h. To improve the wettability of the pyrolytic carbon, the 3D carbon sample was first dipped in ethanol, then rinsed with DI water to remove residual ethanol, before being soaked in the catalyst aqueous solution. To ensure that no gas bubbles were trapped in the high-resolution sample's voids, the soaked sample was degassed in the vacuum oven for the first 30 minutes and then sonicated for 30 minutes at 80 Hz. The catalyst-coated 3D carbon was dried in a vacuum oven at 100 ^oC and then moved to a CVD furnace. Samples were heated with Ar/H_2 carrier gas and held at 650°C for 20 minutes to form Ni/Cu nanoparticles. Then, CNT growth was carried out at 725°C under an ethylene flow for 20 minutes. After CVD CNT growth, CNT growth samples were acid-leached with 2 M HNO_3 at 80 °C for 24 hours to remove any residual catalysts and amorphous carbon.

3.2.5. Material characterization

Optical microscopy (OM; Keyence Digital Microscope VHX-X1F) and scanning electron microscopy (SEM; Zeiss Gemini 500 SEM) were used to inspect the samples and measure strut diameter before and after catalyst coating and pyrolysis. Scanning electron microscopy with energy-dispersive X-ray spectroscopy (SEM-EDS; Thermo Fisher Phenom XL Desktop SEM) was used to analyze elemental distributions in the cross-sections of carbonized samples. All electrochemical measurements were done by a Biologic VSP-3e potentiostat in combination with the EC-Lab program version 11.61. All data plotting and organization were performed using OriginPro 2023b.

3.2.6. Data analysis of Electrochemical data

3.2.6.1. Unit cell size, unit cell area, and strut size calculation

ImageJ software was used to quantitatively analyze the SEM images and measure the unit cell size, strut diameter, and unit cell area of the pyrolytic 3D-printed carbon lattices. First, the ImageJ software was calibrated using the scale bars in the SEM images, and then the relevant features were manually identified for measurement. **Figure 3.1** shows that the unit cell size was determined by measuring the spacing between adjacent lattice nodes in the octet structure at eight locations and averaging the results. The strut size was determined by measuring the two thickest and two thinnest regions of each carbon strut and averaging them. For each sample, we measured the strut size on three struts and averaged these values to obtain the sample's mean strut size. In addition, the unit cell area was calculated from eight lattice units and averaged. This SEM image-based dimensional analysis provided a reliable method for analyzing dimensional retention and structural changes before and after pyrolysis, enabling direct comparison between untreated and Fe-TA-infiltrated samples.

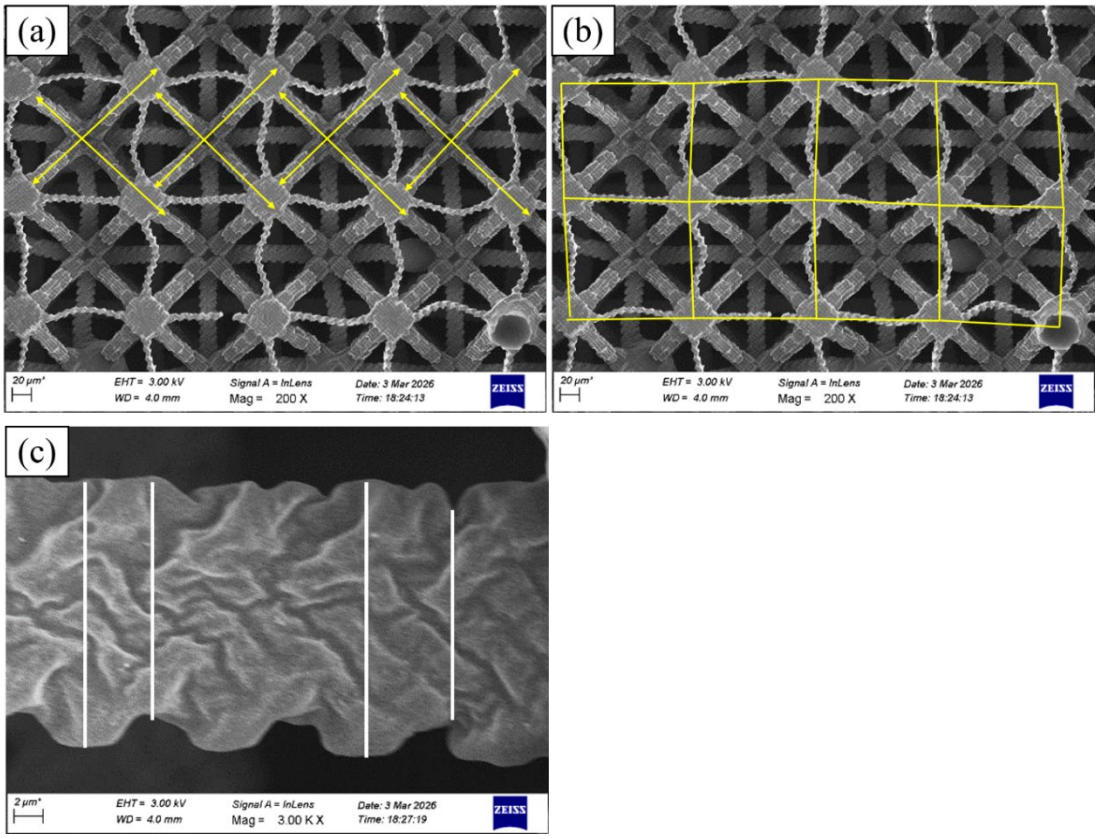


Figure 3.2. (a) ImageJ measurement of eight different unit cell sizes from an SEM image, (b) ImageJ measurement of 8 different unit cell areas, (c) ImageJ measurement of strut size by measuring two thickest and two thinnest regions of each carbon strut.

3.2.6.2. Capacitance calculation from GCD

The electrochemical measurements were performed using a Biologic VSP-3e potentiostat in combination with the EC-Lab program version 11.61. An electrochemical cell (approximately 50 mL in volume) was employed with a saturated calomel electrode (SCE) as the reference electrode, a graphite rod as the counter electrode, and the 3D carbon sample as the working electrode.

For symmetric galvanostatic charge and discharge (GCD) behavior, the charge and voltage ratio remains the same over the entire charge and discharge process; the capacitance(C), and the energy density are [32,33] (indicating all variables)

$$C = \frac{I\,\Delta t}{\Delta V}\,, E = \frac{CV^2}{2}$$

where C is the capacitance, I is the current (A), Δt is the discharge time (s), ΔV is the potential window, and E is energy density.

However, the galvanostatic charge–discharge profiles of our 3D carbon samples are asymmetric, indicating non-ideal capacitive behavior and the presence of quasi-reversible faradaic processes attributable to the PDAN coating. Therefore, the capacitance should be determined by the integral method from the discharge curve rather than by using the conventional linear approximation. The capacitance is calculated from the voltage-time integral:

$$voltage - time\ integral = \int V dt$$

For non-symmetric galvanostatic charge–discharge profiles, the charge and voltage ratio no longer remains constant; instead, it varies with time. The capacitance equation has been rewritten as [33,34]

$$C = \frac{i}{dV/dt}$$

If we rearrange the equation and multiply by (V/V), the previous equation can be integrated to give the equation:

$$C = \frac{\int i\,V\,dt}{\int_{V_i}^{V_f} V\,dV}$$

At constant current, we can take the current out of the integral and get the equation:

$$C = \frac{i\int V\,dt}{\int_{V_i}^{V_f} V\,dV}$$

$$C = \frac{i\int V\,dt}{\frac{1}{2}\Delta V^2} = \frac{2i\int V\,dt}{\Delta V^2}$$

$$C_s(specific\ capacitance) = \frac{i/m \int V\,dt}{\int_{V_i}^{V_f} V\,dV} = \frac{2i \int V\,dt}{m\,\Delta V^2}$$

$$C_a(areal\ capacitance) = \frac{i/A \int V\,dt}{\int_{V_i}^{V_f} V\,dV} = \frac{2i \int V\,dt}{A\,\Delta V^2}$$

Calculation process: take one sample in 0.5 M H_2SO_4 (potential window = 0.7V) as an example.

Table 3.2 Calculation of GCD data of 3D carbon sample tested in 0.5 M H_2SO_4.

Current density (mA/cm^2)	Potential window (ΔV)	IR drop (V)	Integrated area (Vs)	Areal capacitance (F/cm^2)
2.5	0.695	0.005	438.723	4.54
5	0.691	0.009	210.059	4.40
10	0.682	0.018	99.326	4.28
15	0.673	0.027	63.439	4.21
20	0.664	0.036	45.787	4.16
25	0.655	0.045	35.347	4.12
30	0.646	0.054	28.412	4.09
50	0.610	0.090	14.874	4.00
100	0.521	0.179	5.237	3.85
200	0.346	0.354	1.075	3.59
300	0.174	0.526	0.163	3.22

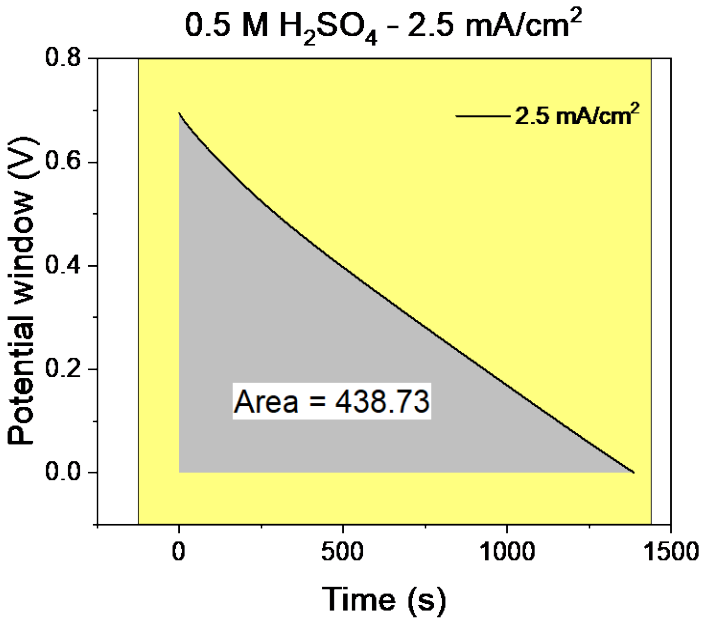


Figure 3.3 Integrated area calculation from OriginPro 2023b to calculate the area capacitance from GCD discharge curve (figures) units

3.2.6.3. Capacitance calculation from Cyclic Voltammetry (CV)

The areal capacitance C_{area} (F/cm^2) from a CV curve measured at a constant scan rate v is commonly calculated as: [32,33]

$$C_{\text{area}} = \frac{1}{v\, 2\Delta V\, A} \int_{V_1}^{V_2} I(V)\, dV$$

where $\int_{V_1}^{V_2} I(V)\, dV$ is the integrated area under the CV curve over one full cycle, v is the scan rate (mV/s), A is the area of the electrode (cm^2), and ΔV is the potential window (V) of the CV curve. A full CV scan covers a total potential range of $2\Delta V$, since the applied potential is scanned through the selected window in both the forward and reverse directions.

3.2.6.4. Carbon density calculations

For all unit cell and unit strut size measurements, we used the struts in the first layer as representative of the entire sample. However, we later observed that the strut diameter in the first layer is thinner than in subsequent layers (the 2nd- and 3rd-layer struts are closer to the initial design dimensions), resulting in different shrinkage compared to other layers. Because SEM images and dimensional data are available only for the first layer for most samples, we nonetheless used these first-layer SEM images to calculate dimensional retention and carbon density. Accordingly, we assume that the dimensional shrinkage of the first-layer struts is representative of the bulk sample. To determine whether the 3D pyrolytic carbon is hollow or solid, I used the following method to calculate its density from our sample. According to the software, we know the basic conditions of the 3D-printed polymer template:

- The 30 µm polymer sample's solid volume (volume of struts and nodes, not including the voids): 20.53 mm^3
- The 30 µm polymer sample's bulk volume (volume of struts, nodes, and voids): 178.66 mm^3
- Void fraction = (bulk bounding volume - solid volume) ÷ bulk volume = (178.66 - 20.53) ÷ 178.66 = 0.88 (88%)
- Solid fraction of 30 µm polymer sample is: 1 - 0.88 = 0.12 (12%)

Since the unit cell of our 3D-printed sample is an octet-truss (shown in **Figure 3.4**), one octet-truss contains 36 struts in total. However, when considering a single repeating unit cell, we account for how those struts are shared with neighboring cells. A standard octet unit cell contains 24 full-strut volumes within its boundaries.

Assuming the struts are cylinders: $V_{strut}(volume\ of\ each\ strut) = \pi r^2 L = \pi r^2 \frac{\sqrt{2}}{4} a$

Total volume of struts (ignoring node overlaps for simplicity): $V_s \sim 24 \times \pi r^2 \frac{\sqrt{2}}{4} a = 6\sqrt{2}\pi r^2 a$

The solid volume of the 3D structure after pyrolysis can be calculated from the dimensional retention of unit cell size (a) and strut size (r) before and after pyrolysis with the initial solid volume of the 3D polymer.

$$V_s\ (after\ pyrolysis)\ = V_s \times \left(\frac{r_{pyrolysis}}{r_{initial}}\right)^2 \left(\frac{a_{pyrolysis}}{a_{initial}}\right)$$

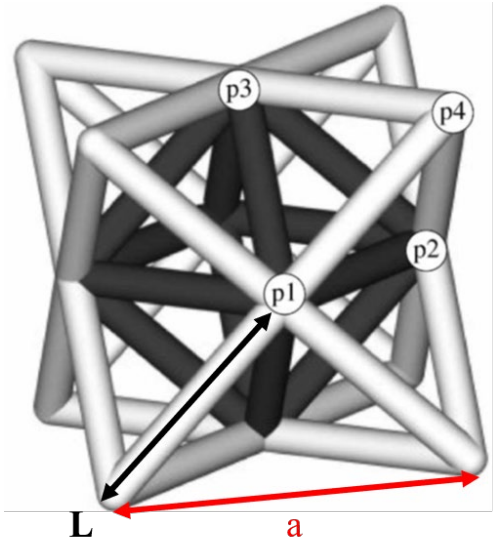


Figure 3.4 Octet-truss unit cell, a is the unit cell size, and L is the strut length.

3.3. Results and discussion

3.3.1. Selection of Elegoo resin

In **Chapter 2**, we used PR48, a standard clear acrylate-based photopolymer used in SLA/DLP 3D printing for high-resolution templates. However, PR48 exhibits significant shrinkage during pyrolysis, yielding only 4.7 wt% of carbon at 800 °C and up to ~95% volume shrinkage. In comparison, the commercial Elegoo Translucent resin, which contains bisphenol A epoxy diacrylate, exhibits a much higher pyrolysis yield of approximately 9.3 wt% at 800 °C, as confirmed by thermogravimetric analysis (**Figure 3.5.a**), while

maintaining high printing speed and resolution. Pyrolysis of PR48 and Elegoo samples printed with 30 µm strut diameters, following a previously reported protocol, demonstrated the Elegoo-derived structures underwent significantly less dimensional shrinkage than those from PR48(**Figure 3.5.b**). The superior dimensional retention and mechanical robustness of the Elegoo-derived carbon therefore motivated its selection as the base polymer for carbon production in this study.

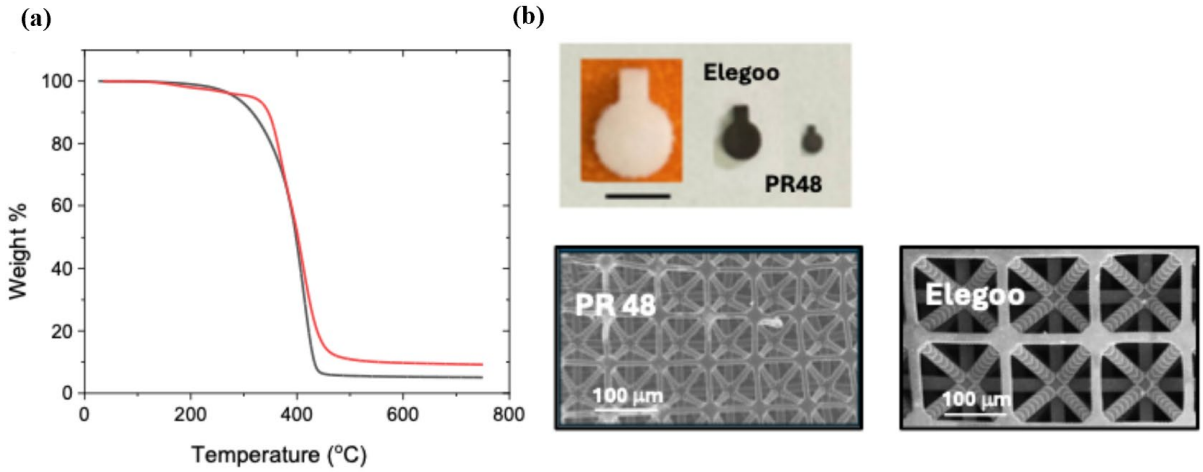


Figure 3.5 (a) Thermogravimetric analysis (TGA) of Elegoo and PR48 octet lattices with as-printed 50 µm struts and 500 µm unit cell size under typical inert pyrolysis conditions; **(b)** (i) photographs of the original polymer template (left), the resulting pyrolyzed product (Elegoo, middle), and the resulting pyrolyzed product (PR48, right) using 50 µm strut size, 500 µm unit cell size polymer templates, and (ii) scanning electron microscopy (SEM) images of the corresponding 3D pyrolytic carbon structures.

3.3.2. Effects of $FeCl_3$ and tannic acid (TA) infiltration

Herein, I present a post-printing, pre-pyrolysis treatment that enhances the electrochemical surface area and electrical conductivity of 3D carbon architectures derived from Elegoo samples. This approach improves carbon yield, mitigates structural shrinkage, and promotes graphitization during pyrolysis by using $FeCl_3$ as a multifunctional catalyst and tannic acid as an additional carbon precursor. As discussed in section 2, $FeCl_3$ serves two key roles: first, it facilitates polymer decomposition at lower temperatures, initiating degradation earlier than in untreated polymers. Second, it promotes graphitization during the high-temperature stages of pyrolysis, consistent with previous findings in section 2. Tannic acid (TA), a naturally derived polyphenolic carbon precursor, was infused into the 3D-printed polymer templates alongside Fe before pyrolysis to further improve structural integrity and char yield. The catechol groups in TA readily chelate transition-metal ions such as Fe^{3+}, inducing crosslinking that significantly enhances carbonization yield. [35,36]

To investigate the effect of tannic acid, thermogravimetric analysis was performed on pure PR48, pure Elegoo, and a 0.1 M tannic acid-soaked Elegoo sample for 48 h. As shown in **Figure 3.6**, the TA-infiltrated Elegoo sample shows a 15 wt% char yield, a 61% increase, compared to the pure Elegoo sample, indicating the effect of tannic acid. Tannic acid is a multifunctional polyphenol with many aromatic rings and hydroxyl groups; when it is absorbed onto the Elegoo matrix, it increases the ratio of aromatic carbon that survives devolatilization and promotes thermal crosslinking/condensation reactions that favor formation of a thermally stable, carbon-rich char rather than volatile fragments. In summary, TA serves as an effective carbon precursor additive, shifting thermal decomposition pathways from volatiles and toward solid carbonaceous products, leading to improved char yield and mechanical integrity.

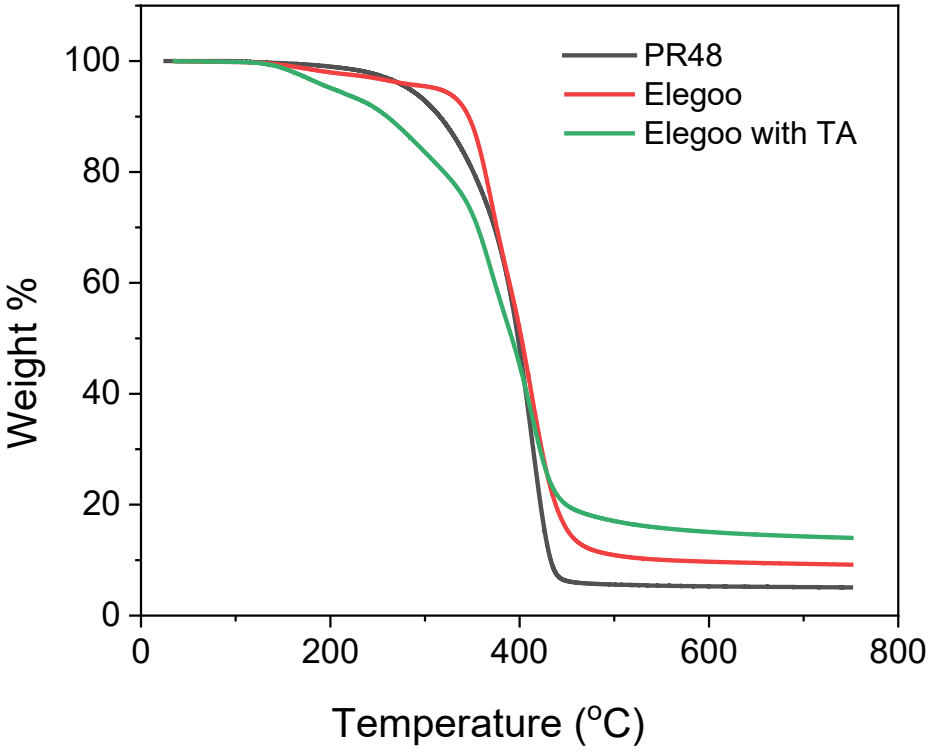


Figure 3.6 Thermogravimetric analysis (TGA) of pure PR48, pure Elegoo and TA-infiltrated Elegoo octet lattices with as-printed 50 µm struts and 500 µm unit cell size under typical inert pyrolysis conditions.

3.3.3. Different feature size effect

The initial sample feature size plays a critical role in char yield and dimensional retention. **Table 3.3** shows char yields of 3D-printed Elegoo samples with and without Fe-TA infiltration with different strut sizes. Higher-resolution samples exhibit larger surface-to-volume ratios, which facilitate the escape of volatile carbon-containing species during pyrolysis, thereby lowering char yield and increasing shrinkage. At the same time, the penetration depth of the soaking solution into the Elegoo template is limited, so smaller struts allow the TA and Fe catalyst to permeate more effectively throughout the structure. As a result, smaller feature size enables more effective permeation of the Fe/TA solution throughout the 3D architecture, as reflected by the char yield of 29~32 wt% for the 30 µm features, compared with only 15~16 wt% for the 200 µm features.

Table 3.3 Char yield of 3D polymer pyrolyzed at 850 °C

Elegoo	Untreated sample	0.08 M $FeCl_3$ + 0.08 M tannic acid
Elegoo-30 µm	7.8 wt%	29 ~ 32 wt% (3 samples)
Elegoo-50 µm	9.3 wt%	23 ~ 25 wt% (3 samples)
Elegoo-200 µm	9.5 wt%	15 ~ 16 wt% (3 samples)

3.3.4. Effects of $FeCl_3$/TA infiltration on char yield, dimensional retention and surface morphology

Figure 3.7 presents the scanning electron microscopy (SEM) images of 3D carbon lattices derived from 3D-printed Elegoo after pyrolysis, comparing samples with and without Fe–TA infiltration at different magnifications. The untreated control sample exhibits significant shrinkage, with a reduced strut diameter of 8.97 μm and a cell size of 114.42 μm. In contrast, with Fe-TA infiltration, the diameter of the carbon strut after pyrolysis becomes 13.20 um, and the cell size becomes 172.6 um. The strut diameter retention improves from 43% to 81.4%, while cell size retention increases from 44.6% to 68.5% with the Fe-TA infiltration treatment (**Table 3.4**). This enhanced dimensional retention can be attributed to the synergistic effects of tannic acid (TA) and Fe^{3+} during pyrolysis. This Fe–TA coordination chemical structure suppresses both excessive scission of polymer chains and mass loss during low-temperature thermal decomposition. Moreover, Fe^{3+} promotes the formation of graphitic carbon at higher temperatures. Together, these effects lead to improved material retention and preservation of the original lattice geometry after pyrolysis. F**igure 3.7 (d**) shows the untreated carbon strut with a relatively smooth and uniform surface, whereas **Figure 3.7 (h)** clearly demonstrates that Fe–TA infiltration produces a much rougher and more wrinkled morphology. In the Fe–TA-treated sample, the strut surface is decorated with abundant nanoscale thorn-like features, giving the carbon a more textured appearance compared with the featureless control sample (**Figure 3.8**). As a result, the Fe–TA sample exhibits a hierarchical surface morphology that can increase the accessible surface area and potentially benefit electrochemical performance.

Table 3.4. Char yield and dimensional retention of control sample and Fe-TA-soaked sample after pyrolysis at 900ºC

	Char yield (%)	Diameter (%)	Thickness (%)	Area (%)	Volume (%)	Strut size (%)	Cell size (%)
Control	7.8	40.9	40.4	16.7	6.8	43.0	44.6
Fe-TA	30.0	63.5	76.2	40.3	30.7	81.4	68.5

The electrochemical performance of the control and Fe-TA-treated 3D carbon samples was measured using half-cell tests in three-electrode beaker cells. **Figure 3.9(a)** presents the cyclic voltammetry (CV) curves of the control sample and Fe-TA infiltration sample at 5 mV/s; the areal capacitance increased from 1.95 F/cm^2 to 4.88 F/cm^2 at 5 mV/s, a 2.5-fold improvement. **Figure 3.9(b)** shows the discharge curve of the galvanostatic charge–discharge (GCD) profiles of the control and Fe-TA-treated samples. Compared with the control sample, the Fe-TA-infiltrated sample exhibits a longer discharge time, confirming a higher charge-storage capacity and improved electrochemical performance, consistent with its enhanced specific surface area, as evidenced by increased surface roughness shown in **Figure 3.8**. The more gradual voltage decay of the Fe-TA-infiltrated sample also suggests lower internal resistance and better charge transport. The Fe-TA-infiltrated sample exhibits higher areal capacitances of 4.74, 4.76, 4.81, 4.90, and 5.07 F/cm^2 at 30, 20, 15, 10, and 5 mA/cm^2, respectively, which are considerably higher than those of the untreated control sample. (Shown in **Figure 3.9.c** and **Table 3.5**)

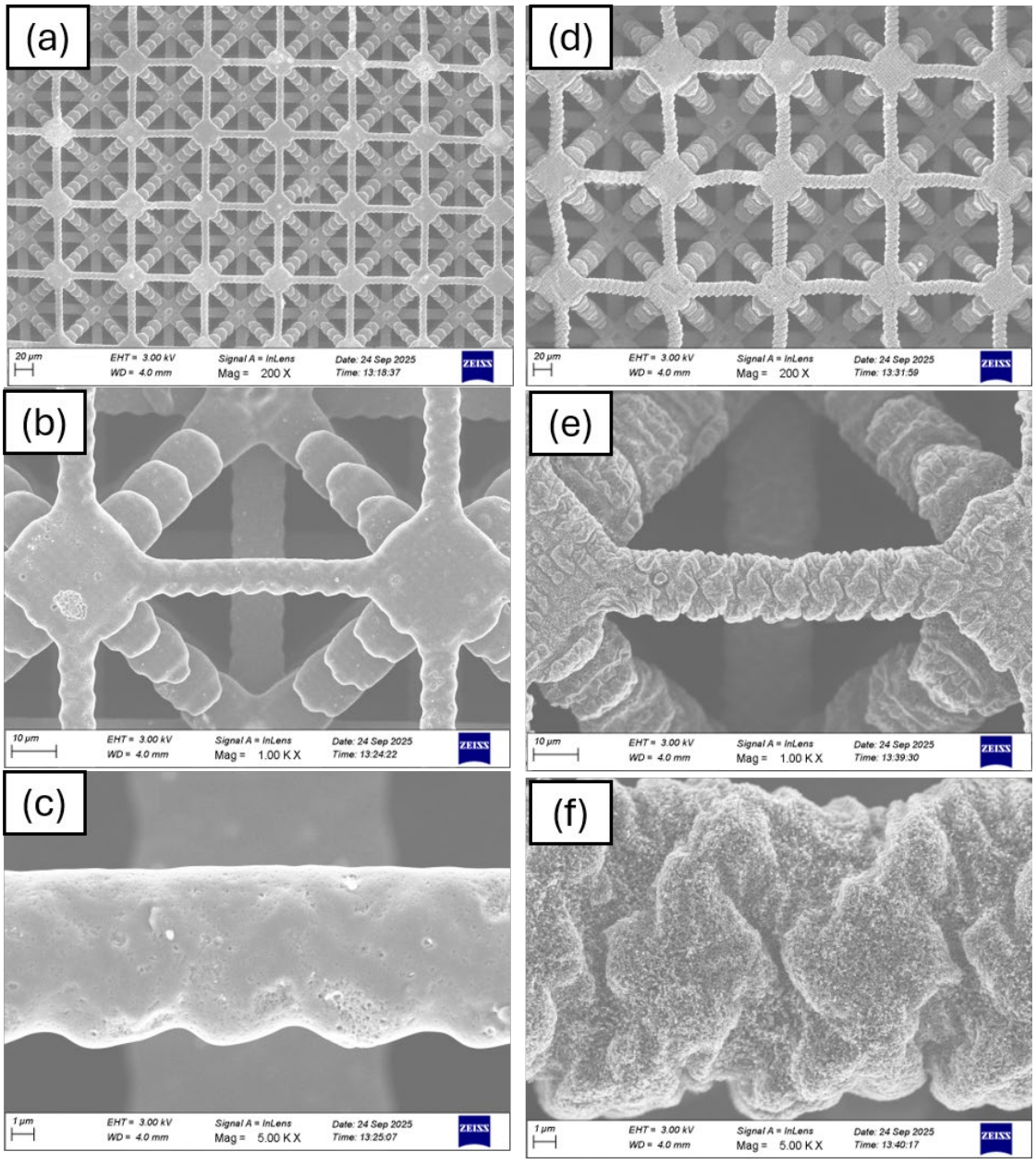


Figure 3.7. SEM images of 3D carbon lattice derived from 3D printed Elegoo after pyrolysis at 900ºC without $FeCl_3$ and tannic acid soaking (a, b, c,) and with 0.08 M $FeCl_3$ + 0.08 M tannic acid soaking (d, e, f). (Bigger picture)

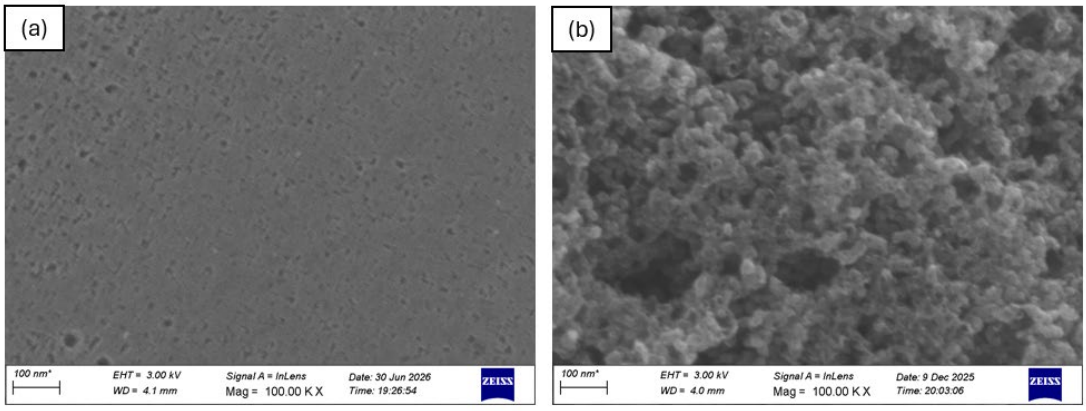


Figure 3.8. SEM images of 3D carbon lattice derived from 3D printed Elegoo after pyrolysis at 900ºC without $FeCl_3$ and tannic acid soaking (a) and with $FeCl_3$ and tannic acid soaking (b) at 100000 X magnification.

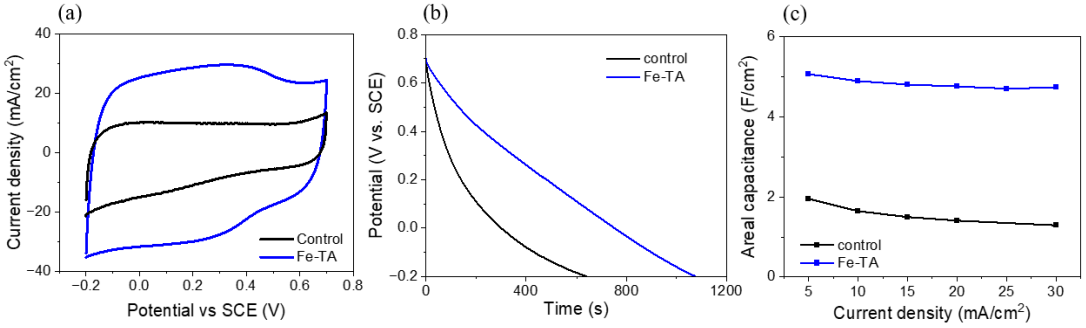


Figure 3.9. (a) Cyclic voltammetry of control and Fe-TA infiltration samples at 5 mV/s in 0.5 M H_2SO_4, (b) GCD discharge curve of control and Fe-TA samples at 5 mA/cm^2 in 0.5 M H_2SO_4, (c) summarized areal capacitance of control and Fe-TA treated samples (For each condition, we prepared three samples, all of which exhibited the same trend.)

Table 3.5 Areal capacitance calculated from GCD measurement of high-resolution carbonized Elegoo samples in 0.5 M H_2SO_4 with SCE as reference electrode, and graphite rod as counter electrode.

	30 mA/cm^2	**20 mA/cm^2**	**15 mA/cm^2**	**10 mA/cm^2**	**5 mA/cm^2**
Control	1.29 F/cm^2	1.41 F/cm^2	1.50 F/cm^2	1.65 F/cm^2	1.95 F/cm^2
Fe: TA=1:1	4.74 F/cm^2	4.76 F/cm^2	4.81 F/cm^2	4.90 F/cm^2	5.07 F/cm^2

3.3.5. Different Fe and tannic acid ratios to determine the best performance

The concentration of the Fe/TA soaking solution significantly affects the final carbon structure, surface morphology, and electrochemical performance. As the TA concentration increases, the char yield generally rises because more high-yield polyphenolic precursor is introduced into the 3D template. However, when the TA concentration becomes too high, the viscosity of the soaking solution increases, hindering penetration into the Elegoo template. Under these conditions, Fe and TA tend to remain near the outer surface rather than infiltrating the interior, resulting in nonuniform carbon formation and reduced internal utilization. In addition, the high viscosity of the soaking solution can cause severe clogging during the spin-drying process, especially for high-resolution 3D-printed samples.

In contrast, when the Fe concentration is too high relative to TA, the limited amount of tannic acid cannot fully coordinate with the excess Fe ions, leading to a lower char yield and the formation of hollow structures after pyrolysis, which is similar to the non-tannic acid introduction situation as discussed in **Chapter 2**. This significantly reduces mechanical integrity. Only at an optimal Fe/TA concentration can the precursor solution effectively infiltrate the template, producing a rough surface uniformly covered with carbon nanothorns (**Figure 3.8**), thereby providing the highest accessible surface area and, consequently, the greatest areal capacitance. In the experiments, a Fe/TA ratio of 1:1, using both $FeCl_3$ and tannic acid at 0.08 M, gave the best performance. As shown in **Figure 3.10**, the Fe/TA = 1:1 sample exhibits the highest areal capacitance, reaching 4.62 F/cm^2 at 20 mV/s and 5.98 F/cm^2 at 5 mV/s, whereas the Fe/TA = 2:1 sample delivers 2.85 and 3.59 F/cm^2 at 20 and 5 mV/s, respectively, and the control sample shows the lowest values. The influence of the Fe/TA molar ratio in the soaking solution on the electrochemical properties of the pyrolyzed polymer samples by Electrochemical Impedance Spectroscopy (EIS). As shown in **Figure 3.10 (c)**, both Fe/TA-soaked samples demonstrate a significant reduction in high-frequency Rs compared to the pristine control sample; this is due to the catalytic effects of Fe, which can transform the pyrolytic carbon into a more conductive graphitic/glassy carbon structure. Increasing the iron content from $1:1$ to $2:1$results in a progressive shift of the high-frequency intercept toward lower values, indicating reduced bulk resistance. The $\mathrm{Fe:TA} = 2:1$ sample shows the lowest $R_s(\approx 3.3\ \Omega)$, followed by $\mathrm{Fe:TA} = 1:1(\approx 4.2\ \Omega)$ and the control ($\approx 7.3\ \Omega$).

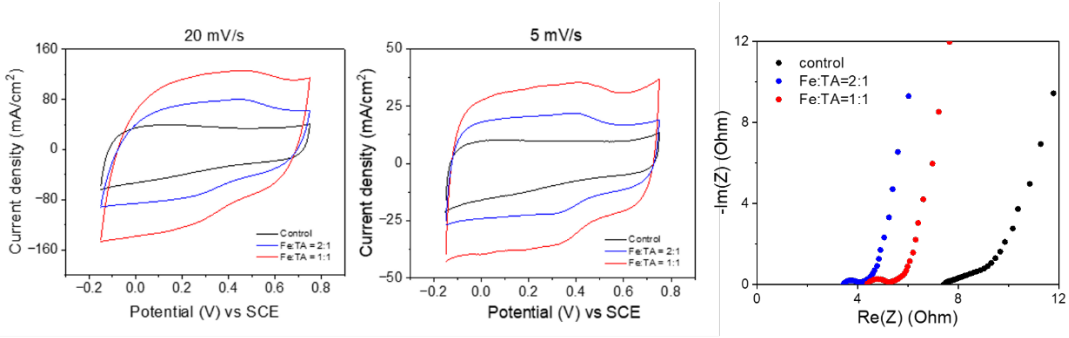


Figure 3.10. Cyclic voltammetry of control and Fe-TA infiltrated sample with different Fe/TA ratio at (a) 20 mV/s, (b) 5 mV/s. (c) Nyquist plot of control and Fe-TA infiltrated sample with different Fe/TA ratio. (Each condition was reproduced by 3 times, and all of them followed the same trend)

In **Figure 3.11**, SEM images of the pyrolyzed 3D-printed carbon show that the untreated control (a, b) has a smoother and thinner strut structure, whereas Fe–TA infiltration (c, d) and (e, f) produces significantly thicker and rougher struts. The increased thickness likely results from penetration and subsequent thermal conversion of the Fe–TA complex within the precursor network, leading to the buildup of carbon/metal residues during pyrolysis. The roughened surface results from uneven shrinkage, gas evolution from decomposition, and Fe-assisted texture of the carbon framework.

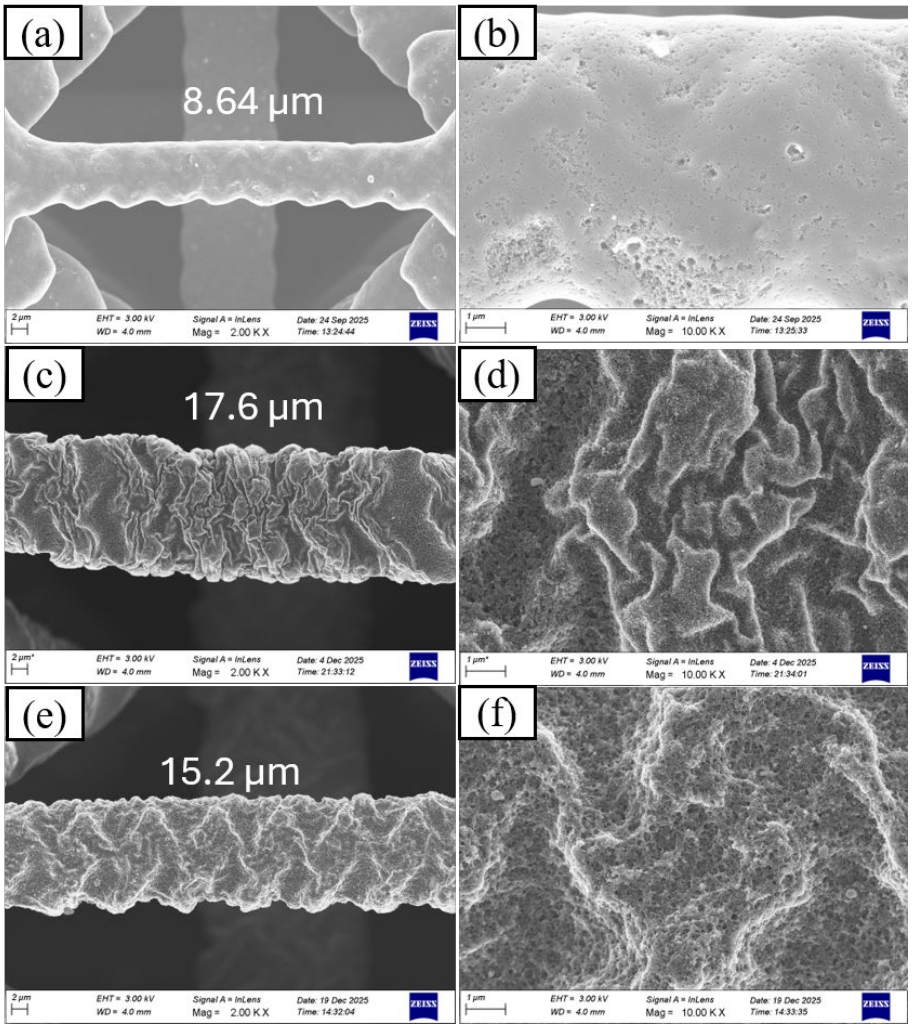


Figure 3.11 SEM images of 3D pyrolytic carbon derived from a high-resolution 3D-printed Elegoo sample after pyrolysis (a, b) control sample without any treatment, (c, d) Fe: TA=2:1 soaking, and (e, f) Fe: TA=1:1 at 2000X and 10000X magnification.

3.3.6. Carbon nanotube growth on 3D Fe-TA infiltrated samples for enhanced areal capacitance and electromagnetic interference shielding

3.3.6.1. Enhanced areal capacitance

To achieve higher areal capacitance by increasing the electrochemically active specific surface area, carbon nanotubes (CNTs) were grown via chemical vapor deposition on both control 3D-printed carbon scaffolds and on Fe–TA-infiltrated scaffolds. In the control samples, CNT growth was markedly non-uniform and sparse (**Figure 3.12**), which can be attributed to two interrelated factors. First, the control scaffolds possess a relatively smooth surface with limited chemical functionality and roughness (shown in **Figure 3.8**), providing insufficient anchoring sites for the deposited metal catalyst nanoparticles; as a result, the catalyst particles are weakly bound and can be moved or even removed by the flowing reaction gases during the high-temperature CVD process, leading to local depletion of active growth sites and heterogeneous CNT nucleation. Second, the control samples exhibit much smaller feature sizes and a more compact pore structure, which impedes the diffusion and penetration of the carbon precursor gas (e.g., ethylene) and carrier gases

throughout the interior of the scaffold; this mass-transport limitation restricts CNT growth predominantly to the outer surfaces and near-surface regions, further exacerbating spatial non-uniformity.

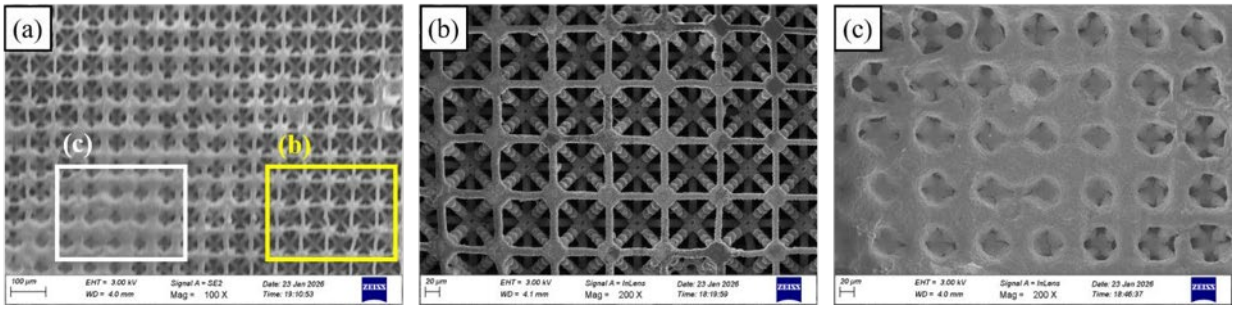


Figure 3.12. SEM images of a 50 µm control sample after CNT (a) at 100 X, (b) loose CNT growth region at 200 X, (c) dense CNT growth region at 200X.

In contrast, the Fe–TA-infiltrated samples display a significantly different surface morphology (shown in **Figure 3.8**): the Fe–TA-infiltrated sample forms well-dispersed, strongly anchored Ni and Cu nanoparticles on a rough carbon matrix. This Fe-TA-infiltrated scaffold provides abundant nucleation sites, improved catalyst stability against gas-flow-induced detachment, and enhanced gas accessibility due to its more open, interconnected pore network, thereby enabling uniform, dense CNT growth throughout the 3D carbon structure. (**Figure 3.13**) Consequently, the Fe–TA-infiltrated, CNT-decorated electrodes offer a substantially higher specific surface area and a more favorable hierarchical architecture for ion transport, which is expected to translate into significantly improved areal capacitance after CNT growth.

After CNT growth, the 50 µm 3D carbon electrode shows a clear increase in areal capacitance from 1.22 F/cm^2 to 3.85 F/cm^2 (**Figure 3.14.a**), as evidenced by the much larger CV area and higher current response compared with the pristine carbon scaffold. This improvement can be explained by the CNT layer creating a more hierarchical and electrochemically accessible surface, thereby increasing the effective surface area, exposing more active sites to the electrolyte, and shortening ion transport pathways within the porous structure. In addition, the CNT network improves electrical connectivity between the carbon framework and the current collector, enabling electrons to flow more efficiently through the electrode during charging and discharging. The EIS results support this interpretation (**Figure 3.14.b**): the decrease in solution resistance (Rs) after CNT growth indicates improved charge transport and reduced overall ohmic loss, likely because the CNTs form conductive bridges, enhance interparticle contact, and reduce contact resistance at the electrode/electrolyte interface. Together, these structural and electrical improvements lead to faster ion and electron transfer, thereby increasing areal capacitance after CNT growth.

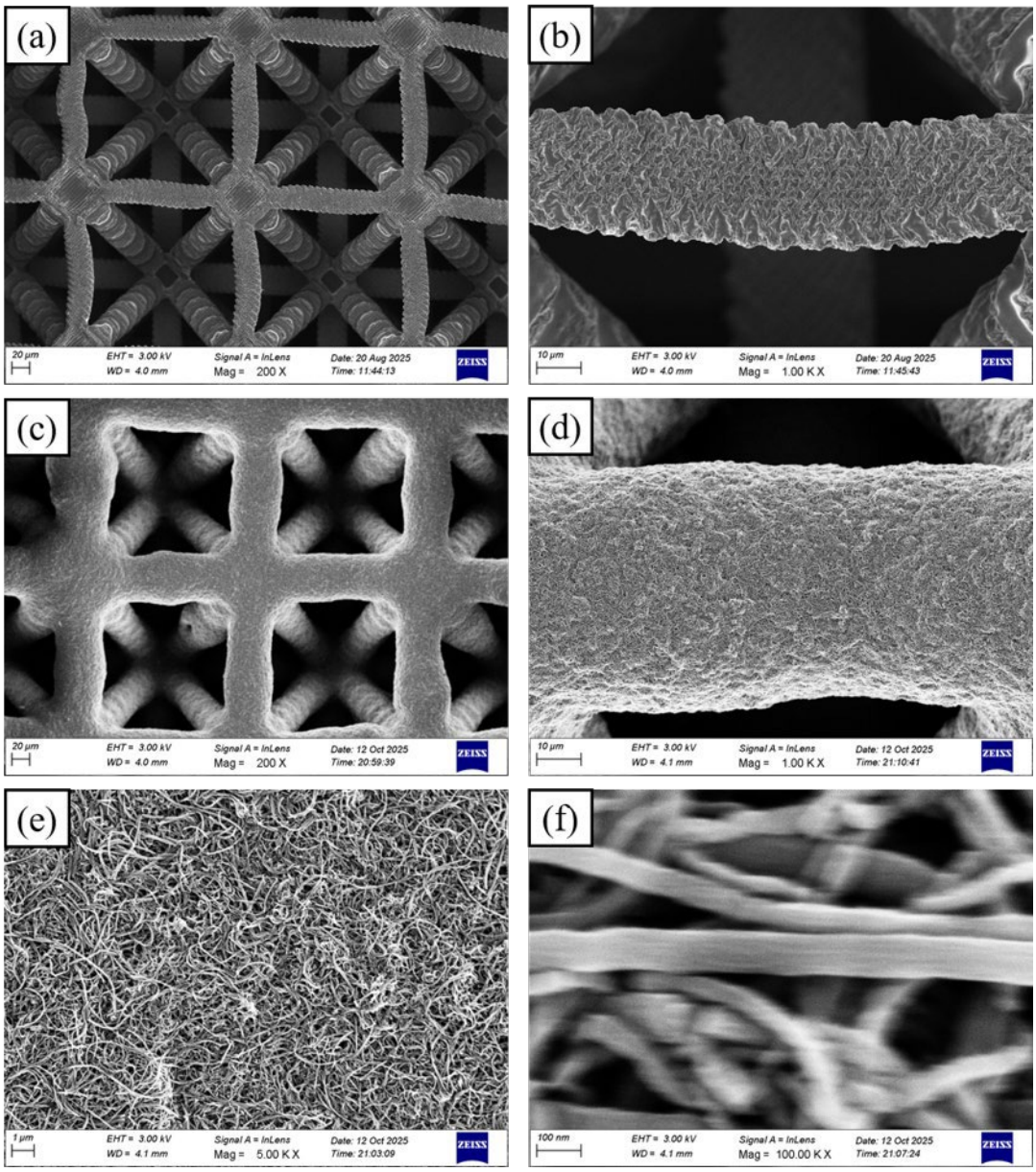


Figure 3.13. SEM images of pyrolytic 50 µm Elegoo before CNT growth at (a) 200 X, (b) 1000 X, SEM images of pyrolytic 50 µm Elegoo after CNT growth at (c) 200 X, (d) 1000 X, (e) 5000 X, and (f) 100000 X.

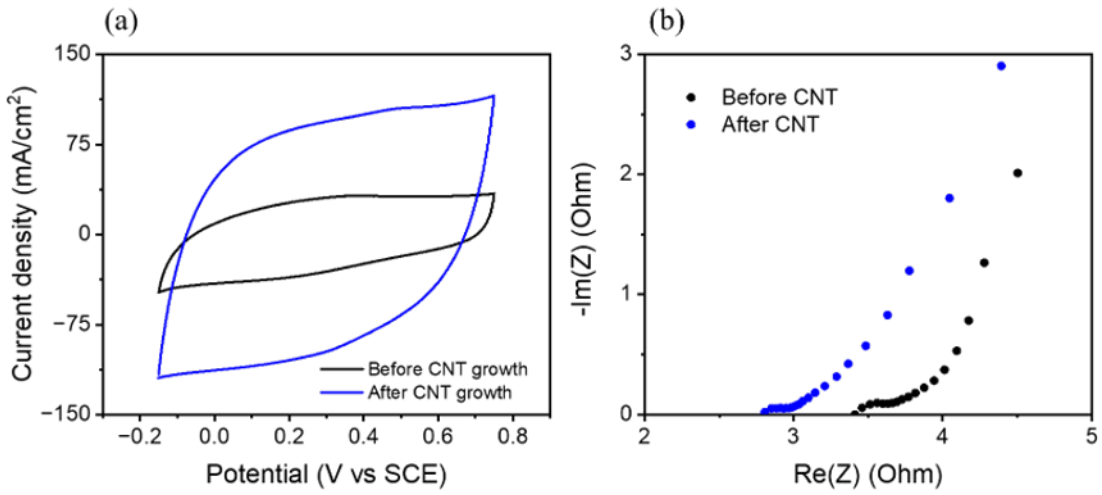


Figure 3.14 (a) Cyclic voltammetry of 50 µm Fe-TA infiltrated Elegoo sample before and after CNT growth at 20 mV/s in 0.5 M H_2SO_4, (b) Nyquist plot of 50 µm Elegoo before and after CNT growth in 0.5 M H_2SO_4

3.3.6.2. Electromagnetic interference (EMI) shielding

EMI shielding is essential in modern electronics because it can protect sensitive devices and systems from unwanted electromagnetic noise. It has been widely used in consumer electronics such as cellphones, laptops, and wearables, as well as in more demanding sectors including telecommunications, automotive electronics, medical devices, aerospace, and satellite systems, where stable operation and safety are extremely important. [37–40] In these applications, shielding materials can reflect electromagnetic waves or absorb and dissipate them, helping to maintain signal integrity and prevent devices from interfering with each other. Because CNTs are lightweight, highly conductive, flexible, and can form conductive networks at low loading, they are attractive alternatives to traditional metal shields, especially for thin, flexible, and low-mass applications.

Electromagnetic shielding is the process of reducing the penetration of electromagnetic (EM) waves into a protected region by interposing a barrier made of conductive and/or lossy materials. EMI can interrupt, degrade, obstruct, or limit the effective performance or operation of electronic instruments and systems. In shielding materials, EMI attenuation arises from three principal mechanisms: reflection, absorption, and multiple internal reflections (Figure 3.15). [41] The EMI mechanism is commonly described in terms of three contributions: reflection loss (SE_R), absorption loss (SE_A), and multiple internal reflection loss (SE_M), such that $SE_{\text{total}} = SE_R + SE_A + SE_M$.[40] Reflection is the primary mechanism in EMI shielding of highly conductive materials. The reflection mechanism requires mobile charge carriers (electrons and holes) that interact with the incident EM radiation, creating an impedance mismatch between free space and the material. As conductivity increases, the shield's reflectivity generally increases, thereby enhancing the reflection component of EMI shielding. [41] Absorption is the secondary mechanism and depends on the presence of electric or magnetic dipoles that can be coupled to the EM field and dissipate its energy as heat. Absorption loss increases with material thickness and is enhanced by high dielectric constants (which provide electric dipoles) and high magnetic permeability (which provide magnetic dipoles). [41] Materials engineered with substantial dielectric and/or magnetic loss therefore exhibit stronger absorption-type shielding. The third mechanism is multiple internal reflections, which occur at interfaces within materials, such as phase boundaries in composites, porous structures, or layered architectures with large specific internal surface areas. [41] This mechanism can either enhance or reduce the net shielding, depending on the balance between additional scattering/absorption and re-radiation.

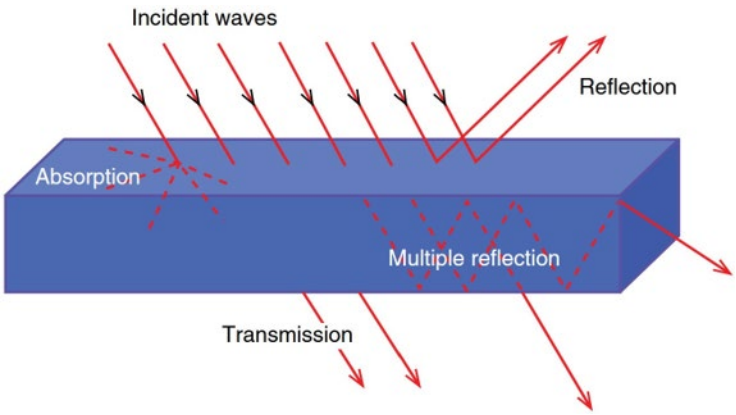


Figure 3.15. Schematic representation showing the mechanism of electromagnetic shielding. [41]

I also generated clustered CNTs on a silicon carbide sample obtained from the University of Padova (**Figure 3.16**). These clustered CNTs can be used for electromagnetic interference (EMI) materials. Carbon nanotubes (CNTs) have emerged as highly effective materials for microwave shielding owing to their exceptional electrical conductivity, large aspect ratio, and tunable dielectric properties.

Carbon nanotubes (CNTs) contribute significantly to EMI shielding through multiple internal reflections arising from their high aspect ratio, porous network formation, and intrinsic electrical conductivity. [37,39– 41] When electromagnetic waves penetrate CNTs, the interconnected pathways and voids create numerous interfaces that repeatedly scatter and reflect the incident radiation between the CNTs. This extended propagation pathway increases the probability of energy dissipation via ohmic (conduction) losses and polarization effects (dielectric losses), particularly interfacial and dipolar polarizations associated with defects and functional groups on CNT surfaces. In hierarchical and 3D architectures, tortuous geometry further improves internal reflections, efficiently trapping electromagnetic waves and promoting attenuation. As a result, CNT networks not only provide conductive attenuation mechanisms but also act as efficient scattering centers, making them really effective for EMI shielding applications. [37–39]

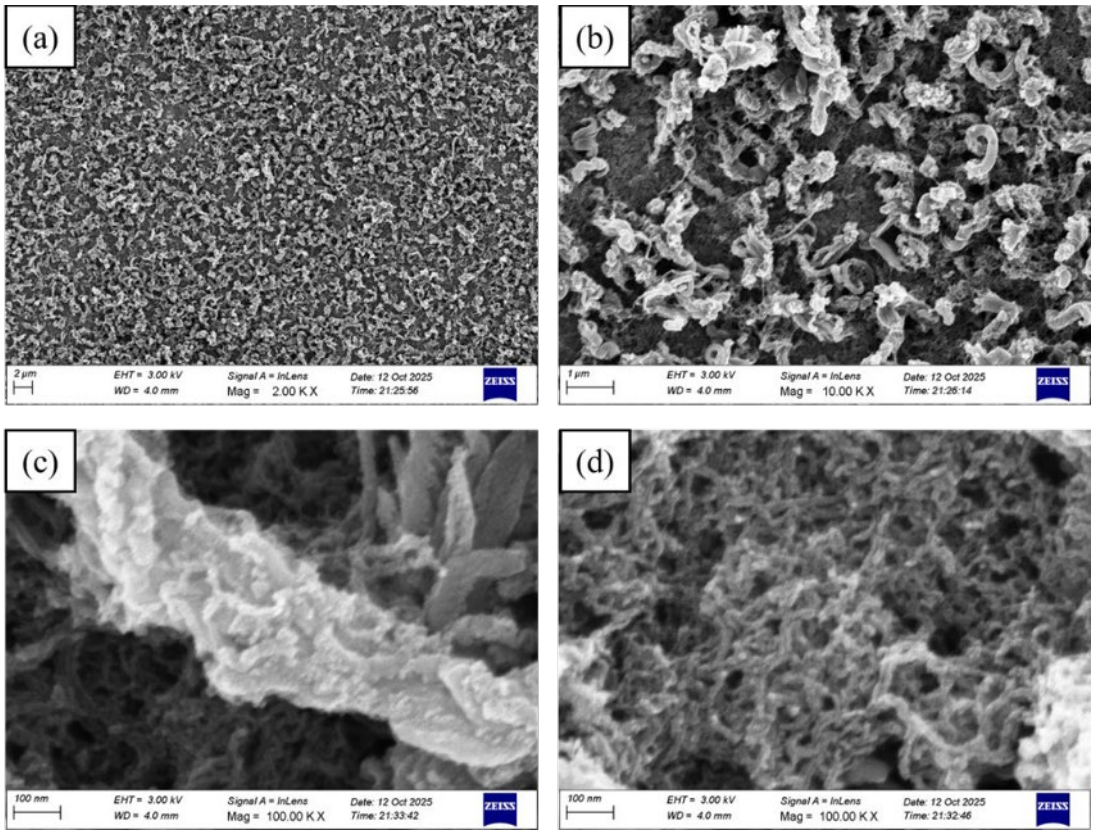


Figure 3.16. SEM images of Carbon nanofiber clusters on silicon carbide template (a) 2k, (b) 10k X, (c) thick CNT clusters at 100k X, (d) thin CNT clusters at 100k X.

3.4. Conclusion

In conclusion, this work demonstrates an effective strategy for constructing high-performance 3D carbon electrodes from high-resolution 3D-printed Elegoo templates (30 µm), using tannic acid (TA) as the carbon precursor and $FeCl_3$ as the graphitization catalyst. As a widely used natural polyphenolic carbon precursor, tannic acid is particularly attractive because of its high aromatic content, abundant phenolic hydroxyl groups, strong ability to form coordination and hydrogen-bonding networks with other chemicals, and intrinsically high carbon residue after pyrolysis. These features make TA highly effective for improving char yield, suppressing excessive shrinkage, and preserving the integrity of complex printed architectures during carbonization. In addition, the concentration ratio between $FeCl_3$ and tannic acid plays a critical role in determining the surface morphology, dimensional retention, and char yield. Through the $FeCl_3$ and TA infiltration process, we can increase the areal capacitance of the 3D pyrolytic Elegoo electrode from 1.95 F/cm^2 to 5.22 F/cm^2 at 5 mA/cm^2, a 2.6-fold improvement; increase the char yield from 7.8 wt% to 30 wt%; and increase the volumetric retention from 6.8% to 30.7%. Overall, our results show that additional precursor- and catalyst-assisted infiltration can effectively overcome the limitations of electrodes generated by direct polymer carbonization of 3D carbon, offering a promising route toward mechanically stable, high-surface-area, and electrochemically efficient 3D carbon electrodes for supercapacitors and related energy-storage applications. (**Table 3.4**)

Table 3.4. The electrochemical performance of the 3D-printed carbon electrode in this work compared with previous literature with similar thickness.

Materials	AM method	thickness	electrolyte	Areal capacitance	Ref
CO_2 activated pyrolytic Elegoo-66% burned off	SLA	1.5 mm	1 M Na_2SO_4	5.25 F/cm^2 at 3 mA/cm^2, 4.27 F/cm^2 at 30 mA/cm^2	[37]
CO_2 activated pyrolytic Elegoo-16% burned off	SLA	1.5 mm	1 M Na_2SO_4	2.41 F/cm^2 at 3 mA/cm^2, 1.46 F/cm^2 at 30 mA/cm^2	[37]
Graphene aerogel	DIW	2 mm	2 M KOH	0.91 F/cm^2 at 0.1 A/g (1.35 mA/cm^2)	[38]
cellulose nanofibers + MWCNT + Urea (5 layer)	DIW	2 mm	1 M H_2SO_4	3.82 F/cm^2 at 2 mA/cm^2, 2.65 F/cm^2 at 30 mA/cm^2	[39]
Surface functionalized 3D graphene aerogel	DIW	2 mm	3 M LiCl	1.58 F/cm^2 at 2 mA/cm^2, 1.16 F/cm^2 at 100 mA/cm^2	[40]
Pyrolytic 3D printed N-doped SWCNT+Urea (3 layer)	DIW	2 mm	1 M H_2SO_4	2.14 F/cm^2 at 1 A/g (14.2 mA/cm^2), 1.81 F/cm^2 at 10 A/g (142 mA/cm^2)	[41]
Fe-tannic acid infiltrated pyrolytic Elegoo	CLIP	2 mm	0.5 M H_2SO_4	5.58 F/cm^2 at 2.5 mA/cm^2, 5.22 F/cm^2 at 5 mA/cm^2, 4.71 F/cm^2 at 30 mA/cm^2	This work

References

[1] F. Béguin, V. Presser, A. Balducci, E. Frackowiak, Carbons and Electrolytes for Advanced Supercapacitors, Advanced Materials 26 (2014) 2219–2251. https://doi.org/10.1002/adma.201304137.

[2] H. Meskher, D. Ghernaout, A.K. Thakur, F.S. Jazi, Q.F. Alsalhy, S.S. Christopher, R. Sathyamurhty, R. Saidur, Prospects of functionalized carbon nanotubes for supercapacitors applications, Materials Today Communications 38 (2024) 108517. https://doi.org/10.1016/j.mtcomm.2024.108517.

[3] P. Forouzandeh, V. Kumaravel, S.C. Pillai, [Review] Electrode Materials for Supercapacitors: A Review of Recent Advances, Catalysts 10 (2020) 969. https://doi.org/10.3390/catal10090969.

[4] Z. Yang, J. Tian, Z. Yin, C. Cui, W. Qian, F. Wei, Carbon nanotube- and graphene-based nanomaterials and applications in high-voltage supercapacitor: A review, Carbon 141 (2019) 467–480. https://doi.org/10.1016/j.carbon.2018.10.010.

[5] L.F. Aval, M. Ghoranneviss, G.B. Pour, High-performance supercapacitors based on the carbon nanotubes, graphene and graphite nanoparticles electrodes, Heliyon 4 (2018). https://doi.org/10.1016/j.heliyon.2018.e00862.

[6] L.L. Zhang, X.S. Zhao, Carbon-based materials as supercapacitor electrodes, Chem. Soc. Rev. 38 (2009) 2520–2531. https://doi.org/10.1039/B813846J.

[7] P. Blyweert, V. Nicolas, J. Macutkevic, V. Fierro, A. Celzard, Tannin-Based Resins for 3D printing of Porous Carbon Architectures, ACS Sustainable Chem. Eng. 10 (2022) 7702–7711. https://doi.org/10.1021/acssuschemeng.2c01686.

[8] J. Wei, Y. Liang, Y. Hu, B. Kong, G.P. Simon, J. Zhang, S.P. Jiang, H. Wang, A Versatile Iron–Tannin-Framework Ink Coating Strategy to Fabricate Biomass-Derived Iron Carbide/Fe-N-Carbon Catalysts for Efficient Oxygen Reduction, Angew Chem Int Ed 55 (2016) 1355–1359. https://doi.org/10.1002/anie.201509024.

[9] P. Blyweert, V. Nicolas, V. Fierro, A. Celzard, Experimental Design Optimization of Acrylate—Tannin Photocurable Resins for 3D Printing of Bio-Based Porous Carbon Architectures, Molecules 27 (2022) 2091. https://doi.org/10.3390/molecules27072091.

[10] C. Chen, H. Yang, X. Yang, Q. Ma, Tannic acid: a crosslinker leading to versatile functional polymeric networks: a review, RSC Advances 12 (2022) 7689–7711. https://doi.org/10.1039/D1RA07657D.

[11] A. Janošević Ležaić, D. Bajuk-Bogdanović, J. Krstić, Z. Jovanović, Ž. Mravik, J. Kovač, N. Gavrilov, What role does carbonized tannic acid play in energy storage composites, Fuel 312 (2022) 122930. https://doi.org/10.1016/j.fuel.2021.122930.

[12] J. Luo, J. Lai, N. Zhang, Y. Liu, R. Liu, X. Liu, Tannic Acid Induced Self-Assembly of Three-Dimensional Graphene with Good Adsorption and Antibacterial Properties, ACS Sustainable Chem. Eng. 4 (2016) 1404–1413. https://doi.org/10.1021/acssuschemeng.5b01407.

[13] H. Li, K. Du, C. Xiang, P. An, X. Shu, Y. Dang, C. Wu, J. Wang, W. Du, J. Zhang, S. Li, H. Tian, S. Wang, H. Xia, Controlled chelation between tannic acid and Fe precursors to obtain N, S co-doped carbon with high density Fe-single atom-nanoclusters for highly efficient oxygen reduction reaction in Zn–air batteries, J. Mater. Chem. A 8 (2020) 17136–17149. https://doi.org/10.1039/D0TA04210B.

[14] Q. Qin, H. Jang, P. Li, B. Yuan, X. Liu, J. Cho, A Tannic Acid–Derived N-, P-Codoped Carbon-Supported Iron-Based Nanocomposite as an Advanced Trifunctional Electrocatalyst for the Overall Water Splitting Cells and Zinc–Air Batteries, Advanced Energy Materials 9 (2019) 1803312. https://doi.org/10.1002/aenm.201803312.

[15] N. Hammi, S. Chen, F. Dumeignil, S. Royer, A. El Kadib, Chitosan as a sustainable precursor for

nitrogen-containing carbon nanomaterials: synthesis and uses, Materials Today Sustainability 10 (2020) 100053. https://doi.org/10.1016/j.mtsust.2020.100053.

[16] C. Zhang, L. Chao, Z. Zhang, L. Zhang, Q. Li, H. Fan, S. Zhang, Q. Liu, Y. Qiao, Y. Tian, Y. Wang, X. Hu, Pyrolysis of cellulose: Evolution of functionalities and structure of biochar versus temperature, Renewable and Sustainable Energy Reviews 135 (2021) 110416. https://doi.org/10.1016/j.rser.2020.110416.

[17] S.D. Stefanidis, K.G. Kalogiannis, E.F. Iliopoulou, C.M. Michailof, P.A. Pilavachi, A.A. Lappas, A study of lignocellulosic biomass pyrolysis via the pyrolysis of cellulose, hemicellulose and lignin, Journal of Analytical and Applied Pyrolysis 105 (2014) 143–150. https://doi.org/10.1016/j.jaap.2013.10.013.

[18] C. Falco, N. Baccile, M.-M. Titirici, Morphological and structural differences between glucose, cellulose and lignocellulosic biomass derived hydrothermal carbons, Green Chem. 13 (2011) 3273–3281. https://doi.org/10.1039/c1gc15742f.

[19] M. Li, W. Li, S. Liu, Hydrothermal synthesis, characterization, and KOH activation of carbon spheres from glucose, Carbohydrate Research 346 (2011) 999–1004. https://doi.org/10.1016/j.carres.2011.03.020.

[20] P. Guo, Y. Gu, Z. Lei, Y. Cui, X.S. Zhao, Preparation of sucrose-based microporous carbons and their application as electrode materials for supercapacitors, Microporous and Mesoporous Materials 156 (2012) 176–180. https://doi.org/10.1016/j.micromeso.2012.02.043.

[21] K. Jurkiewicz, B. Liszka, P. Gancarz, S. Smykała, D. Zygadło, P. Nokielski, T. Lamrani, E. Talik, R. Wrzalik, M. Walkowiak, J. Ilavsky, Sucrose-Based Dense, Pure, and Highly-Crystalline Graphitic Materials for Lithium-Ion Batteries, (n.d.). https://doi.org/10.1002/adfm.202410409.

[22] J. Yang, S. Zuo, Facile synthesis of graphitic mesoporous carbon materials from sucrose, Diamond and Related Materials 95 (2019) 1–4. https://doi.org/10.1016/j.diamond.2019.03.018.

[23] D. Chen, K. Cen, X. Zhuang, Z. Gan, J. Zhou, Y. Zhang, H. Zhang, Insight into biomass pyrolysis mechanism based on cellulose, hemicellulose, and lignin: Evolution of volatiles and kinetics, elucidation of reaction pathways, and characterization of gas, biochar and bio-oil, Combustion and Flame 242 (2022) 112142. https://doi.org/10.1016/j.combustflame.2022.112142.

[24] Q. Yan, J. Li, X. Zhang, E.B. Hassan, C. Wang, J. Zhang, Z. Cai, Catalytic graphitization of kraft lignin to graphene-based structures with four different transitional metals, J Nanopart Res 20 (2018) 223. https://doi.org/10.1007/s11051-018-4317-0.

[25] S. Dbira, N. Bensalah, M.M. Zagho, M. Ennahaoui, A. Bedoui, Oxidative Degradation of Tannic Acid in Aqueous Solution by UV/S2O82− and UV/H2O2/Fe2+ Processes: A Comparative Study, Applied Sciences 9 (2019) 156. https://doi.org/10.3390/app9010156.

[26] W. Zhang, Y. Cheng, P. Ma, Y. Fang, B. Liu, Degradation of tannic acid using monopersulfate activated CuO particles, Desalination and Water Treatment 317 (2024) 100177. https://doi.org/10.1016/j.dwt.2024.100177.

[27] C. Zhang, B. Wu, Y. Zhou, F. Zhou, W. Liu, Z. Wang, Mussel-inspired hydrogels: from design principles to promising applications, Chem. Soc. Rev. 49 (2020) 3605–3637. https://doi.org/10.1039/c9cs00849g.

[28] J. Saiz-Poseu, J. Mancebo-Aracil, F. Nador, F. Busqué, D. Ruiz-Molina, The Chemistry behind Catechol-Based Adhesion, Angewandte Chemie International Edition 58 (2019) 696–714. https://doi.org/10.1002/anie.201801063.

[29] A. Baldwin, B.W. Booth, Biomedical applications of tannic acid, J Biomater Appl 36 (2022) 1503–1523. https://doi.org/10.1177/08853282211058099.

[30] K.S. Novoselov, V.I. Fal′ko, L. Colombo, P.R. Gellert, M.G. Schwab, K. Kim, A roadmap for

graphene, Nature 490 (2012) 192–200. https://doi.org/10.1038/nature11458.

[31] K. Liu, H. Li, Y. Wang, X. Gou, Y. Duan, Adsorption and removal of rhodamine B from aqueous solution by tannic acid functionalized graphene, Colloids and Surfaces A: Physicochemical and Engineering Aspects 477 (2015) 35–41. https://doi.org/10.1016/j.colsurfa.2015.03.048.

[32] W. Pholauyphon, P. Charoen-amornkitt, T. Suzuki, S. Tsushima, Guidelines for supercapacitor electrochemical analysis: A comprehensive review of methodologies for finding charge storage mechanisms, Journal of Energy Storage 98 (2024) 112833. https://doi.org/10.1016/j.est.2024.112833.

[33] L.-Q. Mai, A. Minhas-Khan, X. Tian, K.M. Hercule, Y.-L. Zhao, X. Lin, X. Xu, Synergistic interaction between redox-active electrolyte and binder-free functionalized carbon for ultrahigh supercapacitor performance, Nat Commun 4 (2013) 2923. https://doi.org/10.1038/ncomms3923.

[34] W. Pholauyphon, P. Charoen-amornkitt, T. Suzuki, S. Tsushima, Guidelines for supercapacitor electrochemical analysis: A comprehensive review of methodologies for finding charge storage mechanisms, Journal of Energy Storage 98 (2024) 112833. https://doi.org/10.1016/j.est.2024.112833.

[35] H. Ejima, J.J. Richardson, K. Liang, J.P. Best, M.P. Van Koeverden, G.K. Such, J. Cui, F. Caruso, One-Step Assembly of Coordination Complexes for Versatile Film and Particle Engineering, Science 341 (2013) 154–157. https://doi.org/10.1126/science.1237265.

[36] G. Fu, X. Yan, Y. Chen, L. Xu, D. Sun, J.-M. Lee, Y. Tang, Boosting Bifunctional Oxygen Electrocatalysis with 3D Graphene Aerogel-Supported Ni/MnO Particles, Advanced Materials 30 (2018) 1704609. https://doi.org/10.1002/adma.201704609.

[37] Y. Katsuyama, N. Haba, H. Kobayashi, K. Iwase, A. Kudo, I. Honma, R.B. Kaner, Macro- and Nano-Porous 3D-Hierarchical Carbon Lattices for Extraordinarily High Capacitance Supercapacitors, Advanced Functional Materials 32 (2022) 2201544. https://doi.org/10.1002/adfm.202201544.

[38] Z. Qi, J. Ye, W. Chen, J. Biener, E.B. Duoss, C.M. Spadaccini, M.A. Worsley, C. Zhu, 3D-Printed, Superelastic Polypyrrole–Graphene Electrodes with Ultrahigh Areal Capacitance for Electrochemical Energy Storage, Advanced Materials Technologies 3 (2018) 1800053. https://doi.org/10.1002/admt.201800053.

[39] G. Zhou, M.-C. Li, C. Liu, C. Liu, Z. Li, C. Mei, 3D Printed Nitrogen-Doped Thick Carbon Architectures for Supercapacitor: Ink Rheology and Electrochemical Performance, Advanced Science 10 (2023) 2206320. https://doi.org/10.1002/advs.202206320.

[40] B. Yao, S. Chandrasekaran, H. Zhang, A. Ma, J. Kang, L. Zhang, X. Lu, F. Qian, C. Zhu, E.B. Duoss, C.M. Spadaccini, M.A. Worsley, Y. Li, 3D-Printed Structure Boosts the Kinetics and Intrinsic Capacitance of Pseudocapacitive Graphene Aerogels, Advanced Materials 32 (2020) 1906652. https://doi.org/10.1002/adma.201906652.

[41] W. Kang, L. Zeng, S. Ling, C. Zhang, 3D Printed Supercapacitors toward Trinity Excellence in Kinetics, Energy Density, and Flexibility, Advanced Energy Materials 11 (2021) 2100020. https://doi.org/10.1002/aenm.202100020.

Chapter 4 – Enhancing Energy Storage Performance of Pyrolytic Elegoo Carbon through Secondary Structure Growth - poly(diaminonaphthalene) (PDAN)

Nowadays, the demand for lightweight and compact energy storage systems is attracting increasing attention. At the same time, the continued miniaturization and expanding functionality of electronic devices, especially wearable technologies, together with the rapid growth of artificial intelligence infrastructure, are driving demand for energy storage systems with high gravimetric and volumetric energy densities and high-power density. To achieve these goals, increasing the density of electrochemical reaction sites within a confined volume can significantly improve electrochemical performance.

In parallel, redox-active conjugated polymers are promising energy storage materials due to their high theoretical capacitance, good electrical conductivity, and additional pseudocapacitive charge storage via electrochemically active sites in each repeat unit.[1–3] Their low cost, lightweight nature, and mechanical flexibility further make them attractive candidates for electrode applications. However, poor cycling stability, arising from the large volumetric changes during doping and dedoping, together with performance loss at increased polymer thickness, limits the practical mass loading of these materials in conventional 2D electrodes. Compared with conventional 2D electrodes, 3D architected structures offer a much larger accessible surface area, shorter ion-diffusion pathways, and better accommodation of active materials, making them especially suitable for integrating conducting polymer coatings. Such architectures enable higher polymer loading while maintaining a thin, conformal layer on the electrode surface, thereby minimizing the performance degradation that often occurs when polymer thickness increases.

In Chapter 3, we developed a 3D pyrolytic carbon electrode for energy storage by incorporating Fe and tannic acid (TA) into the printed template prior to carbonization, thereby enabling the formation of a mechanically robust, electrically conductive carbon architecture with high surface area. Although this strategy improved the structural integrity and electrochemical activity of the electrode, the areal capacitance remained insufficient for demanding energy-storage applications.

To further enhance the electrochemical performance of 3D carbon electrodes, we selected poly(diaminonaphthalene) (PDAN) as a secondary structure to graft onto a 3D-printed carbon electrode. Among all conjugated polymers, PDAN is particularly attractive because its naphthalene-based conjugated backbone supports efficient charge transport, while its abundant nitrogen-containing redox sites enable fast, reversible faradaic reactions.

4.1. PDAN deposition on 3D carbon template

4.1.1. PDAN Selection

Redox-active conjugated polymers are promising energy storage materials due to their high theoretical capacitance, good electrical conductivity, and additional pseudocapacitive charge storage. Among conductive polymers, polyaniline (PANI) has attracted significant attention. However, poly(diaminonaphthalene) (PDAN), with two amino groups on the naphthalene ring, offers a higher theoretical energy storage density (1545 F/g) than PANI (1325 F/g). [4] The fused naphthalene ring makes the polymer less hydrophilic than PANI after protonation or cation attachment. It is well known that extended conjugation raises the energy of the highest occupied molecular orbital, thereby facilitating faster electron-transfer kinetics and leading to a lower onset potential for PDAN polymerization. [5,6] The extended π-conjugation of the naphthalene backbone further enhances charge delocalization and redox activity, improving both rate capability and cycling stability. In addition, the multiple redox-active sites along the PDAN polymer chain provide more faradaic contributions per unit mass, making it particularly attractive for high-performance supercapacitor electrodes. These combined advantages motivate our selection of PDAN as the active material in this work.

4.1.2. Experimental section

4.1.2.1. Preparation of diaminonaphthalene (DAN) solution for electropolymerization

A 5 mM DAN solution was prepared in an aqueous electrolyte containing 1.0 M $HClO_4$. $HClO_4$ was used to protonate DAN, improve its solubility in water, and serve as the supporting electrolyte to improve ionic conductivity while remaining chemically inert. After degassing, the electrolyte was purged with N_2 for an additional 30 min before adding DAN. The solution was then continuously stirred under N_2 purge until the monomer was completely dissolved, after which electropolymerization was initiated immediately.

4.1.2.2. Electropolymerization of PDAN

The electropolymerization was performed using a Biologic VSP-3e potentiostat in combination with the EC-Lab program version 11.61. Electropolymerization was carried out by chronoamperometry over a potential range of 0.8 to 1.7 V in 0.1 V increments, with each potential applied for 10 cycles relative to the reference electrode in acidic media. During each chronoamperometric cycle, the potential was held at the target potential (0.8 V, 0.9 V, …, 1.7 V) for 60 s and then switched to 0 V for 60 s. The 0 V hold serves as a relaxation and reset step between deposition pulses. It allows the system to return to near open-circuit conditions, reduces double-layer charging effects, and helps limit overgrowth or overly rapid local polymerization during the next deposition step. After polymerization, the sample was rinsed with DI water and soaked in excess acetonitrile for 12 hours to remove oligomers.

4.2. Mechanistic Insights into PDAN: Electropolymerization and Energy Storage Behavior

4.2.1. Electropolymerization mechanism

The electropolymerization of PDAN is a two-electron-transfer reaction via oxidation of monomers. **Figure 4.1** shows the electropolymerization process of 1,5-DAN monomer to PDAN. The initial step involves the oxidation of the monomer (a) at a given potential (E) to generate the radical cation (b). Then, this unstable radical cation reacts with a monomer to produce the neutral radical (c) and a protonated monomer. The cationic species (d) was obtained by oxidizing the neutral radical. Still, the product in this step undergoes an irreversible chemical reaction to give the dihydro-dimer, which is deprotonated to afford the aromatic dimer (e). The dimer is oxidized to the dication, then coupled with a molecule of (b), and this species is deprotonated to produce the hydro cationic structure (f). Compound (f) then couples with another molecule of (b) to give the next higher homology species, the trimer, which is deprotonated and oxidized to give the oxidized form of the tetramer, and so on. [7]

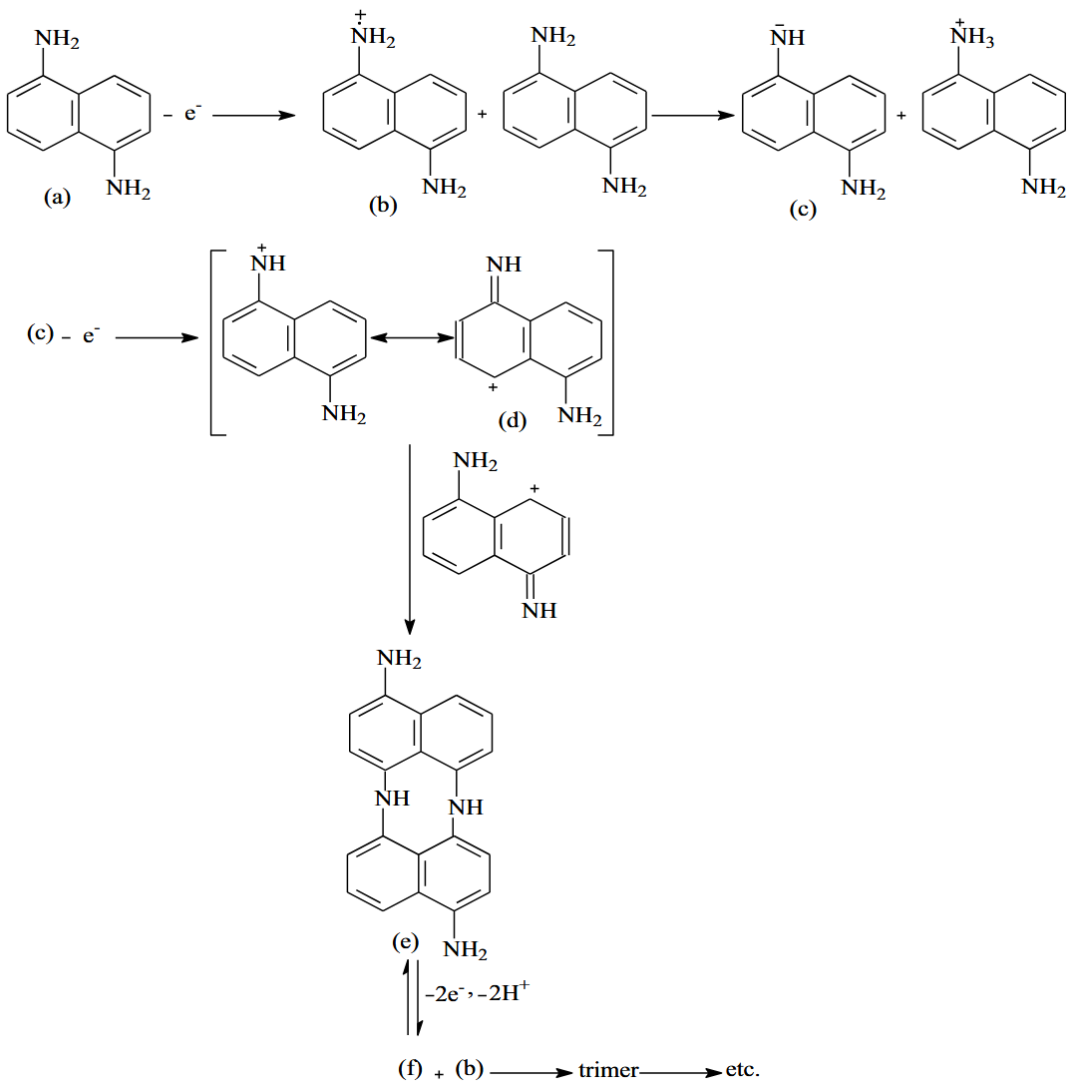


Figure 4.1. Suggested mechanism of 1,5-diaminonaphthalene electropolymerization.[7]

4.2.2. Charge storage mechanism

The charge storage mechanism of PDAN is dominated by reversible faradaic redox reactions of its amino (-NH-)/imino (-N=) groups along the conjugated polymer backbone, allowing π-electrons to delocalize and giving the material pseudocapacitive behavior rather than pure electric double-layer capacitance (EDLC). During charge and discharge, the polymer undergoes rapid ion-coupled electron transfer, so charge is stored through surface/near-surface redox processes that can proceed much faster than bulk diffusion-limited reactions. More specifically, during discharge, the imino group in PDAN receives electrons, reducing it to (-N^--) with a negative charge, which can combine with protons or cations (metal ions in a metal salt solution). During the charge process, the negatively charged group is oxidized back to the imino group, releasing protons and cations into the electrolyte. If we continue to charge PDAN to a more positive potential, the amino group is further oxidized to a (-N^+H=) group with a positive charge, which can interact with anions in

the electrolyte. (**Figure 4.2**) [8,9] On the other hand, the amino group in ladder PDAN receives electrons and becomes a negatively charged (-N^--) group, attracting protons and cations during the discharge process, and the (-N^--) group oxidizes back to the amino group during the charge process. [4,8] (**Figure 4.3**) In aqueous electrolytes, both protons and other cations can participate in the redox process depending on the electrolyte composition, which helps explain the high capacity, fast kinetics, and good cycling stability reported for PDAN-based electrodes. [8–10]

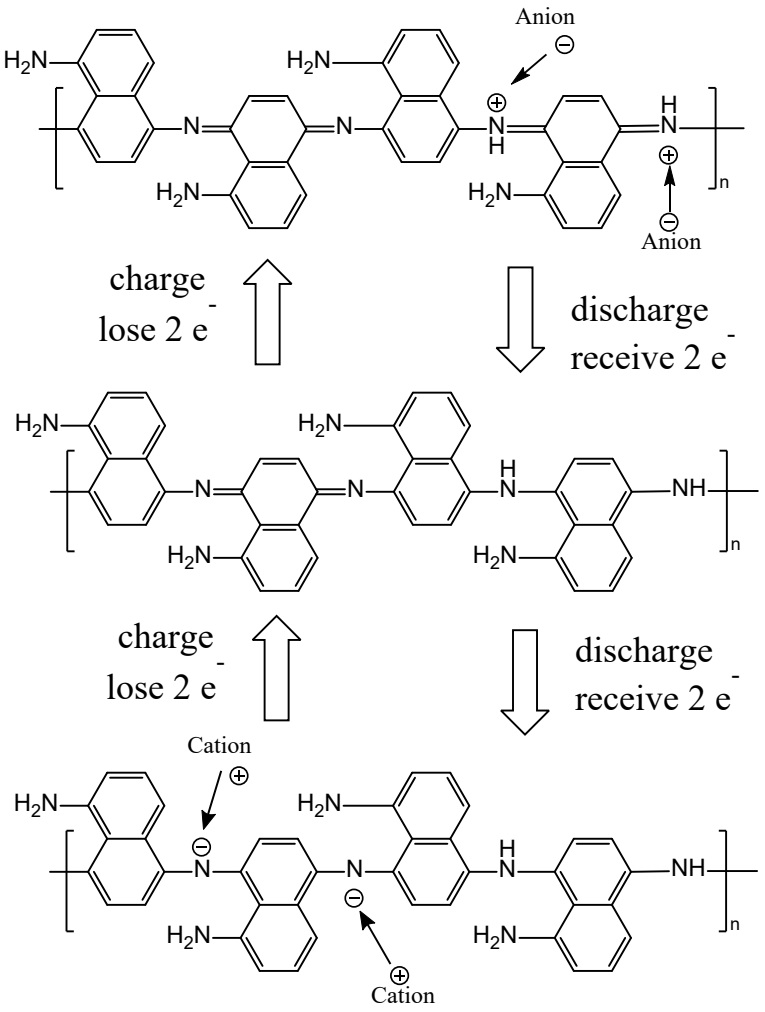


Figure 4.2. Charge-storage mechanism of a bipolar branched PDAN during the charge/discharge process.

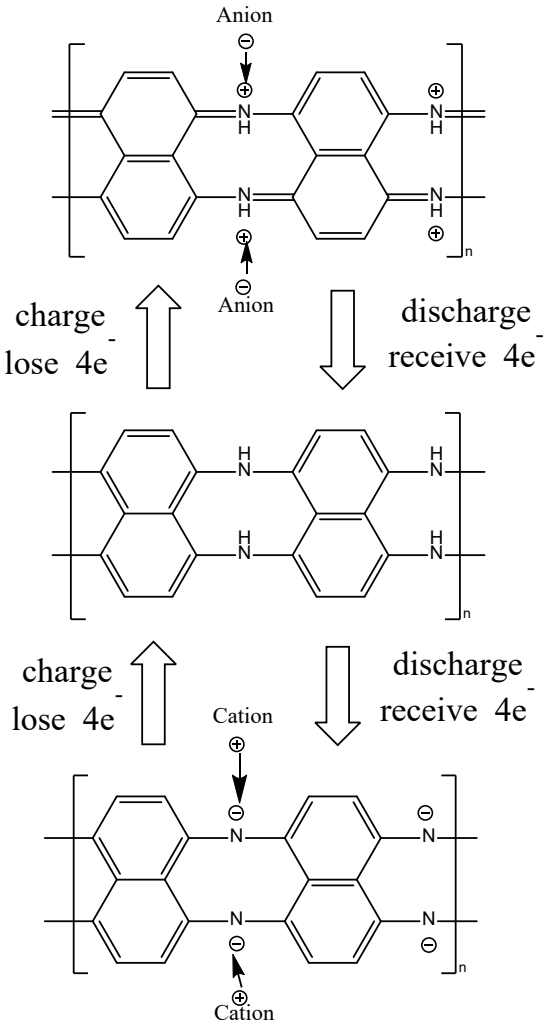


Figure 4.3. Charge-storage mechanism of laddered PDAN during the charge/discharge process.

4.3. Results and Discussion

4.3.1. Conformal PDAN deposition on 3D carbon electrode

PDAN was electrochemically deposited onto the pyrolyzed Elegoo-derived 3D carbon electrode via oxidative electropolymerization. As shown in the SEM images (**Figure 4.4**), the oxidative grafting process produced a conformal PDAN coating on the carbon struts, partially smoothing the surface and covering some of the pores. Owing to the redox-active units in PDAN, the electrochemically active surface area (ECSA), which can be quantified by cyclic voltammetry, increased rather than decreased after polymerization, despite the pores being covered by the PDAN-deposited layer. After PDAN deposition, the areal capacitance increased from 4.12 F/cm^2 to 8.14 F/cm^2 in 0.5 M H_2SO_4 at 5 mV/s, and from 3.09 F/cm^2 to 4.33 F/cm^2 in 3 M $NaClO_4$ at 5 mV/s.

In addition, the reduced ionic diffusion resistance observed for the coated electrode, followed by a gradual increase with film thickness, suggests that PDAN facilitates electrolyte transport while lowering

interfacial resistance; this is discussed in more detail in **Section 4.3.5**. In contrast, the higher diffusion resistance measured in the porous 3D carbon scaffold is likely attributable to the carbon's hydrophobicity and the longer ion-transport pathways within the porous architecture.

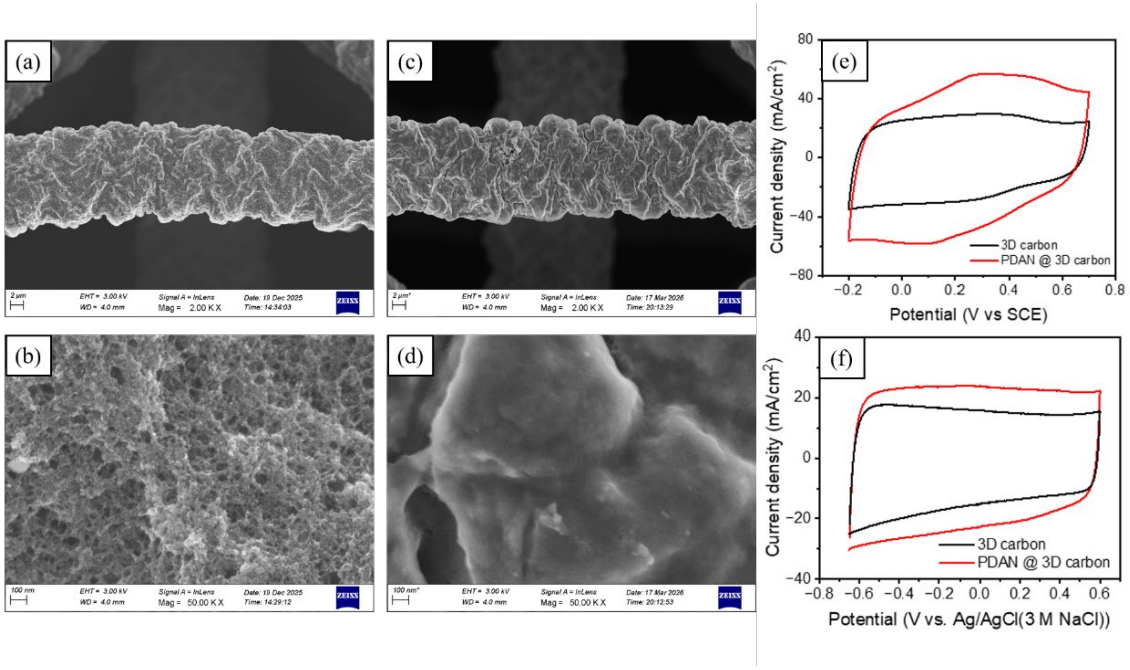


Figure 4.4. SEM images before PDAN deposition (a, b), and after PDAN deposition (c, d), showing the conformal PDAN coating and resulting smooth surface morphology, (e) Cyclic voltammetry in 0.5 M H_2SO_4 at 5 mV/s, (f) Cyclic voltammetry in 3 M $NaClO_4$ at 5 mV/s.

4.3.2. Enhanced capacitance by additional pseudocapacitance from PDAN

As discussed in **Section 4.2.2**, the amino/imino groups in the conjugated polymer networks of PDAN can interact with metal ions and protons via reversible intercalation and deintercalation. To improve the electrochemical performance of 3D carbon electrodes, I grew a secondary PDAN layer on them. The electrochemical performance of the Fe-TA-treated 3D carbon lattices for supercapacitors was measured using half-cell tests in three-electrode beaker cells. **Figure 4.5** presents the cyclic voltammetry (CV) curves of different samples at 5 mV/s; [11] the capacitance improves significantly due to the increased surface area of Fe-TA infiltration and the pseudocapacitance from PDAN. **Figure 4.5**. presents the GCD curves of 3D carbon prepared from pure polymer (labeled as 3D carbon_P in **Figure 4.5**), 3D carbon prepared with Fe-TA infiltration, and PDAN-coated Fe-TA-treated 3D carbon in 0.5 M H_2SO_4, the two 3D carbon electrodes show nearly triangular GCD curves, indicating a fast ion diffusion and charge transfer. In contrast, the PDAN-coated sample shows a non-linear and asymmetric charge–discharge curve, reflecting the contribution of pseudocapacitance from the conducting polymer. Among them, the PDAN coated-3D carbon exhibits the most extended charge and discharge time with extraordinarily high areal capacitance of 7.87, 8.06, 8.25, 8.50, 8.89 F/cm^2 at 30, 20, 15, 10, 5 mA/cm^2. In contrast, control sample (untreated pyrolytic Elegoo 3D carbon) exhibits 1.29, 1.41, 1.50, 1.65, 1.95 F/cm^2 at 30, 20, 15, 10, 5 mA/cm^2, and 3D carbon (Fe-TA treated Elegoo 3D carbon) exhibits 4.74, 4.76, 4.81, 4.90, 5.07 F/cm^2 at 30, 20, 15, 10, 5 mA/cm^2. (shown in **Figure 4.5**)

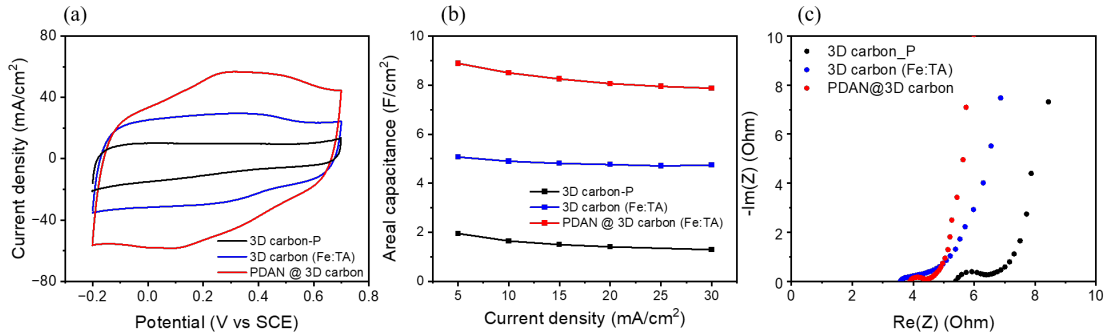


Figure 4.5. (a) Cyclic voltammetry of 3D carbon prepared from pure polymer (3D carbon_P), 3D carbon prepared with Fe-TA infiltration, and PDAN-coated Fe-TA-treated 3D carbon in 0.5 M H_2SO_4 at 5 mV/s, (b) Areal capacitance of the 3D carbon_P, 3D carbon (Fe: TA), and PDAN@3D carbon in 0.5 M H_2SO_4 calculated from GCD, (c) Nyquist plot of the 3D carbon_P, 3D carbon (Fe: TA), and PDAN@3D carbon in 0.5 M H_2SO_4.

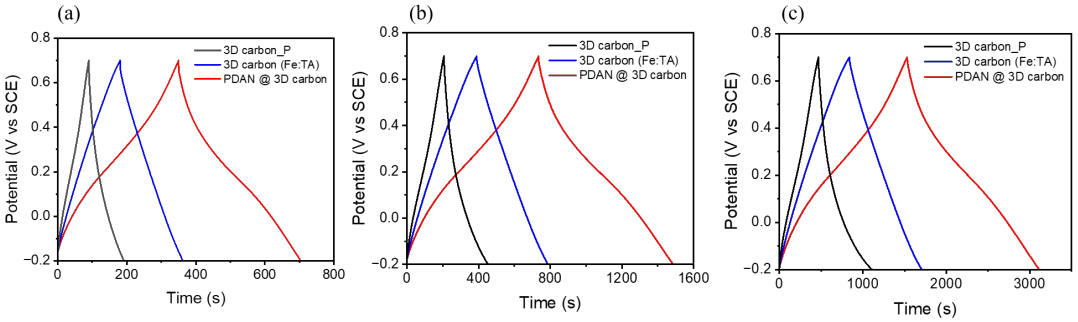


Figure 4.6. GCD curves of 3D carbon prepared from pure polymer (3D carbon_P), 3D carbon prepared with Fe-TA infiltration, and PDAN-coated Fe-TA-treated 3D carbon in 0.5 M H_2SO_4 at (a) 20 mA/cm^2, (b)10 mA/cm^2, (c) 5 mA/cm^2.

To further elucidate the charge-storage mechanism of PDAN, the electrochemical behavior of 3D carbon electrodes with and without PDAN was examined in different electrolytes, 0.5 M H_2SO_4 and 3 M $NaClO_4$. **Figure 4.7** presents the cyclic voltammetry (CV) curves of 3D carbon before and after PDAN deposition versus Ag/AgCl (3 M NaCl) in different electrolytes at scan rates of 10 and 2 mV/s. Among these two electrolytes, H^+ produced a more pronounced enhancement in areal capacitance at low scan rates than Na^+ (**Figure 4.8**). In H_2SO_4, the capacitance improvement after PDAN coating is much larger because the polymer is more effectively protonated and more strongly coupled to the charge-storage process. Protons are much smaller than Na^+, so they can penetrate the PDAN layer and access redox-active sites more easily. They also move faster in the electrolyte, which supports faster ion–electron transport during charging and discharging. In addition, PDAN contains nitrogen functionalities that interact strongly with H^+ via protonation, thereby increasing the density of reversible faradaic sites and enhancing the pseudocapacitive contribution. In contrast, Na^+ has a larger hydration shell and weaker interaction with the PDAN backbone. Hence, its insertion/protonation-like participation is more limited, and the capacitance gain is therefore smaller in $NaClO_4$. This explains why the PDAN coating produces a much larger enhancement in 0.5 M H_2SO_4 than in 3 M $NaClO_4$.

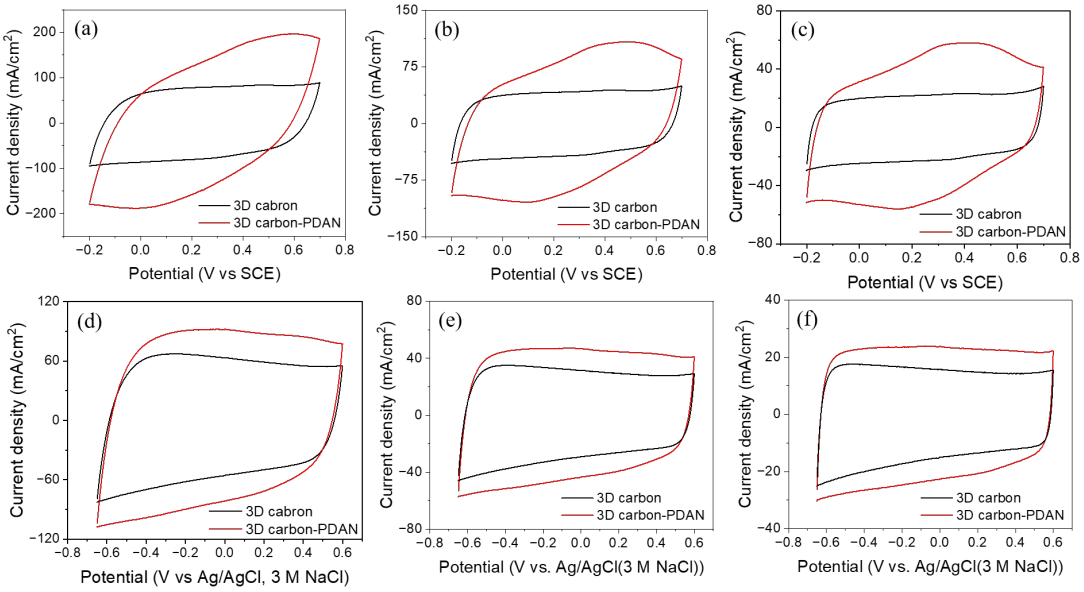
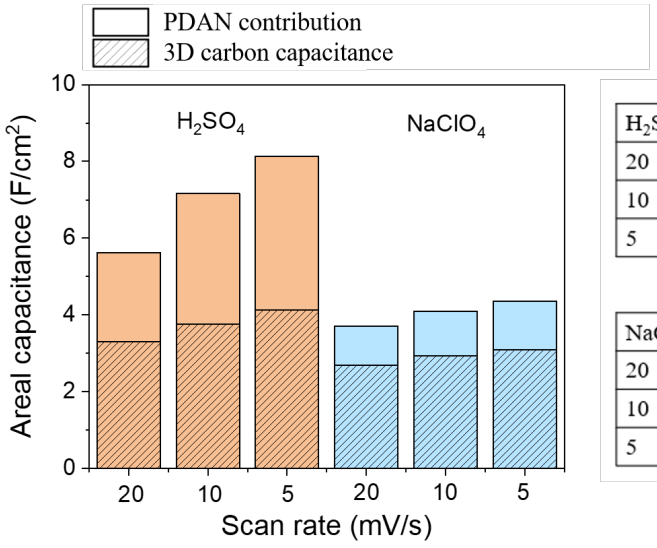


Figure 4.7. Cyclic voltammetry of 3D carbon before and after PDAN deposition in 0.5 M H_2SO_4 (a-c) at 20, 10, 5 mV/s in 0.5 M H_2SO_4, and (d-f) at 20, 10, 5 mV/s in 3 M $NaClO_4$



H_2SO_4	Before PDAN	After PDAN
20	3.31 F/cm²	5.62 F/cm² (70%)
10	3.76 F/cm²	7.16 F/cm² (90%)
5	4.12 F/cm²	8.14 F/cm² (97%)

$NaClO_4$	Before PDAN	After PDAN
20	2.68 F/cm²	3.72 F/cm² (39%)
10	2.93 F/cm²	4.09 F/cm² (40%)
5	3.09 F/cm²	4.35 F/cm² (41%)

Figure 4.8. Areal capacitance improvement after PDAN deposition on 3D carbon electrodes in 0.5 M H_2SO_4 and 3 M $NaClO_4$ at scan rates of 20, 10, and 5 mV/s. (Four different 3D carbon samples were evaluated before and after PDAN deposition in both electrolytes.)

4.3.3. Electrochemical performance of different PDAN thicknesses (deposited at different potentials)

The thickness of the PDAN coating on 3D carbon electrodes strongly influences electrochemical performance by controlling the balance among active material loading, ion transport, and electrical conductivity. When the PDAN coating is too thin, only a small amount of redox-active polymer is available, so the overall capacitance gain is small even though charge transfer is fast. As the thickness increases to an

optimal range, more electroactive sites are introduced. At the same time, the coating can remain conformal and electrically connected to the carbon scaffold, which usually yields the best overall performance in terms of areal capacitance, charge-transfer resistance, and utilization efficiency. However, if the polymer layer becomes too thick, ion diffusion through the film slows, the inner portion of the PDAN may become electrochemically inaccessible, and the larger volume changes associated with the doping and dedoping processes can generate mechanical stress, cracking, or delamination. This thickness effect is especially important on a 3D PDAN-coated electrode because the 3D architecture can tolerate more active material loading than a conventional 2D electrode, but only if the polymer remains thin enough to preserve open pathways for electrolyte penetration and fast redox kinetics, and to deliver better rate capacity and cycle life. [12,13]

The electrochemical performance of the Fe-TA-treated 3D carbon lattices for supercapacitors was measured using half-cell tests in three-electrode beaker cells. **Figure 4.9** presents the cyclic voltammetry (CV) curves of 1.2 V PDAN-deposited 3D carbon and 1.7 V PDAN-deposited 3D carbon in the range from –0.65 to 0.6 V versus Ag/AgCl (3 M NaCl) in 3 M $NaClO_4$ at various scan rates (1-10 mV/s). Among them, the 1.7 V PDAN-deposited 3D carbon is the only one that shows clear redox peaks and does not remain rectangular in its cyclic voltammogram, while also exhibiting the highest areal capacitances of 4.99, 5.13, 5.37, 5.73, and 6.02 F/cm^2 at 10, 8, 5, 2, and 1 mV/s. On the other hand, the 1.2 V PDAN-deposited 3D carbon sample only exhibits areal capacitances of 4.09, 4.19, 4.35, 4.59, 4.73 F/cm^2 at 10, 8, 5, 2, 1 mV/s; this is because the higher polymer loading in the 1.7 V PDAN sample provides more accessible redox-active sites, increasing the pseudocapacitive contribution and resulting in higher capacitance than the thinner PDAN-coated sample.

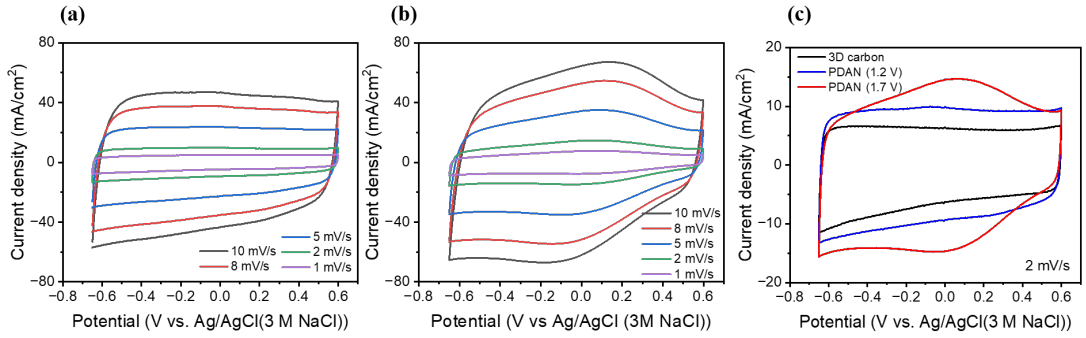


Figure 4.9. (a) Cyclic voltammetry curves at 1, 2, 5, 8, and 10 mV/s of 1.2 V-PDAN deposition 3D carbon in 3 M $NaClO_4$, (b) Cyclic voltammetry curves at 1, 2, 5, 8, and 10 mV/s of 1.7V-PDAN deposition 3D carbon in 3 M $NaClO_4$, (c) Cyclic voltammetry curves at 2 mV/s of 3D carbon, 1.2 V-PDAN deposition 3D carbon in 3 M $NaClO_4$.

To further confirm the effect of different PDAN thickness, we took another 3D carbon electrode to deposit PDAN at different potentials. **Figure 4.10. a** presents the cyclic voltammetry (CV) curves of a 3D carbon electrode with and without PDAN deposition in the range from –0.65 to 0.6 V versus Ag/AgCl (3 M NaCl) in 3 M $NaClO_4$ at 5 mV/s. Among them, the 1.45 V PDAN-deposited 3D carbon is the only one that shows clear redox peaks and does not remain rectangular in its cyclic voltammogram, while also exhibiting the highest areal capacitance of 5.53 F/cm^2 at 5 mV/s, an 85% increase from 3D carbon without PDAN deposition (2.98 F/cm^2). On the other hand, the 1.3 V PDAN-deposited 3D carbon sample only exhibits an areal capacitance of 4.44 F/cm^2 at 5 mV/s. **Figure 4.10.b** shows the galvanostatic charge and discharge (GCD) curves of the 3D carbon electrode with and without PDAN deposition in the range from –0.65 to 0.6 V versus Ag/AgCl (3 M NaCl) in 3 M $NaClO_4$ at 5 mA/cm^2. All of them show nearly triangular GCD profiles, indicating fast ion diffusion and electron transfer during the charge and discharge processes; however, we still observe a distortion of the GCD curve in the 1.45 V-PDAN-deposited sample due to pseudocapacitance from redox reactions. The 1.45 V-PDAN-deposited sample exhibits the most extended charge and discharge with outstanding areal capacitances of 6.08, 5.86, 5.70, 5.66, 5.65 F/cm^2 at 5, 10, 20, 30, 50 mA/cm^2, while

1.30 V-PDAN-deposited sample exhibits 4.42, 4.32, 4.22, 4.16, 4.09, 3.99 F/cm^2, and 3D carbon electrode without PDAN exhibits 3.05, 2.96, 2.88, 2.84, 2.80 at 5, 10, 20, 30, 50 mA/cm^2. (**Figure 4.10.c)**

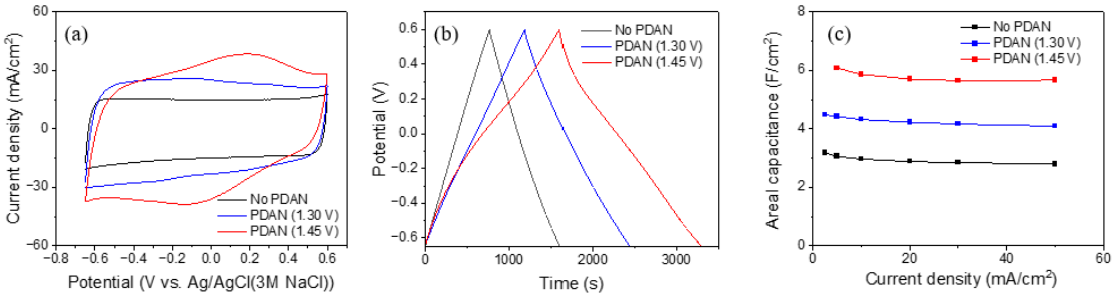


Figure 4.10 (a) Cyclic voltammetry curves in 3 M $NaClO_4$ at 5 mV/s before and after PDAN deposition, (b) GCD curves in 3 M $NaClO_4$ at 5 mA/cm^2 before and after PDAN deposition, and (c) areal capacitance calculated from GCD data in 3 M $NaClO_4$ before and after PDAN deposition.

4.3.4. Redox kinetics (capacitive and diffusive contribution) on PDAN-coated 3D carbon electrodes

Understanding capacitive and diffusive kinetics is important because it can tell not just how much charge an electrode can store, but how it stores it and how fast the process is. Capacitive-dominated behavior generally indicates rapid, surface-controlled charge storage and better power performance. In contrast, diffusive-dominated behavior indicates slower ion transport, which can limit rate capability but improve total capacity. It is especially useful when the electrodes are 3D structures, porous carbons, or polymer-based electrodes, where transport bottlenecks and surface accessibility can change dramatically with structure and cycling.

To elucidate the charge-storage mechanism of the 3D electrode materials, the relative contributions from capacitive-controlled (fast kinetics) and diffusion-controlled (slow kinetics) processes were evaluated using the b-value analysis, Dunn's method, and the Trasatti method. The b-value approach, Dunn's analysis, and the Trasatti method are all used, but they answer slightly different questions about charge-storage kinetics. (As shown in **Table 4.1**)

1. The b-value gives a fast first look at whether a process is more capacitive or diffusion-limited at a given potential, which is the simplest and fastest method.
2. Dunn's analysis deconvolutes the CV into capacitive and diffusion-controlled current across the whole voltage window, offering more details at different potentials.
3. Trasatti method estimates the overall outer-surface versus inner/diffusion-limited contribution by scan-rate extrapolation, giving an estimation of accessible vs less-accessible charge storage.

Table 4.1 Comparison of different analysis methods to investigate charge-storage mechanism

Methods	Pros	Cons	Reference
b-value analysis	Simple to apply from CV peak-current vs scan-rate data. Gives a quick first-look estimate of whether a process is more capacitive- or diffusion-	It is only an empirical power-law fit, so it does not fully separate mixed kinetics. Less informative for broad and	[14,15]

	controlled. Useful for comparing redox peaks or potential regions.	non-peak-shaped responses.	
Dunn's analysis	Provides potential-resolved separation of capacitive and diffusion-controlled current. More mechanistic than b-value analysis because it deconvolutes the whole CV curve. Very useful for visualizing how kinetics change across the voltage window.	Relies on simplifying assumptions about current decomposition. Can be distorted by thick films, high resistance, or heterogeneous electrodes. Results depend on scan-rate range and fitting quality.	[14–17]
Trasatti method	Simple and widely used for estimating outer-surface versus inner/diffusion-limited charge storage. Good as a complementary check on CV-based kinetic analysis.	Less detailed than Dunn's analysis because it is not potential resolved. Relies on extrapolation, so it is sensitive to the chosen scan-rate range.	[14,15]

4.3.4.1. b value analysis

The b-value was extracted from the power-law relationship in , $i = av^b$, where i represents peak current at a given potential, v represents the scan rate, and a, b are the fitting parameters. [13] For diffusion-controlled process, according to the Randles-Sevick equation ($i_p = 2.69 \times 10^5 n^{2/3} A D^{1/2} C v^{1/2}$), the peak current is proportional to the square root of the scan rate, thus the b-value is 0.5. On the other hand, for a pure capacitor, the relationship between current (i), capacitance (C), and scan rate (v) is $i = C\frac{dE}{dt} = Cv$, i is proportional to v, thus the b-value is 1. Generally, a b-value close to 0.5 corresponds to a diffusional-controlled process (sluggish reaction kinetics, bulk redox reaction, battery-like behavior), while a b-value close to 1 signifies a capacitance-controlled process (an ideal supercapacitor with ultrarapid reaction kinetics). At **Figure. 4.11**, three different types of energy storage devices can be categorized by their b-value. When the b-value is smaller than 0.5, it's a battery-like material; when the b-value is bigger than 0.8, it's an ideal material for a supercapacitor. When the b-value lies between 0.5 and 0.8, it's a supercapattery. [16]

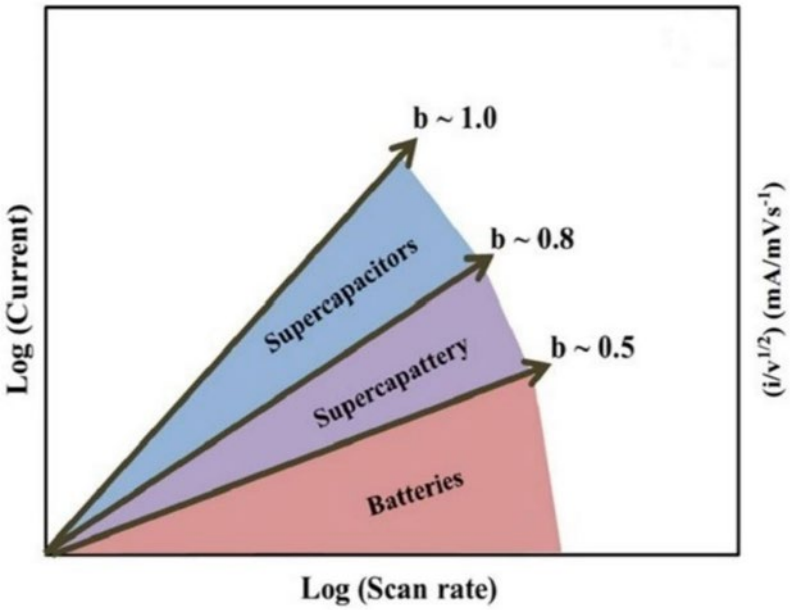


Figure 4.11. Energy storage devices are distinguished by their appropriate b-value.[16]

Comparing b-values derived from cyclic voltammetry at low and high scan rates helps elucidate mixed charge-storage mechanisms in periodic high-resolution 3D architectures. At low scan rates (e.g., 1–10 mV s^{-1}), diffusion has sufficient time to contribute, highlighting faradaic processes.

For samples with obvious redox peaks during cyclic voltammetry (**Figure 4.9.a**), i represents the peak current of the redox reaction; however, if the CV curve doesn't show obvious redox reactions (**Figure 4.9.b**), we can still estimate the b-value by selecting a current response at the same potential for different scan rates. In this case, because there is no clear peak current to track, it is better to choose several fixed potentials within the stable redox or charging region or use the current response at the midpoint/representative potential of the CV window and calculate the slope from the linear fit. Also, the b value analysis is more reliable when fitted over an appropriate, usually lower, scan rate window; at higher scan rates, deviations from ideal behavior often make the slope drift away from the true mechanism.

In **Figure 4.12**, the b-value analysis indicates that PDAN-coated 3D carbon samples exhibit primarily surface-controlled kinetics, as their b values are close to 1. For both PDAN-coated samples, the cathodic process shows a higher b value than the anodic process, suggesting that ion transport is more favorable during the anodic reaction than the cathodic reaction. This is because although PDAN is a bipolar polymer as discussed in **Section 4.2**, the anion insertion into p-type PDAN remains less effective than cation insertion into n-type PDAN, so the anodic/discharge process retains a larger diffusion-controlled contribution. The b value analysis provides a useful first assessment of charge-storage kinetics by indicating whether the current is mainly diffusion-controlled or capacitive-controlled. However, it provides only a broad mechanistic classification and cannot fully quantify the relative contributions of capacitive and diffusion processes. Therefore, Dunn's analysis is needed for a more detailed investigation because it separates the current into capacitive and diffusion-controlled components and gives a clearer comparison between different systems.

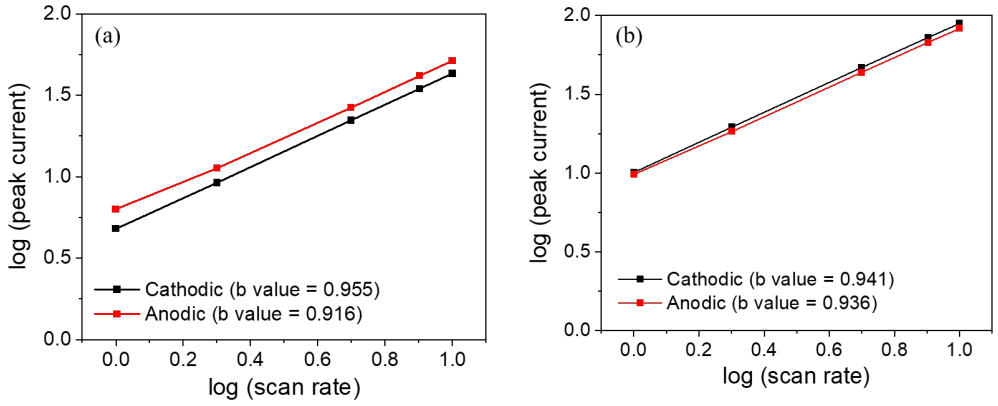


Figure 4.12 (a) b-value of PDAN-1.2 V in 3 M $NaClO_4$ at scan rate 1, 2, 5, 8, 10 mV/s, (b) b-value of PDAN-1.7 V in 3 M $NaClO_4$ at scan rate 1, 2, 5, 8, 10 mV/s.

4.3.4.2. Dunn's analysis

There are three types of charge storage mechanisms: the non-Faradaic contribution from the formation of an electric double layer, the Faradaic contribution (pseudocapacitance) from charge-transfer processes involving surface species, and the ion-insertion process. The first two charge-storage processes are fast kinetic processes that are not limited by ion diffusion. On the other hand, the ion insertion process is a relatively slow diffusion-controlled process. The cyclic voltammograms of PDAN on Na^+ were nearly box-shaped, suggesting rapid electron and ion transport in the electrode (**Figure 4.13**). In Dunn's method, the

current at a given potential can be written as

$$i(V) = k_1 v + k_2 v^{1/2}$$

where:

$i(V)$ = measured current at that potential, v = scan rate

$k_1 v$ = capacitive-controlled contribution

$k_2 v^{1/2}$ = diffusion-controlled contribution

Rearranging the equation gives:

$$\frac{i(V)}{v^{1/2}} = k_1 v^{1/2} + k_2$$

Thus, by plotting $\frac{i(V)}{v^{1/2}}$ as a function of $v^{1/2}$, the slope and intercept yield k_1 and k_2, respectively. The individual contributions can then be quantified as:

$$i(V) = k_1 v + k_2 v^{\frac{1}{2}} = i_{\text{capacitive}} + i_{\text{diffusion}}$$
$$i_{\text{capacitive}} = k_1 v$$
$$i_{\text{diffusion}} = k_2 v^{1/2}$$

Deconvolution of fast (surface-controlled) and slow (diffusion-controlled) charge-storage processes across the potential window was performed to probe the charge storage mechanism. The contribution of capacitive-controlled and diffusion-controlled reactions strongly depends on the scan rate. As shown in **Figure 4.13.f**, increasing the scan rate leads to a clear increase in the capacitive contribution and a corresponding decrease in the diffusion-controlled contribution for all electrolytes, indicating that fast surface reactions dominate at higher scan rates; the diffusion-controlled slow kinetic process doesn't have enough time to participate in the reaction.[14,15] Take a 1.2 V PDAN deposited sample, for example; in 0.5 M H_2SO_4, the capacitive contribution increases from 72% at 1 mV/s to 89% at 10 mV/s, while in 3 M $NaClO_4$, it increases from 81% to 93%. The higher diffusion capacitance of PDAN in 0.5 M H_2SO_4 compared with 3 M $NaClO_4$ likely arises from the stronger proton-coupled redox activity in the acidic electrolyte. In H_2SO_4, the small and highly mobile H^+ ions can penetrate the PDAN structure more easily and participate directly in fast protonation/deprotonation processes, which enhances the Faradaic contribution associated with diffusion-dependent charge storage. By contrast, $NaClO_4$ mainly supports more limited ion interaction with the polymer backbone, so charge storage is more dominated by surface-controlled processes. This is consistent with the Dunn analysis, where the capacitive contribution in H_2SO_4 increases from 72% at 1 mV/s to 89% at 10 mV/s (**Figure 4.13.f)**, while in $NaClO_4$ it increases from 81% to 93% (**Figure 4.14.f)**, indicating that both electrolytes show enhanced surface control at higher scan rates but the acidic medium provides a larger diffusion-related response overall.

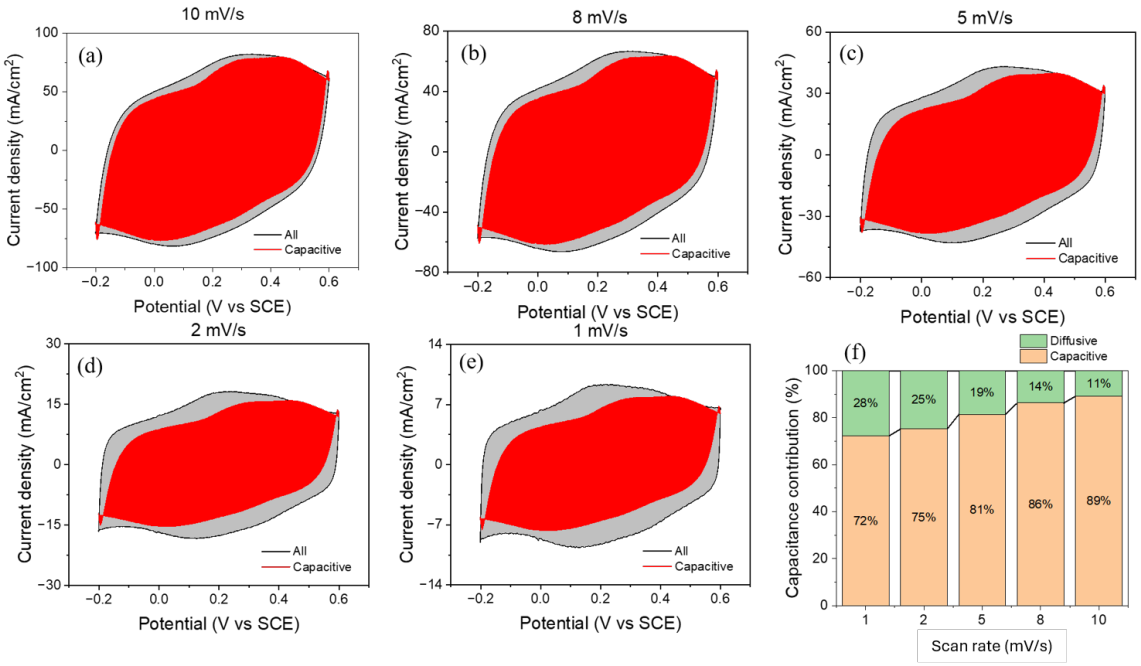


Figure 4.13 (a-e) Cyclic voltammetry curves at 10, 8, 5, 2, and 1 mV/s of 1.2 V-PDAN deposition 3D carbon in 0.5 M H_2SO_4, (f) Capacitive and diffusive contribution ratios based on Dunn's analysis at different scan rates.

Figure 4.14 and **Figure 4.15** present Dunn's analysis results of the 1.2 V PDAN-deposited sample and the 1.7 V PDAN-deposited sample in 3 M $NaClO_4$. Dunn's analysis indicates that both PDAN films are dominated by surface-controlled pseudocapacitive charge storage, but the thicker film deposited at 1.7 V shows a larger diffusion contribution than the thinner film deposited at 1.2 V. For the 1.2 V PDAN sample, the capacitive fraction remains higher across all scan rates, with only a slight increase in diffusive contribution as the scan rate decreases (7% at 10 mV/s, 19% at 1 mV/s); in contrast, the 1.7 V PDAN sample shows a more noticeable increase in diffusion-controlled charge storage, especially at lower scan rates (11% at 10 mV/s, 29% at 1 mV/s). This trend indicates that increasing PDAN thickness makes ion transport more tortuous and slows electrolyte penetration, so a larger portion of the current is limited by the diffusion process rather than by fast surface capacitive processes. At the same time, the high capacitive fractions in both samples confirm that PDAN still behaves mainly as a pseudocapacitive polymer, with rapid faradaic reactions contributing the majority of the stored charge. Overall, the thicker 1.7 V film preserves strong pseudocapacitance but at the cost of greater diffusion resistance than the thinner 1.2 V film.

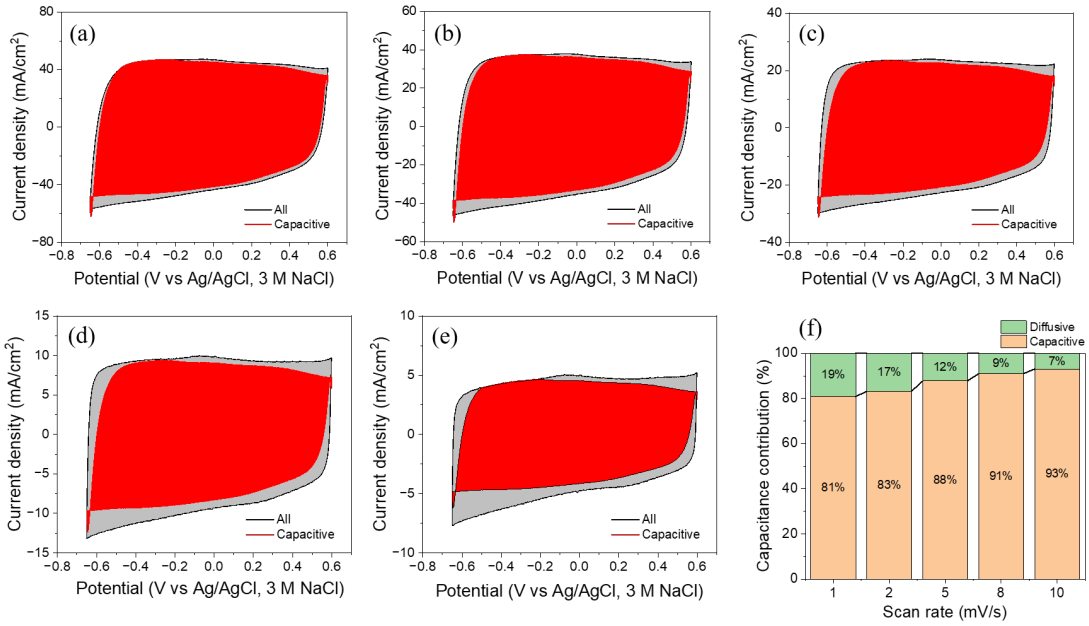


Figure 4.14. (a-e) Cyclic voltammetry and Dunn analysis curves at 10, 8, 5, 2, and 1 mV/s of 1.2 V-PDAN deposition 3D carbon in 3 M $NaClO_4$, (f) Capacitive and diffusive contribution ratios based on Dunn's analysis at different scan rates.

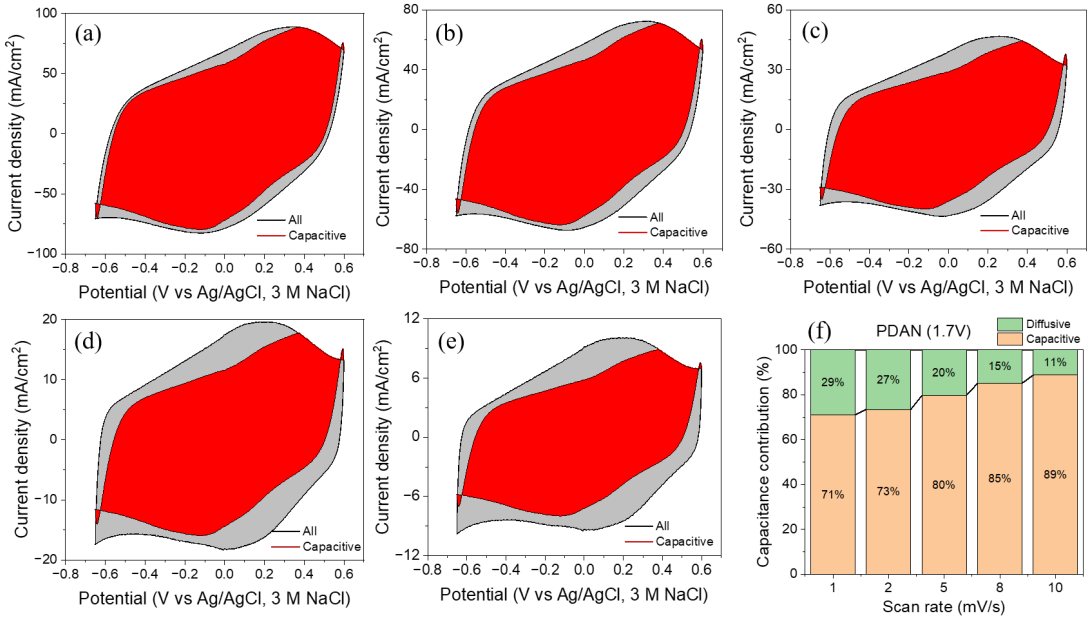


Figure 4.15. (a-e) Cyclic voltammetry and Dunn analysis curves at 10, 8, 5, 2, and 1 mV/s of 1.7 V-PDAN deposition 3D carbon in 3 M $NaClO_4$, (f) Capacitive and diffusive contribution ratios based on Dunn's analysis at different scan rates.

4.3.4.3. Electrochemical impedance spectroscopy (EIS) analysis on 3D PDAN deposited carbon electrode

Electrochemical impedance spectroscopy (EIS) is a powerful method for investigating electrochemical performance because it separates resistive, capacitive, and diffusion-related processes over a wide frequency range.[16] Here, we use Nyquist plots and the Warburg coefficient derived from EIS data to further investigate the capacitive and diffusive kinetics of electrolytes with 3D PDAN electrodes. In a Nyquist plot, the high-frequency intercept gives the solution resistance or internal resistance; the semicircle is commonly associated with charge-transfer resistance and interfacial capacitance; and the low-frequency line reflects ion-diffusion behavior, making this plot very useful for a quick qualitative picture of electrode kinetics. However, Nyquist plots are not always easy to interpret because several processes can overlap, the same shape can arise from different equivalent circuits, and the frequency associated with each point is not shown directly. In contrast, the Warburg coefficient provides a more focused insight into diffusion resistance by quantifying the low-frequency diffusion response, which helps estimate ion-transport kinetics and compare diffusion limitations in different electrodes or electrolytes.

4.3.4.3.1. Nyquist Plot

Figure 4.16 presents the trend of solution resistance (Rs, also known as ohmic resistance or uncompensated resistance): PDAN (1.2V) < PDAN (1.7V-stabilized) < 3D carbon before PDAN deposition < PDAN (1.7V). This indicates that the 1.2 V film likely provided the best overall electronic/ionic contact path. At the same time, the untreated 3D carbon had a slightly poorer effective ohmic pathway than the stabilized film, and the as-deposited 1.7 V film had the highest resistance. A higher deposition potential can make the PDAN film more oxidized, thicker, or more compact in structure, thereby increasing the ion diffusion path and reducing wettability, leading to higher Rs.

In contrast, the charge transfer resistance (Rct) reflects how readily charge crosses the electrode/electrolyte interface, making it sensitive to the number of accessible redox sites. In this experiment, Rct: PDAN (1.7V-stabilized) > PDAN (1.2V) ~ PDAN (1.7V) > 3D carbon before PDAN deposition, meaning the stabilized 1.7 V film became more stable but less kinetically open at the interface, which is consistent with removal of loosely bound species and film reorganization into a denser layer. After stabilization, unstable low-molecular-weight species may be removed, but the remaining film can become more compact and less accessible, so Rct rises even if diffusion improves. Therefore, the stabilized 1.7 V sample can show a lower diffusion impedance but a higher kinetic barrier for interfacial charge transfer.

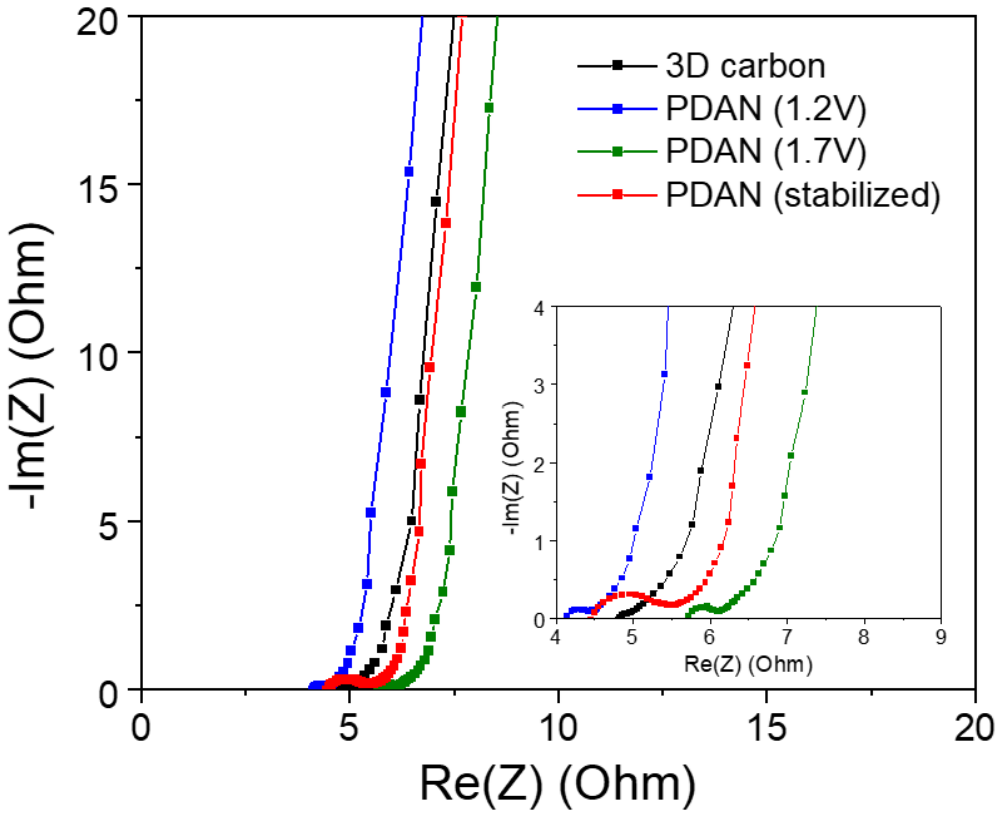


Figure 4.16 EIS data of 3D carbon and 3D carbon with different PDAN deposition potential samples in 3 M $NaClO_4$

4.3.4.3.2. Warburg coefficient (diffusion resistance)

In the three-electrode system, the total current can be divided into the current associated with EDLC charge/discharge (IC) and the current associated with the Faradic reaction (I_F). According to **Figure 4.17.a**, the general impedance of Faradic reaction (Z_F) accounts for both the kinetics of redox reaction and the diffusion of redox species from electrolyte to electrode surface; therefore, the impedance of Z_F can be written as: $Z_F = R_{ct} + Z_W$. [18]

1. R_{ct} is the charge-transfer resistance, which is related to the kinetics of redox species not absorbed on the electrode surface, and it can be written as

$$R_{ct} = \frac{RT}{k^0 n^2 F^2 AC}$$

where k^0 is the heterogeneous electron transfer rate (cm/s), n is the number of electrons participated in the redox reaction, F is the faraday's constant (96485 C/mol), R is the gas constant (8.314 J/mol K), T is the temperature (K), A is the electrochemical active surface area (cm^2) and C is the concentration of redox species.

2. Z_w is called the Warburg impedance, which indicates the mass transport of redox species from electrolyte to electrode surface. And Z_w can be written as

$$Z_w = R_w + C_w = [\sigma\omega^{-\frac{1}{2}} - j\left(\sigma\omega^{-\frac{1}{2}}\right)],\ \sigma = \frac{2RT}{n^2F^2\sqrt{2}\sqrt{D}C}$$

where D is the diffusion coefficient (cm^2/s) of the redox species; the rest of the symbols have the same meaning as in previous content.

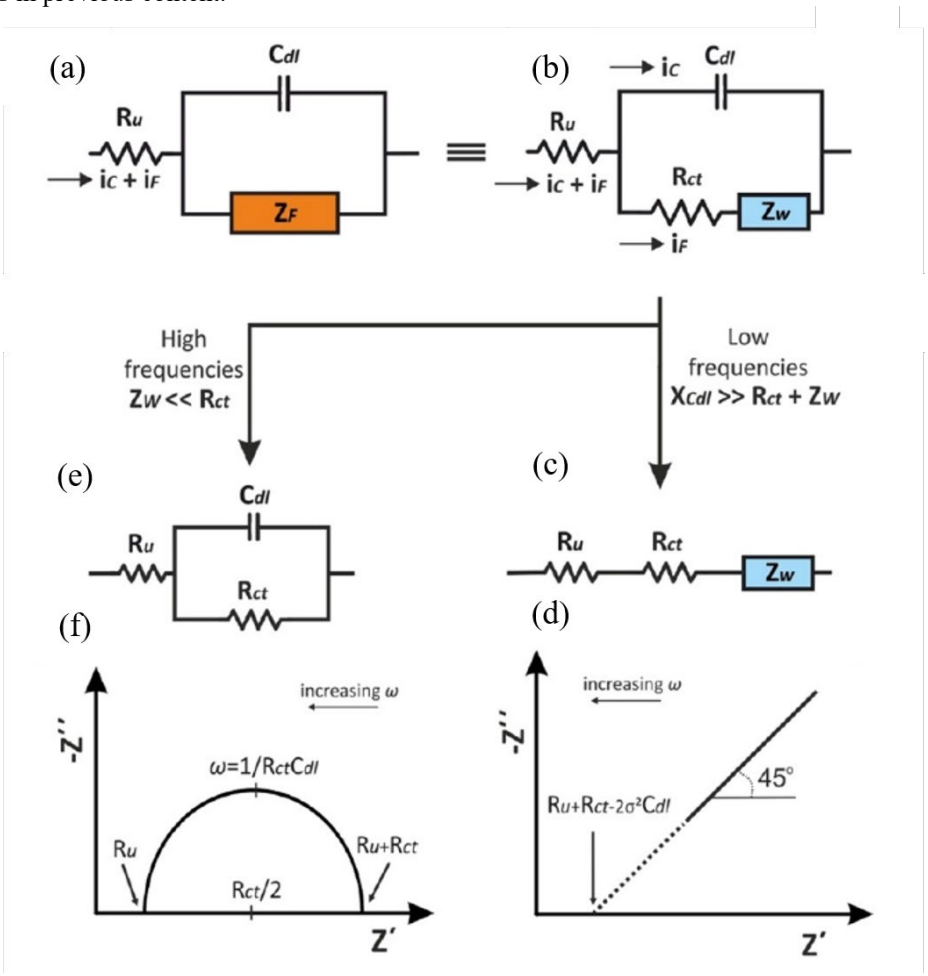


Figure 4.17. (a, b) The Randles equivalent circuit and its behavior at (c, d) low and (e,f) high frequencies. [18]

The equivalent electrical circuit is called the Randles circuit (Figure 4.3.3.1B), and the electrical impedance of the Randles circuit can be separated into the real part (Z') and the imaginary part (Z''), given as the following equations:

$$Z' = R_u + \frac{R_{ct} + \sigma\omega^{-1/2}}{(\sigma\omega^{1/2}C_{dl} + 1)^2 + \omega^2 C_{dl}^2 (R_{ct} + \sigma\omega^{-1/2})^2}$$

$$-Z'' = \frac{\omega C_{dl}(R_{ct} + \sigma\omega^{-1/2})^2 + \sigma^2 C_{dl} + \sigma\omega^{-1/2}}{(\sigma\omega^{1/2}C_{dl} + 1)^2 + \omega^2 C_{dl}^2 (R_{ct} + \sigma\omega^{-1/2})^2}$$

Where R_u is called the uncompensated resistance, which is the ohmic resistance of the electrolyte between the reference and the working electrode, C_{dl} is the capacitance of the electrical double layer at the electrode/electrolyte interface under ac conditions, and R_{ct} is the charge-transfer resistance.

At low frequencies, the C_{dl} value is very high; thus, the current will pass through the R_u, R_{ct}, and Z_w (**Figure**

4.17). When the limiting condition is $\omega \to 0$, the Z_w equations can be rewritten as:

$$Z' = R_u + R_{ct} + \sigma\omega^{-1/2}$$

$$Z'' = -\sigma\omega^{-\frac{1}{2}} - 2\sigma^2 C_{dl}$$

Therefore, we can calculate the σ (Warburg's coefficient) from plotting the EIS data by using $\omega^{-\frac{1}{2}}$ as the x-axis and the real part of impedance ($Z^{'}$) as the y-axis; the slope of this line will be the Warburg's coefficient.

For Warburg coefficient calculation, $\omega^{-0.5}$ = 0.5 to 3.0 region was selected because it corresponds to the most distinct diffusion-controlled response in the impedance data. Within this range, the impedance exhibits an approximately linear dependence characteristic of diffusion, indicating that mass transport is the dominant contribution to the electrochemical response. Moreover, this region avoids deviations typically observed at very low frequencies, which are often caused by finite-diffusion-length effects, instrumental noise, and non-ideal interfacial processes that undermine the reliability of the ideal Warburg response.

The bare 3D carbon exhibits the highest Warburg coefficient because ion transport is relatively hindered inside the porous carbon network. In this state, ions must move through tortuous pores and access internal surface sites directly on the carbon. After coating with the conducting polymer PDAN, the ion/electron transport pathway becomes more continuous and electrochemically active, so ions no longer rely as much on slow diffusion through the bare carbon architecture. A redox-active PDAN film also provides additional pseudocapacitive charge storage and easier ion-insertion pathways, which reduces the apparent Warburg contribution in EIS. As the deposition potential and cycle number increase, Rct also increases, indicating a slower interfacial charge-transfer process due to increased PDAN thickness, as shown in **Figure 4.18**. This is also supported by the increased Warburg coefficient between the PDAN (1.2V) and PDAN (1.7V) samples, indicating that it becomes harder for ions to penetrate deeply into the thicker PDAN layer.

Although stabilization increases charge-transfer resistance, it also decreases the Warburg coefficient, suggesting that repeated cycling removed loosely bound species and reorganized the film into a more stable but less interfacial-accessible redox structure. After rinsing the 1.7V-PDAN sample with acetonitrile and repeated cyclic voltammetry scans, the loosely bound oligomers and weakly attached low-molecular-weight species can be removed, leaving a more compact, better-adhered electroactive PDAN deposition layer on the 3D carbon scaffold. This stabilization process can improve film uniformity and reduce tortuosity during ion exchange, thereby reducing the fitted Warburg coefficient and increasing the diffusion coefficient.

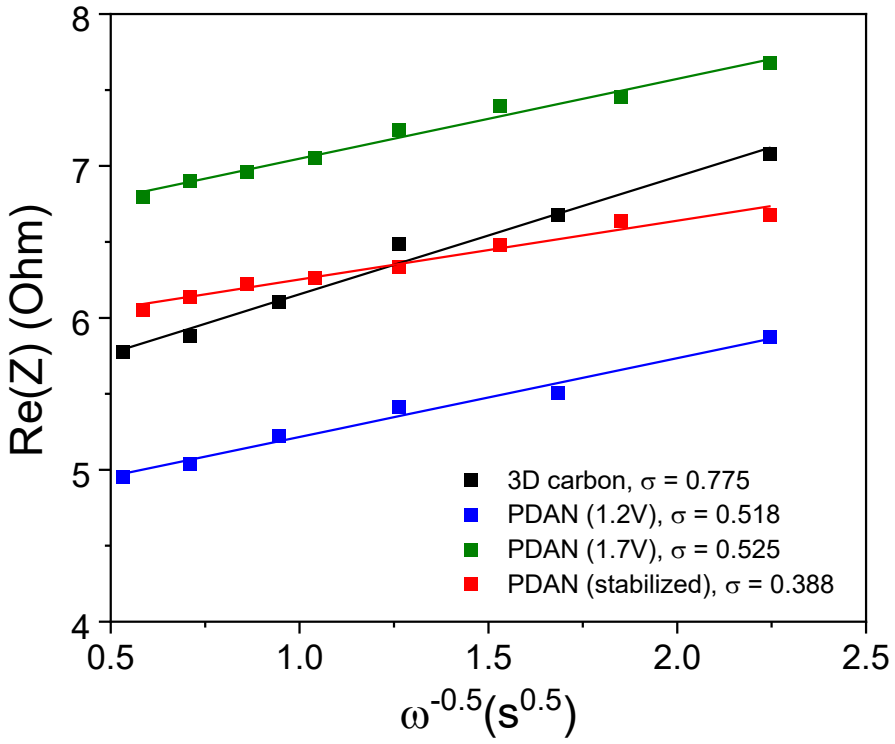


Figure 4.18 Warburg coefficient data of 3D carbon and 3D carbon with different PDAN deposition potential samples in 3 M $NaClO_4$ (two samples are tested under different PDAN deposition, both of them show the same trend)

4.3.5. Cycle stability of PDAN-coated 3D carbon sample

Redox-active conjugated polymers are promising energy storage materials due to their high theoretical capacitance, good electrical conductivity, and additional pseudocapacitive charge storage. However, conductive polymers often suffer from limited material utilization and poor cycling stability [12,13,19]; take PANI, for example: the electrical conductivity decreases significantly in both the oxidized and reduced states, especially at high oxidation levels, thereby restricting electron transport and ultimately limiting the achievable mass loading. Their poor cycle life is mainly attributed to repeated swelling and de-swelling during ion insertion and removal, as well as the reduced stability of the highly oxidized polymer form.

A long-term cycle stability test was done by running 3D-printed carbon electrodes conformally coated with PDAN in 3 M NaCl, using a graphite rod as the counter electrode and SCE as the reference electrode at 100 mV/s for 100000 cycles, and running a 5 mV/s CV scan at every 500 runs to record the CV curve change with more details (**Figure 4.19.a**). The PDAN-coated sample demonstrates exceptional electrochemical stability. The coated electrodes retain over 94.6% of their initial capacitance after 100,000 cycles at a scan rate of 100 mV/s, reflecting minimal loss of active material or interface connectivity during repeated operation (**Figure 4.19.b**). **Figure 4.19.c** shows an outstanding capacity retention (94.6% after 100000 cycles at 100 mV/s), which is primarily due to the conformal coating of the polymer on the 3D carbon sample, which forms a continuous, uniform layer over the complex carbon strut topology and prevents polymer delamination

or agglomeration during repeated charge–discharge cycles. The good interfacial contact between PDAN and the 3D carbon surface maintains efficient electronic pathways between the conductive carbon scaffold and the redox-active polymer, while also preserving ion-accessible surface area.

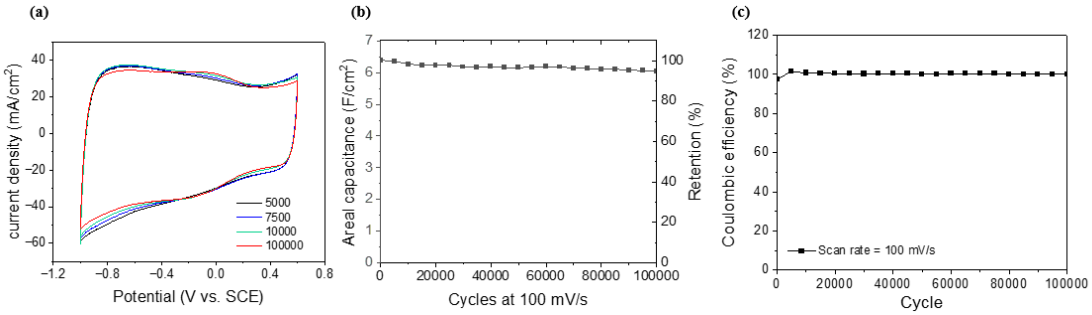


Figure 4.19 (a) 5 mV/s CV curves in 3 M NaCl after 5000,7500,10000 and 100000 cycles, (b) Areal capacitance and capacitance retention of S1-PDAN after 100000 cycles at 100 mV/s, (c) Coulombic efficiency of S1-PDAN after 100000 cycles at 100 mV/s.

To better evaluate the cycling and electrochemical stability of the PDAN sample, an additional PDAN-coated 3D carbon electrode was prepared and initiated a cycle stability test at a lower GCD current density of 30 mA/cm^2. Compared with a faster test condition (100 mV/s), this slower rate allows more complete utilization of the redox-active sites and ion transport, making the result more representative of the material's intrinsic long-term stability rather than only its high-rate performance. It also helps reveal gradual degradation processes, such as active-site loss and polymer degradation, that may be overlooked under faster testing conditions, where polarization and incomplete utilization can dominate the response. **Figure 4.20.c** shows the areal capacitance retention as a function of cycle number at 30 mA/cm^2. The decreasing capacitance is also evident from the progressively shorter charge and discharge times in the GCD curves at different cycle numbers (**Figure 4.20.b**). The electrode demonstrates promising long-term stability, retaining more than 91% of its initial capacitance after 7500 cycles. Coulombic efficiency (CE) remained essentially 100% (**Figure 4.20.d**). CV curves at 10 mV/s (**Figure 4.20.a**) confirm that a significant pseudocapacitive contribution from PDAN persists despite extended cycling. This cycle stability experiment is still ongoing.

The cycling stability of conductive polymers is often limited by structural degradation caused by repeated volumetric change during ion insertion and extraction, i.e., doping and de-doping processes. However, the 3D PDAN-coated carbon electrode offers high electrochemical stability, and it can be ascribed to the following factors: (1) The highly conjugated PDAN can strongly anchor to the carbon substrate through π–π interactions and promote intermolecular π–π stacking, thereby improving structural integrity by providing additional support.(2) The rigid polycyclic aromatic framework, whether in a ladder-like or highly branched linear architecture, exhibits lower solubility in aqueous electrolytes than conventional conductive polymers, which helps suppress swelling, chain rearrangement, and dissolution and preserves electrical contact during long-term cycling. (3) The relatively weak interaction between Na^+ ions and the PDAN redox centers facilitates reversible ion insertion and extraction with minimal structural perturbation, further reducing capacity fading over extended cycling. (4) The highly interconnected 3D architected structure allows faster ion diffusion and reduces the transport distance of electrolyte ions inside the 3D electrodes during the charge/discharge processes compared to conventional 2D planar electrodes. The high coulombic efficiency, together with the largely unchanged CV and GCD responses, highlights the promise of PDAN for sodium-ion-based energy storage, where reversibility and durability are essential for practical applications.

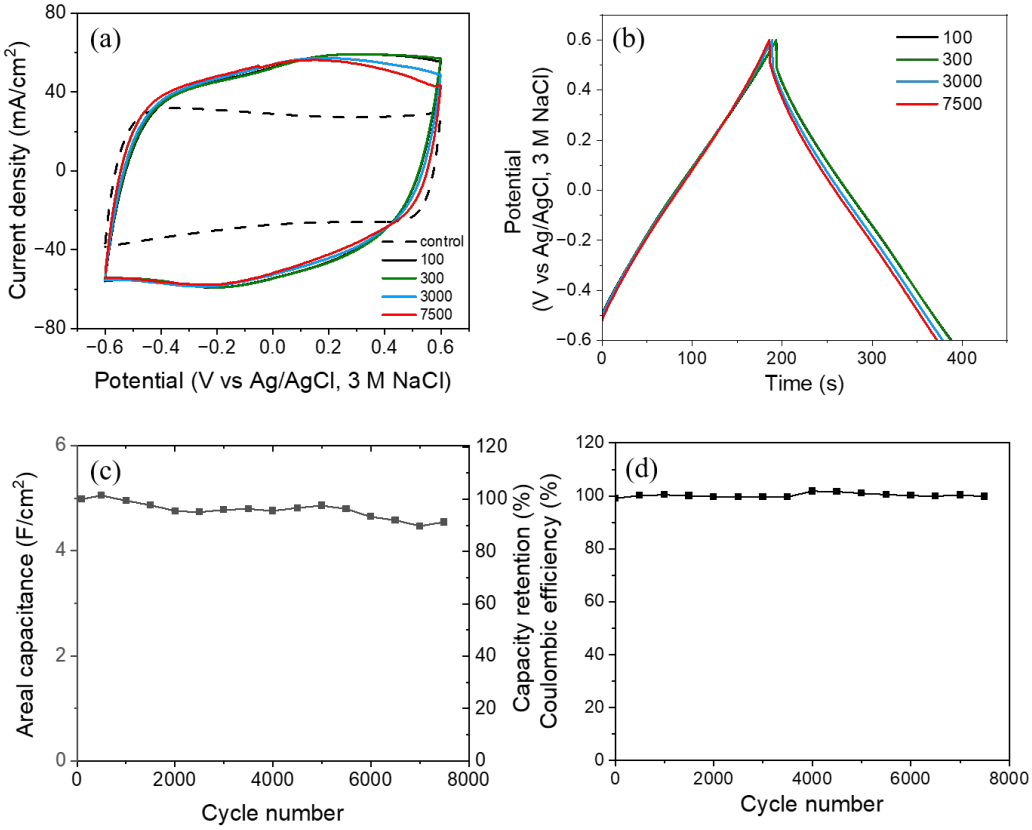


Figure 4.20 (a) 10 mV/s CV curves in 3 M $NaClO_4$ after 100, 300,3000 and 7500 cycles, (b) GCD curves of PDAN sample at 30 mA/cm^2 after 100, 300, 3000 and 7500 cycles (c) Areal capacitance and capacitance retention of PDAN coated sample after 7500 cycles at 30 mA/cm^2, (d) Coulombic efficiency of PDAN coated sample after 7500 cycles at 30 mA/cm^2.

4.4. Conclusion and future plan

In summary, a conducting polymer PDAN with an electronic conductivity of around 5.9×10-5 S/cm is electrochemically deposited on a high-resolution hierarchical 3D carbon electrode to improve capacitance through enhanced wettability and additional pseudocapacitance, and to improve mechanical integrity by providing support from the polymer outer layer. Owing to the semiconducting behavior of PDAN, the PDAN-coated 3D carbon electrode exhibits high-capacity retention (94% over 100000 cycles). Also, the areal capacitance of the 2 mm-thick high-resolution 3D carbon electrode increased from 5.07 F/cm^2 to 8.89 F/cm^2 upon PDAN deposition at 5 mA/cm^2.

Overall, this dissertation demonstrates a facile post-processing catalyst infiltration strategy that enhances the carbon conversion ratio while preserving the intricate structures of 3D-printed polymer electrodes. Moreover, the as-prepared 3D carbon electrode can serve as an ideal scaffold for integrating active materials, such as conducting polymers, to improve electrochemical performance further. This approach provides a promising material for developing scalable, sustainable, and high-performance electrodes in energy storage applications.

In future work, our lab plans to investigate the bipolar functionality of PDAN in energy storage applications with different metal salt electrolytes. By systematically comparing the electrochemical behavior of PDAN

interacting with various metal species, we aim to understand how metal–polymer interactions influence charge storage, ion transport, and redox activity during both charge and discharge. This study will help clarify whether specific metal salts can enhance the bipolar response of PDAN and improve its performance as an electrode material for advanced energy storage systems.

References

[1] Q. Meng, K. Cai, Y. Chen, L. Chen, Research progress on conducting polymer-based supercapacitor electrode materials, Nano Energy 36 (2017) 268–285. https://doi.org/10.1016/j.nanoen.2017.04.040.

[2] A. Eftekhari, L. Li, Y. Yang, Polyaniline supercapacitors, Journal of Power Sources 347 (2017) 86-107. https://doi.org/10.1016/j.jpowsour.2017.02.054.

[3] J.F. Mike, J.L. Lutkenhaus, Recent advances in conjugated polymer energy storage, Journal of Polymer Science Part B: Polymer Physics 51 (2013) 468–480. https://doi.org/10.1002/polb.23256.

[4] M. Acerce, S. Chiovoloni, Y. Hernandez, C. Ortuno, J. Qian, J. Lu, Poly(1,5-diaminonaphthalene)-Grafted Monolithic 3D Hierarchical Carbon as Highly Capacitive and Stable Supercapacitor Electrodes, ACS Appl. Mater. Interfaces 13 (2021) 53736–53745. https://doi.org/10.1021/acsami.1c13746.

[5] Z. Qiao, K. Horatz, P.Y. Ho, A. Mitrofanov, C. Zhou, N. Sun, F.S.-C. Lissel, Carboxylic Groups via Postpolymerization Modification of Polythiophene and their Influence on the Performance of a Polymeric MALDI Matrix, Macromolecular Chemistry and Physics 224 (2023) 2200250. https://doi.org/10.1002/macp.202200250.

[6] K. Bruchlos, D. Trefz, A. Hamidi-Sakr, M. Brinkmann, J. Heinze, A. Ruff, S. Ludwigs, Poly(3-hexylthiophene) revisited – Influence of film deposition on the electrochemical behavior and energy levels, Electrochimica Acta 269 (2018) 299–311. https://doi.org/10.1016/j.electacta.2018.02.126.

[7] A.M. Fathi, H.S. Mandour, Electrosynthesized conducting poly(1,5-diaminonaphthalene) as a corrosion inhibitor for copper, Polym. Bull. 77 (2020) 3305–3324. https://doi.org/10.1007/s00289- 019-02913-w.

[8] L. Yan, Q. Zhu, Y. Qi, J. Xu, Y. Peng, J. Shu, J. Ma, Y. Wang, Towards High-Performance Aqueous Zinc Batteries via a Semi-Conductive Bipolar-Type Polymer Cathode, Angew Chem Int Ed 61 (2022) e202211107. https://doi.org/10.1002/anie.202211107.

[9] Y. Wang, C. Zheng, M. Zhao, X. Wang, Y. Su, G. Diao, C. Wang, In Situ Electrochemical Polymerized Bipolar-Type Poly(1,5-diaminonaphthalene) Cathode for High-Performance Aqueous Zinc-Organic Batteries, ACS Appl. Polym. Mater. 6 (2024) 14928–14938. https://doi.org/10.1021/acsapm.4c03352.

[10] Y. Xu, X.-Z. Tang, X. Xie, N. Wang, S. Komarneni, Development of Poly(naphthalene-diamine) as a Low-Cost, High-Performance Organic Cathode Material for Aqueous Zinc-Organic Batteries, ACS Appl. Polym. Mater. 7 (2025) 14621–14629. https://doi.org/10.1021/acsapm.5c02768.

[11] S. Chen, Z. Liu, S. Jiang, H. Hou, Carbonization: A feasible route for reutilization of plastic wastes, Science of the Total Environment 710 (2020) 136250. https://doi.org/10.1016/j.scitotenv.2019.136250.

[12] R. Dallaev, Conductive Polymer Thin Films for Energy Storage and Conversion: Supercapacitors, Batteries, and Solar Cells, Polymers (Basel) 17 (2025) 2346. https://doi.org/10.3390/polym17172346.

[13] S. Suriyakumar, P. Bhardwaj, A.N. Grace, A.M. Stephan, Role of Polymers in Enhancing the Performance of Electrochemical Supercapacitors: A Review, Batteries & Supercaps 4 (2021) 571–

584. https://doi.org/10.1002/batt.202000272.

[14] A. Cymann-Sachajdak, M. Graczyk-Zajac, G. Trykowski, M. Wilamowska-Zawłocka, Understanding the capacitance of thin composite films based on conducting polymer and carbon nanostructures in aqueous electrolytes, Electrochimica Acta 383 (2021) 138356. https://doi.org/10.1016/j.electacta.2021.138356.

[15] S. Harish, P.U. Sathyakam, Dunn's Method for Distinguishing Charge Storage Mechanisms in Supercapacitors: A Status Quo Review, J. Electron. Mater. 54 (2025) 10858–10872. https://doi.org/10.1007/s11664-025-12481-7.

[16] R. Hasan, Y. Altaf, N. Jabeen, N. Ul Hassan, F. Ahmed, S. Hussain, A. Hussain, S. Ullah Asif, B.A. Al-Asbahi, ZnS@Fe2O3 core–shell nanorod arrays for supercapattery applications; theoretical evaluation of faradic and non-faradic behavior using Dunn's model, Journal of Electroanalytical Chemistry 966 (2024) 118411. https://doi.org/10.1016/j.jelechem.2024.118411.

[17] A.M. Afzal, N. Muzaffar, M.W. Iqbal, G. Dastgeer, A. Manzoor, M. Razaq, S.M. Wabaidur, E.A. Al-Ammar, S.M. Eldin, Exploring the charge storage mechanism in high-performance Co@MnO2- based hybrid supercapacitors using Randles–Ševčík and Dunn's models, J Appl Electrochem 54 (2024) 65–76. https://doi.org/10.1007/s10800-023-01939-3.

[18] A.Ch. Lazanas, M.I. Prodromidis, Electrochemical Impedance Spectroscopy—A Tutorial, ACS Meas. Sci. Au 3 (2023) 162–193. https://doi.org/10.1021/acsmeasuresciau.2c00070.

[19] A. Patel, S.K. Patel, R.S. Singh, R.P. Patel, Review on recent advancements in the role of electrolytes and electrode materials on supercapacitor performances, Discov Nano 19 (2024) 188. https://doi.org/10.1186/s11671-024-04053-1.